工學博士 學位論文

Optimal Numerical/Experimental Assessment on GFRP for Wind Turbine Blades in Repairing Process utilizing Photo Polymerizable Resin

Photo polymerizable resin을 사용한 풍력 터빈 블레이드용 GFRP repair 공정 시 최적의 수치적 및 실험적 평가

指導敎授 金 允 海

2019년 6월

韓國海洋大學校 大學院

造船機資材工學科

陳 梓 萱

본 논문을 CHEN ZIXUAN의 공학박사 학위논문으로 인준함

위원장 배 창 원 (인)

위 원 김 윤 해 (인)

위 원 김 준 영 (인)

위 원 신 도 훈 (인)

위 원 윤 성 원

2019년 6월 28일

한국해양대학교 대학원

Contents

1. Introduction

2. Literature Review

3. Experimental and Numerical Analysis of UV repaired GFRP

4. Effect of Low Temperature Environment on UV repaired GFRP

5. Durability of UV repaired GFRP among Acidic Atmosphere

6. Performance of UV repaired GFRP during UV ageing Process

7. Summary and Conclusions

List of Tables

List of Figures

Optimal Numerical/Experimental Assessment on GFRP for Wind Turbine Blades in Repairing Process utilizing Photo Polymerizable Resin

Chen, Zixuan

Division of Materials Engineering
Department of Marine Equipment Engineering
Graduate School of Korea Maritime and Ocean University

Abstract

Fiber reinforced plastics are drawing significant attention to the renewable energy sectors in terms of their excellent specific strength, modulus and stiffness properties as well as outstanding processability, corrosion, and chemical resistance. Wind turbine blades, which inherent GFRP main bodies, are the representative practice for generating renewable energy. While the wind turbine blades may inevitably be damaged due to the harsh service environments like low temperature, acidic moisture, and intense UV irradiation. Remediations on a damaged wind turbine are indispensable to preserve the integrity, guarantee the strength, and expanse the service life. The photo polymerizable resins are featured by less energy consumption, equipment requirement and curing time compared to conventional thermal polymerizable resins. During this dissertation, the photo polymerizable resins were employed to conduct patch remediation on pre-damaged GFRP specimens. The stress and damage distributions of repaired GFRP specimens were obtained through numerical/experimental assessments to validate the remediation feasibility; properties in low temperature were investigated, which was in consideration of the relative cold service environment; durability of repaired GFRP specimens in long-term UV and acid ageing were evaluated to represent the typical service environments of wind turbine blades.

KEY WORDS: GFRP; patch remediation; photo polymerizable resin; low temperature; durability

1. Introduction

1.1 Research background

In our daily lives, we are surrounded by a variety of products, utensils, and equipments. In order to manufacture these things, materials are necessary. These materials must have some characteristics like insulating or conduct heat and electricity, reject or accept magnetic flux, withstand loads, transmit or reflect light, be stable in hostile environments, and perform all these functions without damaging the environment or costing too much (Loos, 2015).

Around 1890s, only a few hundred materials were available in the market. However, engineers and designers currently have more than 60,000 different types of materials available (Ashby, et al., 2007). It is difficult to study all these materials and their properties individually, so a general classification is needed to enable simplification and characterization (Sanjay, 2002).

Engineering materials, depending on their main characteristics such as strength, stiffness, density, and melt temperature, can be conveniently divided into four main categories: (1) metal, (2) polymers, (3) ceramic, and (4) composites (William, 2007). Some authors still divide the materials into additional groups such as semiconductors and biomaterials. In this dissertation, we will adopt the division based on four main categories. Fig. 1 shows the properties of some materials selected from each class.

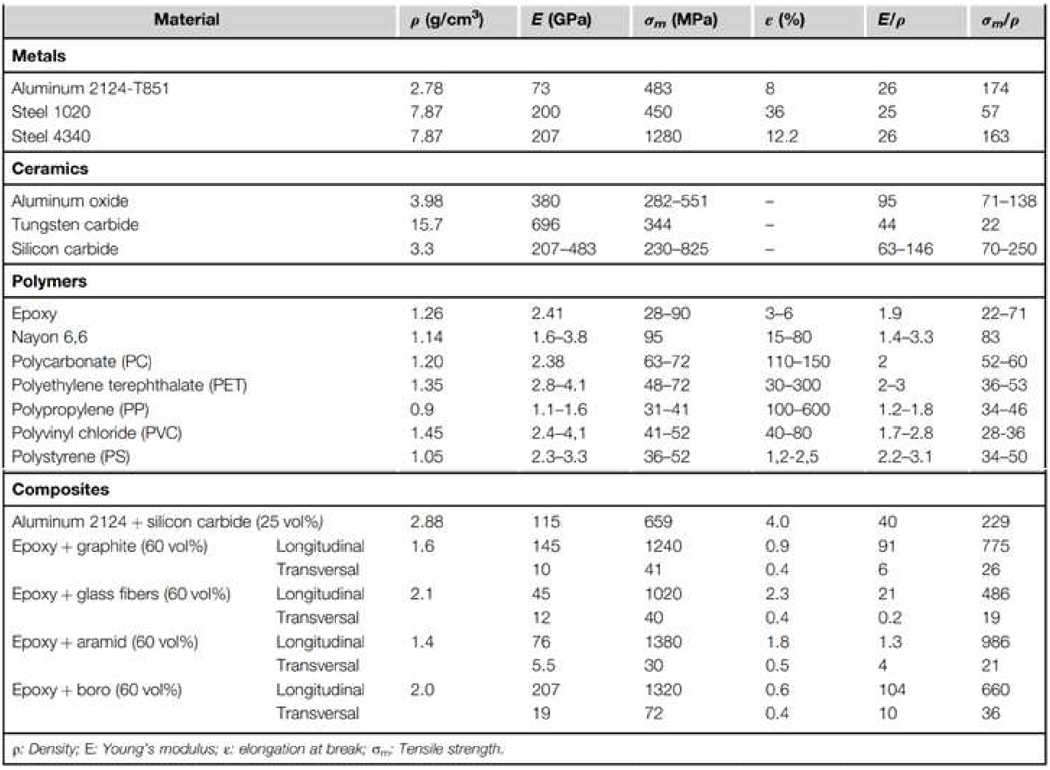

Material		ρ (g/cm^3)	E (GPa)	σ_m (MPa)	ε (%)	E/ρ	σ_m/ρ
Metals							
Aluminum 2124-T851		2.78	73	483	8	26	174
Steel 1020		7.87	200	450	36	25	57
Steel 4340		7.87	207	1280	12.2	26	163
Ceramics							
Aluminum oxide		3.98	380	282–551	–	95	71–138
Tungsten carbide		15.7	696	344	–	44	22
Silicon carbide		3.3	207–483	230–825	–	63–146	70–250
Polymers							
Epoxy		1.26	2.41	28–90	3–6	1.9	22–71
Nayon 6,6		1.14	1.6–3.8	95	15–80	1.4–3.3	83
Polycarbonate (PC)		1.20	2.38	63–72	110–150	2	52–60
Polyethylene terephthalate (PET)		1.35	2.8–4.1	48–72	30–300	2–3	36–53
Polypropylene (PP)		0.9	1.1–1.6	31–41	100–600	1.2–1.8	34–46
Polyvinyl chloride (PVC)		1.45	2.4–4,1	41–52	40–80	1.7–2.8	28-36
Polystyrene (PS)		1.05	2.3–3.3	36–52	1,2-2,5	2.2–3.1	34–50
Composites							
Aluminum 2124 + silicon carbide (25 vol%)		2.88	115	659	4.0	40	229
Epoxy + graphite (60 vol%)	Longitudinal	1.6	145	1240	0.9	91	775
	Transversal		10	41	0.4	6	26
Epoxy + glass fibers (60 vol%)	Longitudinal	2.1	45	1020	2.3	21	486
	Transversal		12	40	0.4	0.2	19
Epoxy + aramid (60 vol%)	Longitudinal	1.4	76	1380	1.8	1.3	986
	Transversal		5.5	30	0.5	4	21
Epoxy + boro (60 vol%)	Longitudinal	2.0	207	1320	0.6	104	660
	Transversal		19	72	0.4	10	36

ρ: Density; E: Young's modulus; ε: elongation at break; σ_m: Tensile strength.

Fig. 1 Typical Properties of Engineering Materials (Loos, 2015)

Composite materials have become common engineering materials and are designed and manufactured for various applications including aerospace parts, automotive components, sporting goods, consumer goods, and in the marine and oil industries since the 1960s. Among all materials, composite materials have the potential to replace widely used steel and aluminum, and usually with better performance. Composite materials are 60-80% lighter than steel components and 20-50% lighter by replacing aluminum parts. It appears that composites have become a better choice for many engineering applications nowadays.

The composite material is composed of two or more than two components of different properties and has new properties on the macroscopic or macro level. All kinds of materials have the synergistic effect and making the properties of composite materials better than the original components to fulfill different demands. The matrix of composite have both metals and non-metals. Typical engineered composite materials include mortars, concrete, reinforced plastics, ceramic composites and so on. Composite materials are generally used for buildings, bridges, and structures such as boat hulls, swimming pool panels, race car bodies, the most advanced examples perform routinely on spacecraft and aircraft in demanding environments (Isaac, et al., 2006).

Glass fibers have been manufactured from glass since the 1930s. GFRP is a form of fiber reinforced plastic where glass fiber is the reinforcement. This is the reason perhaps why GFRP is also known as glass reinforced plastic or glass fiber reinforced plastic. The glass fiber is usually flattened into a sheet, randomly arranged or woven into a fabric. According to the use of the GFRP, the glass fibers can be made of different types of glass.

GFRP is lightweight, durable and less brittle. The best part of GFRP is its ability to get molded into various complicated shapes. This pretty much explains why GFRP is widely used in bathtubs, boats, aircraft, roofing, and other applications.

Polymer composite materials, which can be used to manufacture lighter and larger turbine blades, offer several opportunities in the wind energy industry (Katnam, et al., 2015). From a structural design viewpoint, composite materials have many advantages such as high strength-to-weight ratio, high stiffness-to-weight ratio, fatigue tolerance, corrosion resistance, formability (i.e., easily mouldable to complex shapes), tailored mechanical properties, and low thermal expansion. Wind turbine blades are typically manufactured using E-glass fibers (with 10-15 mm diameter, 2.5-2.6 g/cm^3 density, 70–75 GPa Young’s modulus and –3,500 MPa tensile strength) or combined E-glass and carbon fibers (with 6-8 mm diameter, 1.7–1.8 g/cm^3 density and 220-240 GPa

Young’ s modulus and ~4,000 MPa tensile strength) with epoxy or polyester resins (with 1.1-1.3 g/cm^3 density, 2-4 GPa Young’ s modulus and 50~100 MPa tensile strength) (Veers, et al., 2003; Brondsted, et al., 2005; Haymen, et al., 2008).

Reliable energy supply is critical to global social-economic development and sustainable economic growth. Fossil fuels (e.g., coal, oil, gas) currently supply most of the global energy requirements (Dorian, et al., 2006; Dresselhaus, et al., 2001). However, to combat the global issues of climate change, greenhouse gases, and energy insecurity, renewable energy sources (e.g., wind, solar, bio, hydro, and marine energies) and energy-efficient technologies are essential to meet the increasing global energy demands (Asif & Muneer, 2007; Armaroli & Balzani, 2006). In recent decades, wind energy has been recognized as one of the critical renewable energy sources. Wind energy can play an important role in reducing the dependency on fossil fuels and provide opportunities for green electricity generation (Islam, et al., 2013; Herbert, et al., 2007; Quarton, 1998; Esteban, et al., 2011; Kaldellis & Zafirakis, 2011). The wind energy industry has a significant growth in recent years through onshore and offshore wind farms—with individual turbine capacity ranging from 1 to 7 MW (e.g., Vestas V-90 3.0 MW, Gamesa G-128 4.5 MW, Siemens SWT6-120 6 MW, Samsung S7-171 7.0 MW and Enercon E-126 7.5 MW) and the development of more giant turbines with 8~10 MW for offshore installation (e.g., Vestas V-164 8 MW).

From 2004 to 2014, the global installed capacity of wind power has been growing from 47 GW to 369 GW. As global wind energy growth stabilizes, China’ s growth is set to triple by 2025, reaching an estimated 347.2 GW by 2025, says Global Data (Pu, et al., 2017). Wind turbines are expected to have a service life of about 20 years. However, essential maintenance is critical to extend the life of ageing-damaged wind turbines and also to ensure that they last the expected service life. The composite blades, being the most significant dynamic structural components in a wind turbines, are especially prone to structural damage during service.

As the increased utilization of composite materials for wind turbines, the maintenance and repair of these components are vital to ensure that the performance of these composite components remain the same as they were initially designed (ASM International, 2002). There are many repair methods like patch repair by hand lay-up or by the use of prepreg. Besides that, there are injection repair and self-healing repair methods. Ultraviolet (UV) light curing technology is well established in many industries for its advantages like easy-operation, reduced costs and rapid production times (George, 2011). The resin formulated with a photoinitiator is the basic concept to realize the photopolymerization which initiates an extremely rapid cross-link cure mechanism, often complete in several minutes or even in several seconds as opposed to relative long curing time of conventional thermal polymerization resins, when under the exposure to UV irradiation (Li, et al., 2003). Photo polymerizable resins can also be cured with sunlight alone and are therefore more practical for field use where additional effort would be necessary to protect the joint from the environment during a lengthier cure, or impractical levels of energy are input into the system to quicken the cure (Jerry, et al., 2004). In this study, the photo polymerizable resin was especially suitable for the service environment of wind turbine blades and can improve the efficiency of repair because of its rapid curing behavior without an external heat source (Chen, et al., 2018; Chen, et al., 2019; Yu, et al., 2019; Park, et al., 2019; Choi, et al., 2019).

1.2 Research objectives

Currently the repair on the wind turbine blades are mostly the ‘cut out and fill’ type or the ‘wet lay-up’ techniques on the damaged GFRP parts. Especially the resins for wet lay-up need to be mixed on the ground prior and the most difficult aspect is the tool operation and curing process. In additional, the repair on the wind turbine blades must be conducted at local area, which meas even the well-trained skyworkers need to deal with the harsh working environment. Based on that, this dissertation aims to employ the photo polymerizable resin to conduct the wind turbine blades remediation as the alternative of conventional thermoset polymers. The major applications of photo polymerizable resins are coating, packaging, adhesives, graphics arts and automotive in terms of less energy consumption, less equipment space and lower temperature treatment. But the scholars about implement of photo polymerizable resin into fiber reinforced composite remediation aspects were found to be limited. The GFRP lamina shows inherent translucent feature and it can be penetrated by the UV irradiation, which overcome the main limitation of UV-penetration in thickness direction in photo polymerizable resins curing system. The main objective of this dissertation is to propose this remediation technique on GFRP parts of wind turbine blades utilizing photo polymerizable resins with the numerical/experimental properties assessment. The anticipant results of this dissertation are the good feasibility, good durability, compatible properties and reduced operation time of the photo polymerizable resins implemented GFRP remediation.

1.3 Chapter overview

Chapter 2 reviews the literature summary about fiber reinforced composite materials, fabrication, testing methods and different kinds of composite repair methods to represent the research status.

The GFRP repair process utilizing photo polymerizable resin is described in Chapter 3. The mechanical properties of patch-repaired unidirectional GFRP were investigated through experimental and numerical works.

In consideration of the environments in which wind turbine blades located, the properties under low temperature were evaluated in Chapter 4.

Chapter 5 demonstrated the durability in the acidic atmosphere on laminated specimens which were repaired by thermal or photo polymerizable resin separately.

Chapter 6 investigates the performance of repaired specimens and photo polymerizable resin during eight weeks of UV ageing process.

Chapter 7 is the summary and conclusions of this dissertation.

2. Literature Review

Since the mid-1960s, a large volume of literature has been published on various types of composite materials and their structural applications. Without even mentioning tens of thousands of journal articles and conference papers devoted to particular problems, there are hundreds of textbooks, reference books, manuals, handbooks, and also numerous review papers on the subject (Senthil, et al., 2017). The 'Literature review' chapter provides the fundamental to perform further studies. In this chapter, the summarization and review of literature are presented including the following aspects: Fiber reinforced composite materials, Fabrication techniques of composites, and Repair methods of composites.

2.1 Fiber reinforced composite materials

Fiber-reinforced composite materials consist of fibers of high strength and modulus embedded in or bonded to a matrix with distinct interfaces (boundaries) between them. Both fibers and matrix retain their physical and chemical identities, yet they produce a combination of properties that cannot be achieved with either of the constituents acting alone. In general, fibers are the principal load-carrying members, while the surrounding matrix keeps them in the desired location and orientation acts as a load transfer medium between them and protects them from environmental damages due to elevated temperatures and humidity. Thus, even though the fibers provide reinforcement for the matrix, the latter also serves several useful functions in a fiber reinforced composite material. The principal fibers in commercial use are various types of glass and carbon as well as aramid and basalt. Other fibers, such as boron, silicon carbide, and aluminum oxide, are used in limited quantities. All these fibers can be incorporated into a matrix either in continuous lengths or in discontinuous lengths. The matrix material may be a polymer, a metal, or a ceramic. Different chemical compositions and microstructural arrangements are possible in each matrix category. The most common form in which fiber-reinforced composites are used in structural applications is called a laminate. Fiber orientation in each layer, as well as the stacking sequence of various layers in a composite laminate, can be controlled to generate a wide range of physical and mechanical properties for the composite laminates (Mallick, 2007).

2.2 Fabrication techniques of composites

Autoclaves have become indispensable equipment for processing high-quality polymer composite aerospace/aircraft structural components (Upadhya, et al., 2011). Autoclaves are now being used to produce substantial aircraft components such as wing and fuselage. They can process a wide variety of materials, including thermoset and thermoplastic-based composite aircraft parts with varying contours and complex shapes. The autoclave curing process is achieved by placing the tools in a pressurized oven, each with a composite laminate on it. A typical three-stage cure cycle is depicted in Fig. 2 for a single part in the autoclave along time (Dios, et al., 2017). Luigi Nele, et al. (2016) defined a new parameter of the optimal positioning of the parts on the autoclave charge floor to characterize the part-tool assembly thermal and geometric properties. The authors found that the newly defined parameter allows to reduce the heating delay time and minimize the autoclave dwell time within the target temperature range. The time reduction of heating and cooling phase can enhance the clave productivity by reducing the overall autoclave cycle time. Khan, et al. (2017) achieved ramp rate up to 15 K min^{-1} via Quickstep processing and found that this technique allows alteration in chemo-rheology of 977-2A thermosetting resin, and so influences the reaction progress. Although the curing path is different from the autoclave curing, the final cross-linked structure is similar.

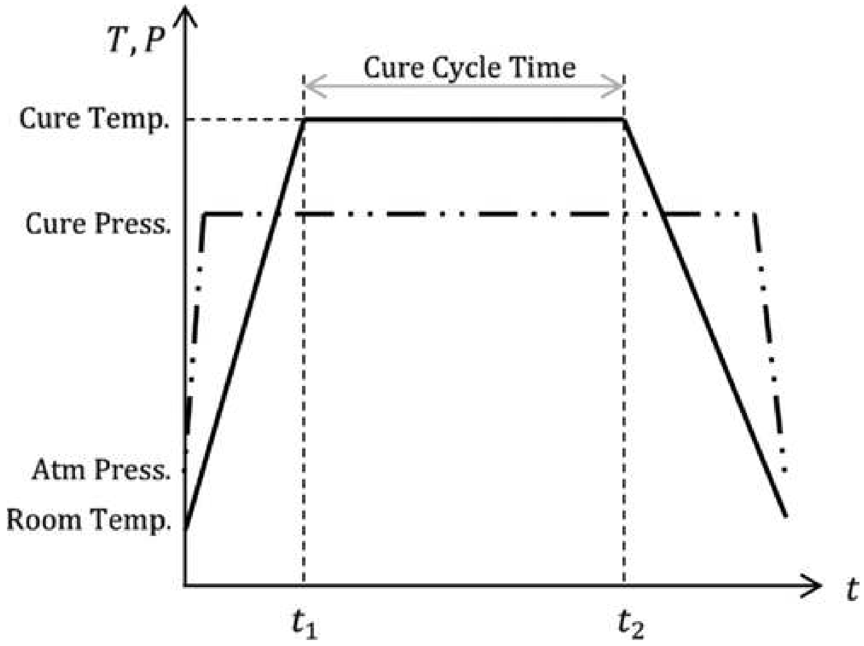

Fig. 2 Standard temperature (T) and pressure (P) cycle (Advani & Murat, 2010)

The vacuum assisted resin transfer molding (VaRTM) process, which has been developed during the past two decades and has many process variants, is now a widely used process for manufacturing fiber reinforced polymer composite laminates. The VaRTM process, which is a closed-mold process with reduced volatile organic compounds (VOC) emission, combines the benefits of high quality, repeatability and clean handling of the resin transfer molding (RTM) process with the advantages of flexibility and scalability of open-mold hand layup processing. However, VaRTM has various drawbacks such as (i) low impregnation velocity during mold filling leading to long cycle times, (ii) possibility of high void content in finished parts, (iii) non-uniform and limited compaction pressure on the fibers which cause spatial variations of laminate properties, (iv) lower fiber volume content (40–50%) compared to RTM and autoclave molding (65 and 70%, respectively), and (v) high surface roughness at the vacuum bag side of the part due to peel-ply (Advani & Sozer, 2010; Donaldson & Miracle, 2001; Abraham, et al., 1998). The VaRTM process plays many vital roles in promoting the quality, affordability and part complexity of substantial closed-mold FRP composite (Hsiao & Heider, 2012). The typical VaRTM setup is shown in Fig. 3. Yalcinkaya, et al. (2017) modified the conventional VaRTM process by external pressurization of a heated mold to increase fiber volume fraction and improve mechanical properties of laminates. It was observed that pressurized VaRTM can led to laminates with less than 1% void content. Besides, fiber volume fraction and flexural strength were increased by 25% and 13% concerning non-pressurized VaRTM, respectively. Mehrad, et al. (2018) used magnet assisted composite manufacturing (MACM) technique to fabricate high-quality VaRTM laminates and a new, transient process model for MACM is introduced. The flexural strength of the 6-ply, 12-ply, and 18-ply laminates was improved by more than 28%, 23%, and 11%, respectively. The flexural modulus was also enhanced substantially, at least by 41%, 34%, and 23%, for the same set of laminates. Matsuzaki, et al. (2011) investigates full-field monitoring of resin flow during a VaRTM process using an area-sensor array. The squared area sensors are aligned as a matrix on a thin polyimide film; thus the film measures the full-field flow monitoring and does not miss a dry spot that may occur anywhere on the film. As a result, the precise figurations of the flow front and the dry spot are successfully estimated in real time.

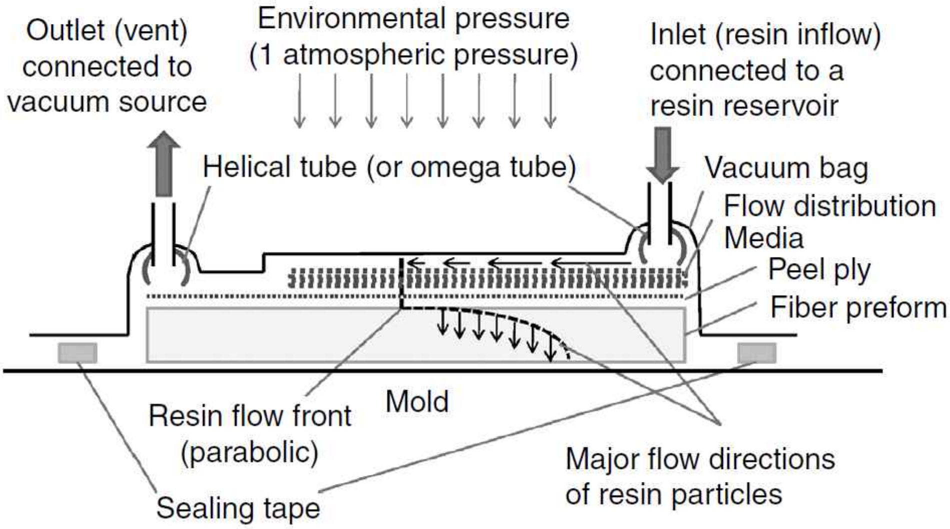

Fig. 3 Typical schematic of VaRTM setup (Hsiao & Heider, 2012)

A new generation of out-of-autoclave (OOA) prepregs has been introduced, and the experience with these prepregs has demonstrated that it is possible to produce autoclave-quality parts using vacuum-bag-only (VBO) consolidation (Ridgard, 2000; Ridgard, 2009; Ridgard, 2010; Boyd & Maskell, 2001; Repecka & Boyd, 2002). The main advantages of these materials are the ability to use lower cost tooling, combined with an increase in dimensional accuracy because of reduced tool thermal expansion. However, these benefits are outweighed by three major drawbacks: (1) relatively high porosity resulting from low applied pressure or inconsistent resin bleed, particularly for high fiber volume fraction reinforcements; (2) out-times, or allowable room temperature storage times, of only about a week; and (3) relatively low mechanical performance, particularly in terms of toughness. The key requirement for low porosity VBO-cured parts is the removal of entrapped air during lay-up. To this effect, VBO prepregs are ‘breathable’, featuring partially impregnated microstructures consisting of both dry and resin-rich areas which are shown in Fig. 4 and Fig. 5.

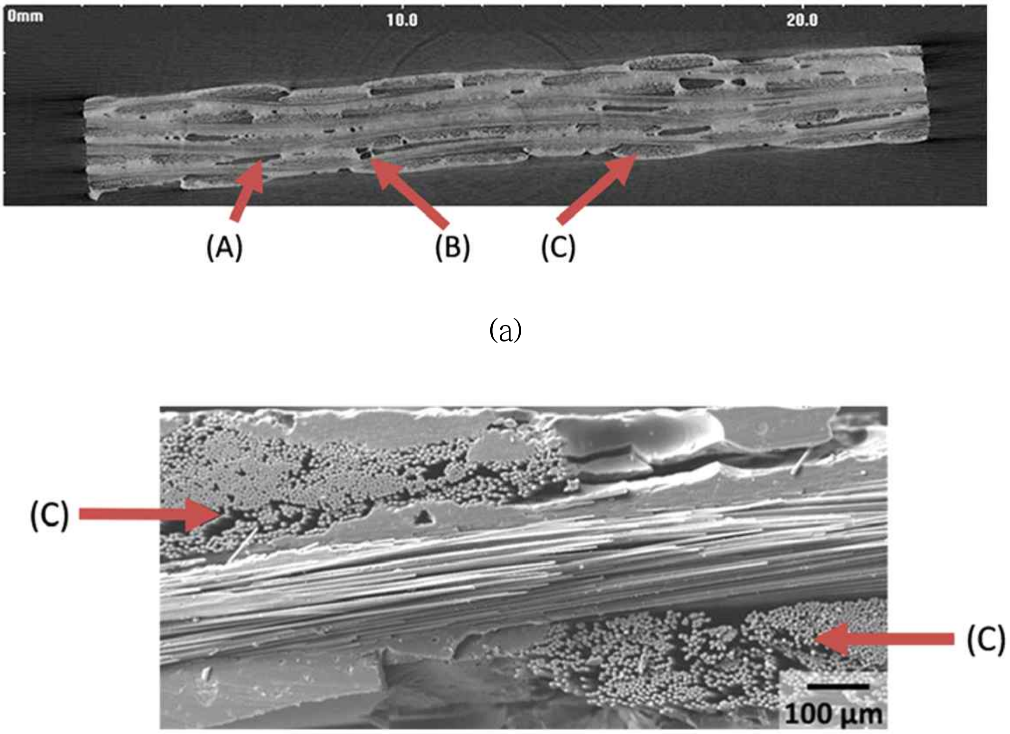

(a)

(b)

Fig. 4 (a) Micro-CT image showing the initial condition in a stack of prepreg plies, (b) SEM images of a single prepreg ply in the as-received condition. Void types are labeled with letters, (A) interlaminar voids, (B) inter-tow gaps, and (C) fiber tow voids (Grunenfelder, et al., 2013)

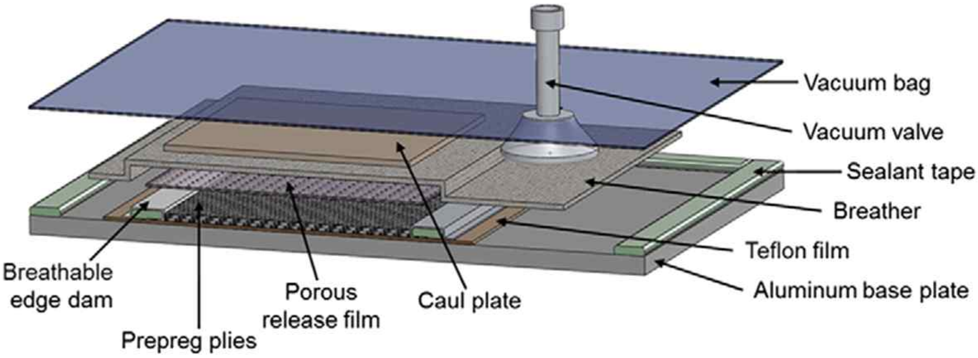

(a)

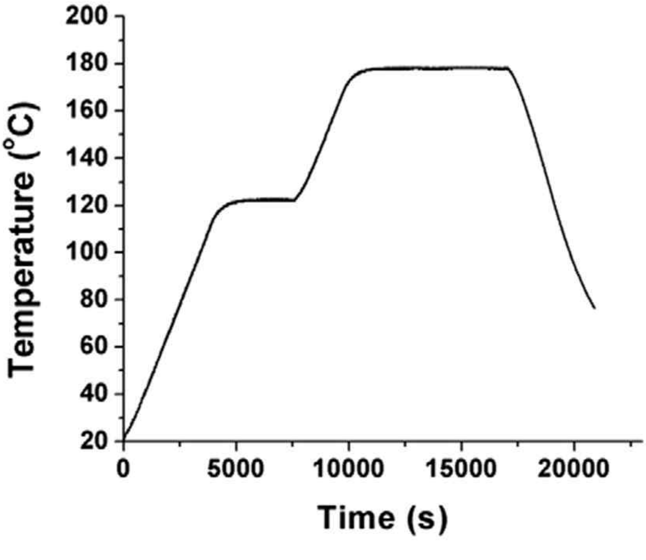

(b)

Fig. 5 (a) Vacuum bagging assembly for laminate manufacture, (b) thermocouple measurements of temperature at the tool surface (aluminum base plate) during the cure cycle (Grunenfelder, et al., 2013)

Lee, et al. (2010) developed reaction rate and viscosity models for a resin matrix (Cytec’ s Cycom 5320-1) using experimental data from DSC and RDA, along with two predictive approaches: look-up tables and neural networks. Both reaction rate models showed acceptable performance, with the neural net approach capturing the second half of the reaction (and thus the shift to diffusion-controlled cure) more accurately. Likewise, Kratz, et al. (2012) characterized the cure kinetics, viscosity and glass transition temperature for two commercial VBO prepregs (ACG’ s MTM45-1 and Cytec’ s Cycom 5320). DSC, RDA, and DMA experiments were carried out in various process conditions, and the resulting data were used to develop semi-empirical analytical models that effectively predicted these properties for any time-temperature cycle.

Additive manufacturing (AM) is defined as ‘a process of joining materials to make objects from 3D model data, usually layer upon layer, as opposed to subtractive manufacturing methodologies’ . AM technologies create possibilities to build an extensive range of prototypes or functional components with complex geometries those are unable or at least difficult to be manufactured by conventional methods (Alimardani, et al., 2007; Yakovlev at al., 2005). AM techniques include stereolithography apparatus (SLA) from photopolymer liquid (West, et al., 2001), fused deposition modeling (FDM) from plastic filaments (Dudek, 2013), laminated object manufacturing (LOM) from plastic laminations (Park, 2000), and selective laser sintering (SLS) from plastic powders (Kruth, 2003). However, FDM is the most widely used method among all the AM techniques for fabricating real plastic parts with low cost, minimal wastage, and ease of material change. Zhong, et al. (2001) modified the ABS filaments for FDM prototyping by incorporation several different modifiers including the short glass fiber, plasticizer, and compatibilizer in order to overcome the deficiency of neat ABS such as low strength and hardness. The result showed that the mentioned two properties were improved by adding a small amount of plasticizer and compatibilizer. Ning, et al. (2015) attempted to modify the neat thermoplastic materials using for FDM technologies by adding carbon fibers to form the thermoplastic matrix CFRP composites. After FDM fabrication, effects on tensile and flexural properties were evaluated, and the results showed increased tensile and flexural strength with decreased toughness, yield strength, and ductility.

2.3 Repair methods of composites

Structural repairs can be performed by mechanical fastening, adhesive bonding, and hybrid fastening and bonding. The damaged material is first cut out as a straight-sided hole on which an external doubler is attached, referring to Fig. 6(a), or sculptured to form a scarf of shallow angle to accommodate a scarf patch, referring to Fig. 6(b). The repair patch can be then attached using mechanical fasteners or adhesive bonding. Cross-sectional views of the resulting repairs are shown in Fig. 7 and Fig. 8, respectively. While the primary intent of internal repair is to ensure that the repaired component conforms to the external shape of the structure, a low-profile doubler is acceptable in the majority of aircraft applications. Historically, Wang, et al. (2015) and Goh, et al. (2013) developed adhesively bonded repair concepts and design methodologies to address secondary structures, without considering some of the critical design requirements faced by safety-critical structures. For example, existing design methodologies proposed by Wang, et al. (2018) for internal (scarf) repairs are commonly based on analyzing the pristine joints as illustrated in Fig. 8(c). In other words, the ultimate load-carrying capacity of the repair is calculated without considering any disbond and delamination. Chun, et al. (2009) found that the platform of the scarf repair depends on the laminate layup (which affects the orthotropy of the composite) and the applied loads. This design methodology of analyzing the pristine joints and repairs, however, is not suitable for safety-critical aircraft structures, because recent airworthiness regulations require that the repaired structure can restore the damage tolerance and fatigue durability of the original structure. The primary design requirements include the scarfed structure, without repair, as illustrated in Fig. 9(a), must be able to sustain the design limit load. This requirement stems from the current lack of nondestructive inspection techniques that can detect weak bonds (Da, et al., 2011). The repaired structure must be able to carry the design ultimate load even in the presence of allowable damage such as disbond or impact damage, as illustrated in Fig. 9(b), and can reach the fatigue endurance of the original structure.

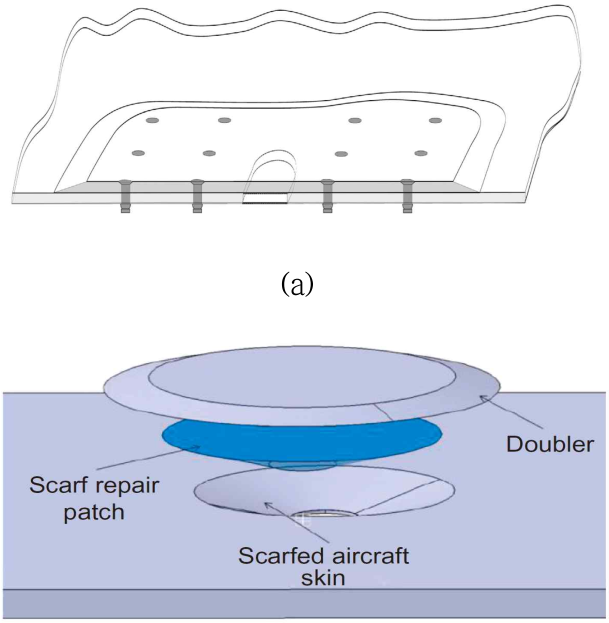

(a)

(b)

Fig. 6 Structure repairs: (a) external doubler repair and (b) scarf repair (Chun & Duong, 2015)

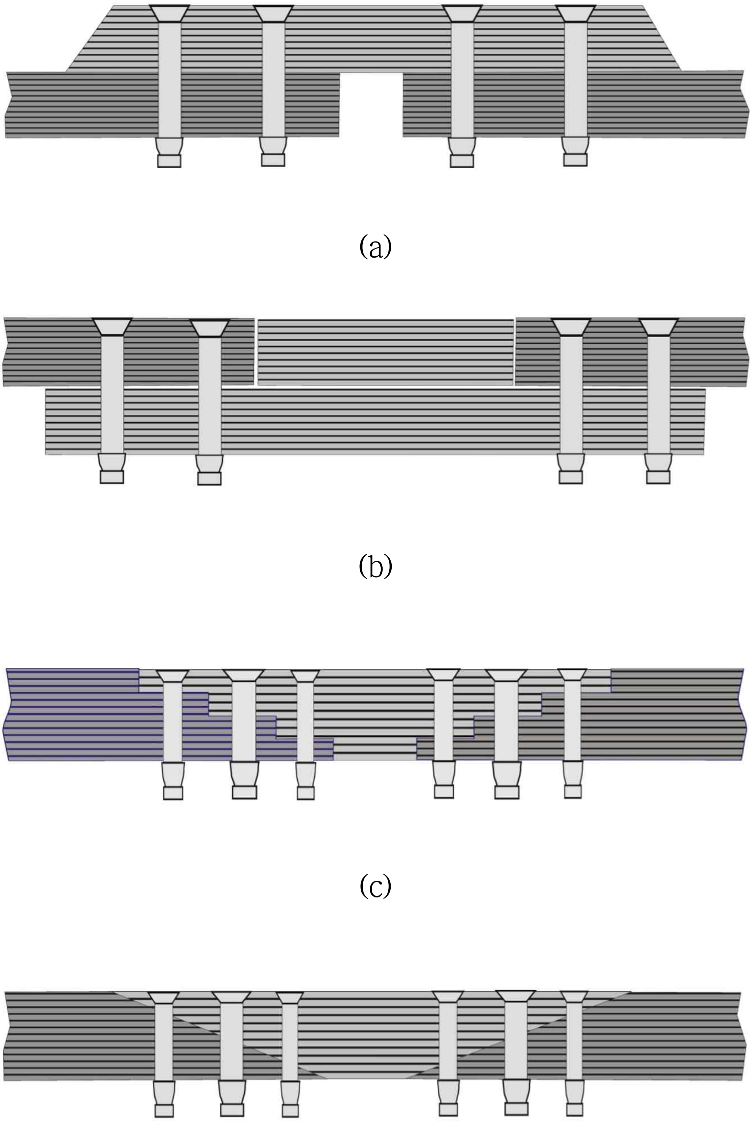

(a)

(b)

(c)

(d)

Fig. 7 Cross-sectional views of mechanically fastened repairs: (a) external doubler bolted repair (small damage), (b) internal bolted repair (large damage), (c) internal multistep bolted repair, and (d) internal scarf bolted repair (Chun & Duong, 2015)

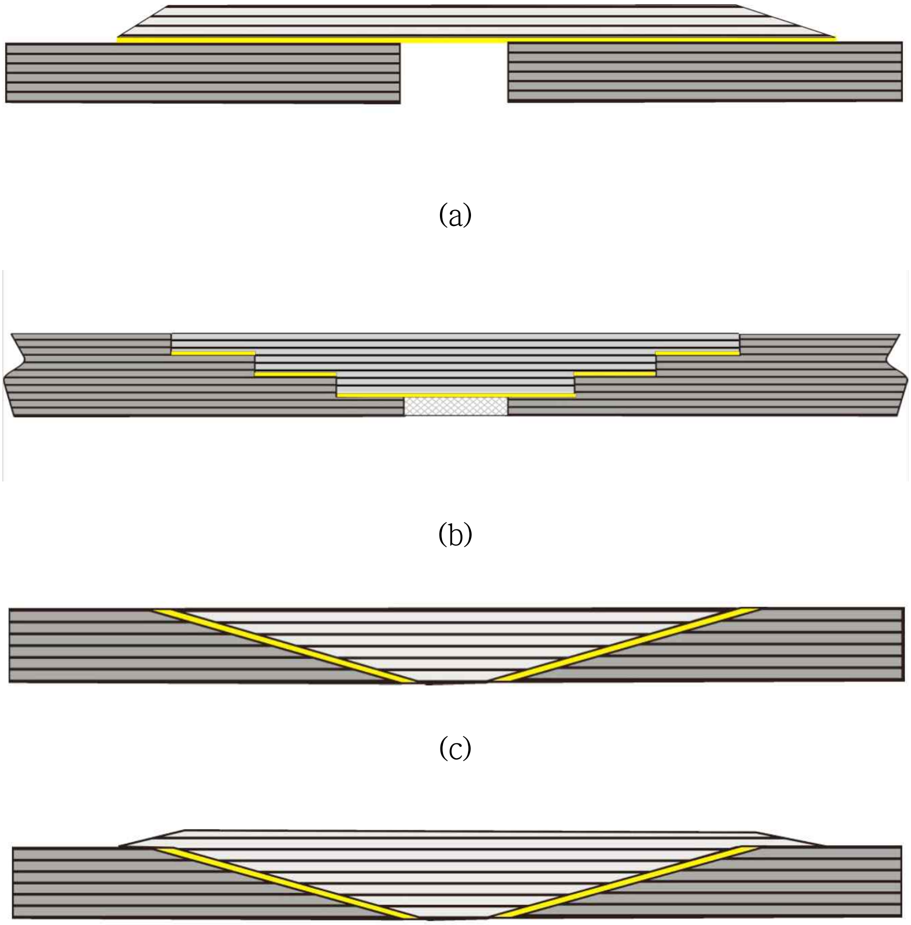

(a)

(b)

(c)

(d)

Fig. 8 Cross-sectional views of adhesively bonded repairs: (a) external doubler bonded repair, (b) internal multistep bonded repair, (c) internal scarf bonded repair, and (d) doubler-scarf repair (Chun & Duong, 2015)

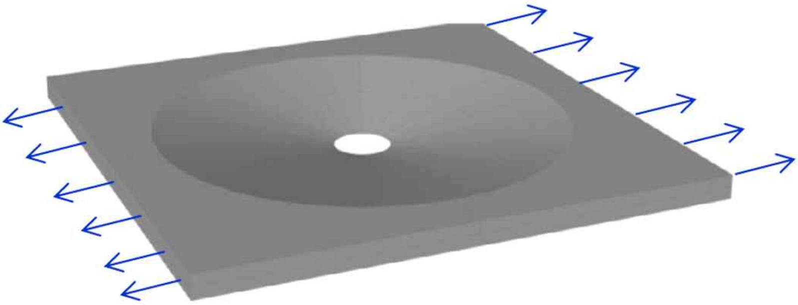

(a)

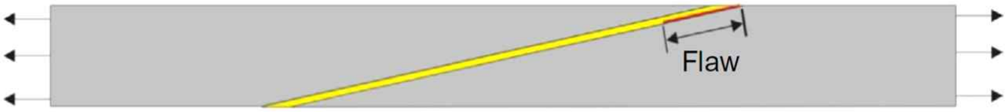

(b)

Fig. 9 Cross-sectional views of adhesively bonded repairs: (a) external doubler bonded repair, (b) internal multistep bonded repair, (c) internal scarf bonded repair, and (d) doubler-scarf repair (Chun & Duong, 2015)

3. Experimental and Numerical Analysis of UV repaired GFRP

In this chapter, the mechanical properties of patch-repaired unidirectional GFRP are investigated by experimental and numerical works. The specimens were repaired by photo or thermal polymerizable resins though stacking the external glass repair patches onto pre-damaged position followed by specified curing methods. The numerical work was proceeded in commercial program ABAQUS. Continuum shell (SC8R) was used to generate the composite layup, and discrete rigid body (R3D4) was selected to define the loading indenter. Cohesive elements were implemented between the repair patches and fundamental specimens by surface-based contact algorithm. Hashin damage criterion was determined to initiate and propagate the intralaminar failure of the laminae. Quadratic stress criterion and Benzeggagh-Kenane criterion were used to simulate the interlaminar failure. Additional DCB and ENF tests were conducted to determine the interlaminar critical strain energy release rate required in damage criterions. The experimental result shows that UV repaired specimens performed higher ultimate strength in both tensile and bending tests compare to RT repaired specimens. The results of numerical works are quite comparable with the experimental data. Stress concentration was observed at center hole and edges of repair patches on tensile specimens. Cohesive failures occuered at edges of repair patches on tensile specimens and areas near loading indenter on bending specimens, respectively. Through the results of experimental and numerical works, the feasibility and reliability of patch repair method utilizing photo polymerizable resin are deeply validated.

3.1 Introduction

Ultraviolet (UV) light curing technology is well established in many industries like inks, adhesives, and coatings for its advantages like easy-operation, reduced costs and rapid production times (Marsh, 2011). Traditional cure methods for thermoset-based composites involve the addition of a hardener or catalyst to the resin for an ambient temperature cure followed by a thermal post-cure treatment full cure (Di & Compston, 2009). The resin formulated with a photoinitiator is the basic concept to realize the photopolymerization which initiates an extremely rapid cross-link cure mechanism, often complete in several minutes or even in several seconds as opposed to several hours (epoxies and prepregs), when under the exposure to UV irradiation (Jefferson, et al., 2018). photo polymerizable resins can also cure with sunlight alone and are therefore more practical for field use where additional effort would be necessary to protect the joint from the environment during a lengthier cure, or impractical levels of energy are input into the system to accelerate the cure (Peck, et al., 2004).

Fiber reinforced plastic consists of high-performance fibers dispersed in a polymer matrix, because of their stiffness, high strength-weight ratio, fiber reinforced plastics have reached application in transportation and sporting goods, replacing metal materials (Pilar, et al., 2013; Chukov, et al., 2015; Kim & Mai, 1991; Ellakwa, et al., 2002). However, unlike metal materials, non-visible and visible irreversible failures may have occurred in FRP, annealing/or reworking on the FRP are infeasible (Reid & Zhou, 2000). The repairs made on damaged areas in order to achieve the original mechanical properties tend to vary depending on the type of failure. Once the damage is detected, and the effects on the residual properties of the structure have been predicted, a decision must be made as to whether this composite part should be repaired or replaced (Kara, et al., 2015; Serge, 1998). The repair techniques used recently are the scarf and lap (single or double) repair by wet hand lay-up or by the use of prepreg (Wang, et al., 2018; Budhe, et al., 2018). The investigation of a remediation methodology of FRP to achieve rapidly and cost-effectively repair is necessary.

Li, et al. (2003) drawn a conclusion that the photo polymerizable resins is a fast, reliable, durable, and cost-effective repair method and can replace the ambient environment curing resin and the heat activated prepreg resin. For UV curing resin repaired samples, conditioning by UV radiation can increase the residual tensile strength. Hasiaoui, et al. (2018) manufactured GFRP and found that when applying more protracted vacuum and impregnation steps, the specimens can lead to high flexure and shear strength. Pu, et al. (2017) successfully adhered a cationic photo polymerizable resin to a damaged CFRP panel due to its characteristic of dark polymerization after UV exposure and the lap shear testing showed the shear stress was above 1,000 psi. Bao, et al. (2018) proposed a simple method for repairing interlaminar cracking in GFRP and conducted DCB test after repair. The authors found the 63% reverse of mode I fracture toughness and suggested the feasibility of the proposed simple repair method for GFRP.

Because it is relatively difficult to obtain the stress distribution and internal damage criterion during the experimental work, the finite element method (FEM) was adopted to do the analysis (Liu, et al., 2016; Vilanova, et al., 2016; Wang, et al., 2014). Some finite element-based composite damage models are available in commercial FEM softwares. Examples include the ABAQUS built-in progressive composite damage model based on the work by Matzenmiller, et al. (1995); and the LS-DYNA (Hallquist, 2006) material model type 262 which uses an approach based on the failure criteria presented by Chang and Chang (1987). Despite the widespread application of these commercial packages, calibration of non-physical parameters to control the damage propagation is generally required. Also, the reliability and feasibility of experimental works can be validated by comparing the date with the simulation result. Furthermore, the positive and negative feedbacks can be obtained for further optimization of experimental designs (Yan & Lin, 2016; Kong, 2018).

In this chapter, GFRP specimens were conducted to patch remediation by utilizing photo and thermal polymerizable resins. Mechanical properties including tensile and bending behaviors were evaluated by experimental and numerical works. Hashin damage criterion was implemented to initiate and propagate the intralaminar failure, while quadratic stress criterion and Benzeggagh-Kenane criterion were employed to simulate the interlaminar failure. Comparative analysis was conducted between experimental and numerical works.

3.2 Experimental works

3.2.1 Materials

Unidirectional glass fabrics (EJ-90, Haining Anjie Composite Material Co., Ltd.) were selected as the reinforcement in fundamental specimen fabrication and glass repair patches. photo polymerizable resin (TB 3033B, supplied by ThreeBond Holdings Co., Ltd.) was used in external glass repair patches for specimens remediation. Thermal polymerizable resin (KFR-120V, supplied by KUKDO chemical Co., Ltd) and hardener (KFR-141, supplied by KUKDO chemical Co., Ltd), with a mixture ratio of 100:30, were used as the matrix for fundamental specimens and glass repair patches.

3.2.2 Fundamental specimens fabrication and remediation

The fundamental specimens preparing for further repair were fabricated using wet prepreg manufacture technique. During the processing, 9 layers laminate of unidirectional glass fabrics arranged $[0/+45/-45]_3$ stacking sequence with dimensions of 300 mm×500 mm were implemented as the reinforcement, with the polymer matrix composed of epoxy resin and hardener. All laminates were adequately impregnated by resin and consolidated by FRP roller, a piece of peel ply and several piles of breathers were then covered upon the glass laminates. A vacuum pump was connected to the mold and vacuum phenomenon was conducted for estimating entrapped air and redundant resin after all laminates were sealed. The photograph of fundamental specimen fabrication processing is shown in Fig. 10. Wet prepreg set-ups were stored in the oven for curing processing at 80℃ and settled for 12 hours with uniformed heating and cooling rate of 30 minutes. After demolding, the fundamental samples were cut into tensile and bending specimens by CNC cutting machine. The configuration of specimens was strictly abide by ASTM standards.

Glass repair patches were proceeded surface treatment in 5 wt.% NaOH solution bath with 3 hours heating at 80℃, then rinsed by distilled water sufficiently and dried by hot plate prior to the repair step for removing the contamination. In repair procedure, every specimen was ground by sanding machine (Model 3037 supplied by Astro Pneumatic Co., Ltd) on the patch-attaching areas in order to increase the surface roughness and to slightly reduce the thickness. The tensile specimens have a rectangular dimension of 36mm × 200mm × 3mm according to ASTM D 3039. The tensile specimens were firstly pre-damaged by an electrodrill in the middle (Φ = 6 mm), followed by three glass repair patches with dimensions of 36 mm ×36 mm and stacking sequence of [0/+45/-45] attachment on ground surface after penetrated by photo or thermal polymerizable resin (weight ratio of resin: hardener = 100:30). An extra piece of double-sized cover layer (72mm

× 36mm) with the zero degree stacking direction was then attached upon. The photograph and schematic of the tensile specimen remediation are shown in Fig. 11. Bending specimens also have the configurations according to ASTM D 790 of 12.7mm × 127mm × 3mm. Similar to tensile specimens, four fully-covered and resin-impregnated glass fabric patches were attached on the ground bending specimen surface to conduct the repair processing. The repaired specimens by using photo polymerizable resin are tagged as 'UV repaired specimens', while the repaired specimens by using thermal polymerizable resin are tagged as 'RT repaired specimens'.

For conducting the curing processing of repaired specimens, a piece of transparent bulky glass sheet was put on the repaired specimens with a hole in the center as the venting gate. After that, a vacuum bag was covered upon and sealed to conduct vacuum phenomenon by vacuum pump for conducting the uniform pressure on the repaired part, which is shown in Fig. 12. Curing processing were conducted under ultraviolet (UV) environment for UV repaired specimens or under an ambient environment for RT repaired specimens. The UV curing was realized by irradiation under 365 nm wavelength ultraviolet by the implementation of UV lamp (UV Cure-60PH, supplied by LICHTZEN Co., Ltd) for 10 minutes and the RT curing was conducted in ambient temperature for 24 hours. The repaired specimens were then mold released and stored for testing.

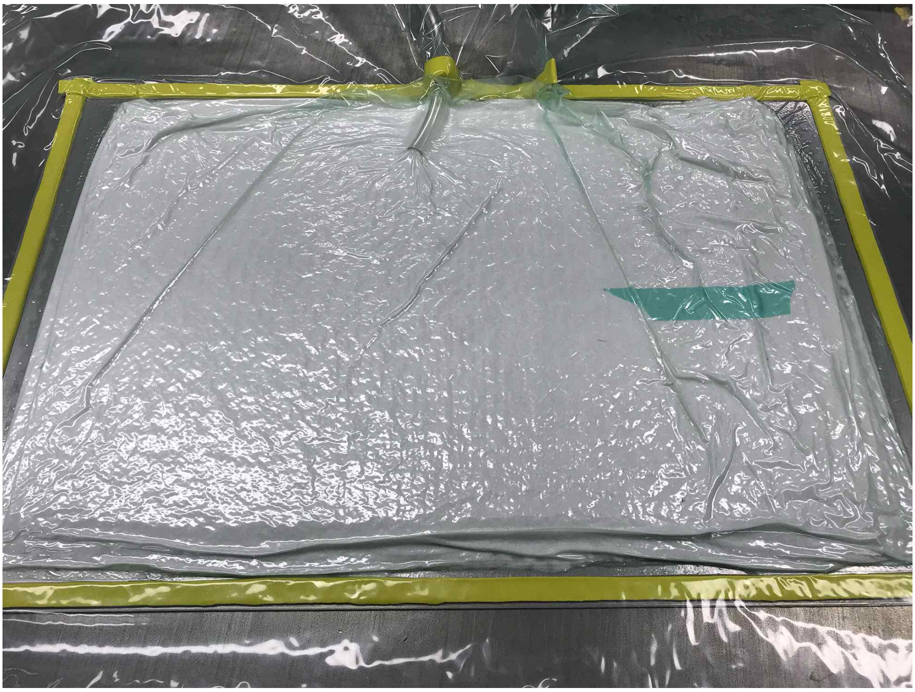

Fig. 10 Photograph of fundamental specimen fabrication processing

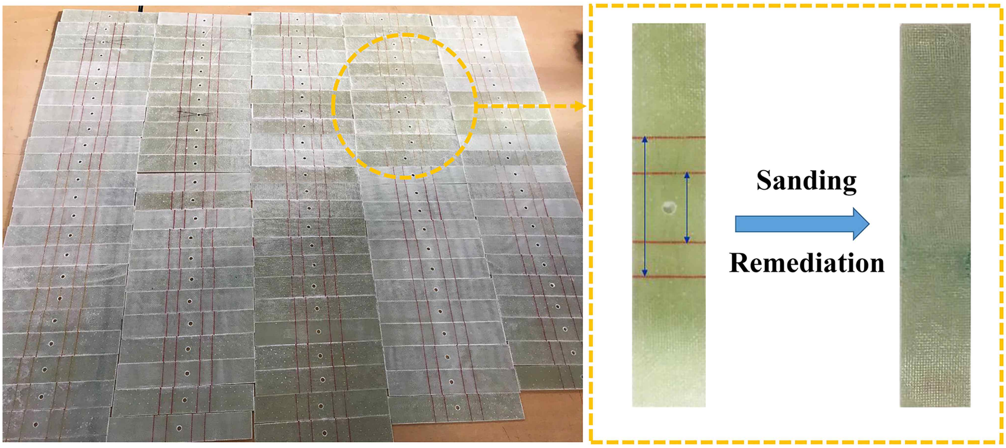

Fig. 11 Photograph and schematic of tensile specimen remediation

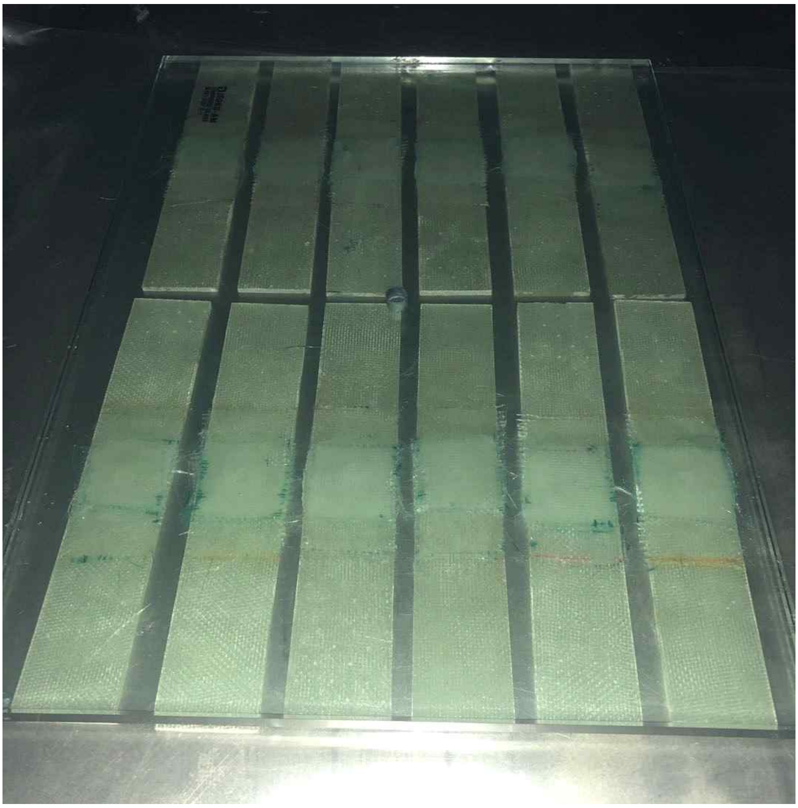

Fig. 12 Remediation set-up of repaired tensile specimens preparing for curing

3.2.3 Characterizations

Tensile and bending tests were both carried out utilizing a universal testing machine (UTM KDMT-156) with a displacement rate of 2 mm/min according to ASTM D 3039 and ASTM D 790, respectively. Least of ten specimens were individually conducted to the tensile and bending tests.

3.2.4 Experimental results and discussion

The experimental results of bending and tensile of both RT and UV repaired specimens are shown in Fig. 13. According to the test results, UV repaired specimens had the ultimate tensile and bending strength of 257 MPa and 396 MPa, which are both higher than RT repaired specimens. The results in ultimate tensile and bending strength indicate that the RT repaired specimens have the weaker bonding between the repair patches and the fundamental specimens, in contrast to the UV repaired specimens. The typical load-displacement curves of tensile and bending tests of both repaired conditions are shown in Fig. 14. During the tensile test shown in Fig. 14(a), smooth and steady load-displacement curves can be obtained in both repair conditions. A distinction of ultimate strength and the elongation at break is caused by the different interfacial bonding strength between patch and fundamental lamina at different curing and test conditions. The elastic modulus of two load-displacement curves are almost the same because the repair method of attaching an external patch had negligible contribution to the improvement of tensile modulus. The strengthened phenomenon can be verified by the macroscopic fracture morphology which presents the alteration of the failure pattern from adhesive debonding and delamination into integral breakage at the drilled hole. On the contrast, the curves of the bending test shown in Fig. 14(b) illustrates a rough and unstable failure process, and the UV repaired specimens presents the multi-stage plateau fracture phenomenon before critical failure. The fracture pattern of UV repaired specimen reveals the impediment of crack propagation which leads to a delayed failure and a higher ultimate strength. The outstanding properties of photo polymerizable resin contributes to a higher ultimate strength and modulus which revealed a strengthened interfacial bonding between repair patches and fundamental specimens.

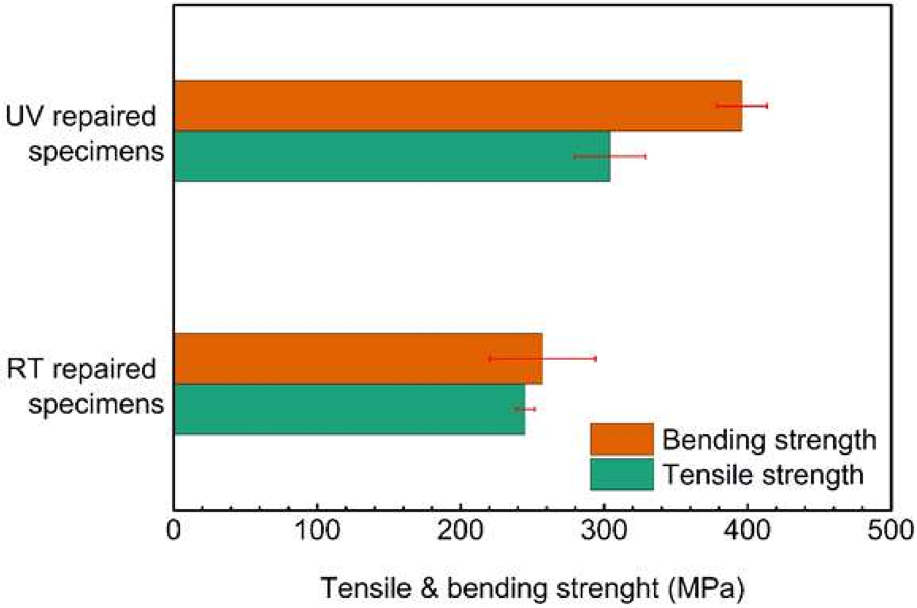

Fig. 13 Experimental results of tensile and bending tests

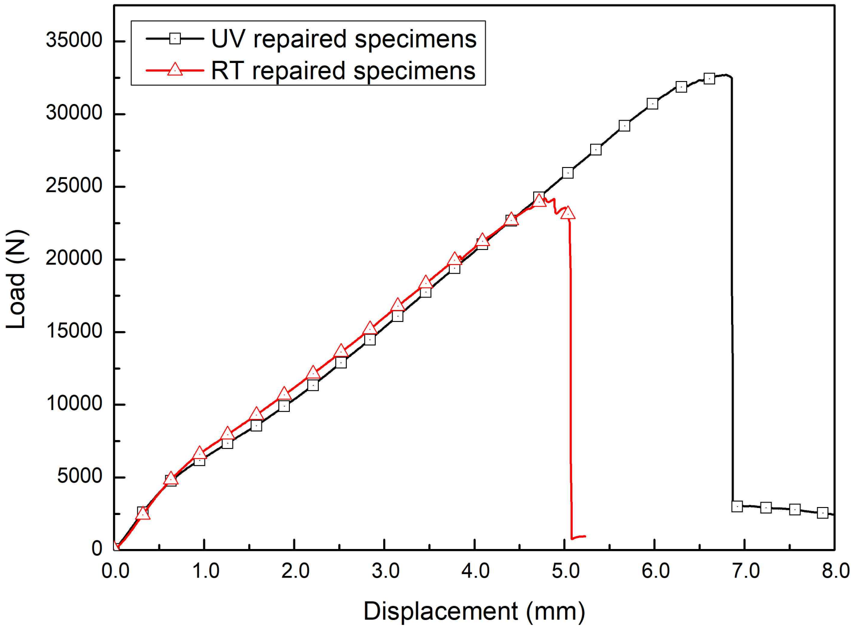

(a)

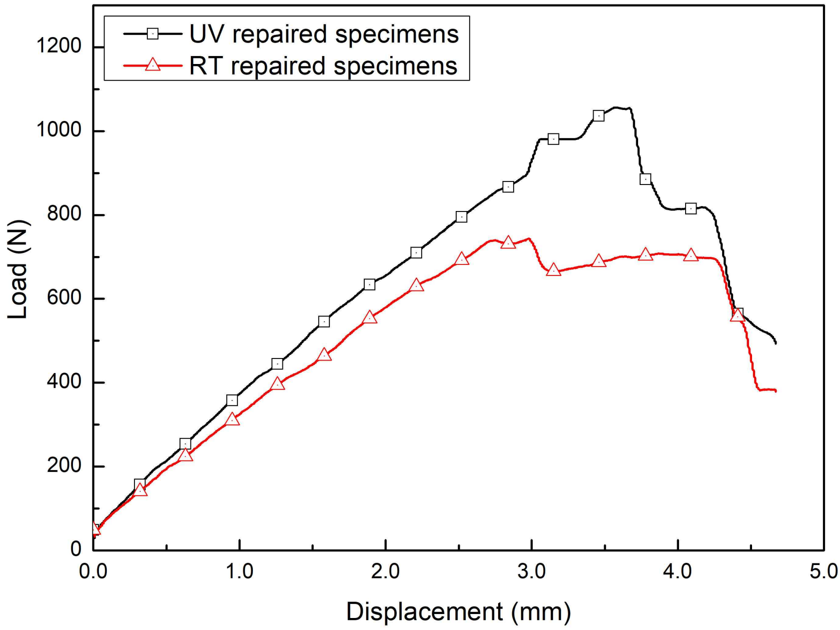

(b)

Fig. 14 Typical tensile (a) and bending (b) load-displacement curves of different repaired conditions

3.3 Numerical works

3.3.1 Material properties determination

To realize simulation on FRP laminates, interlaminar and intralaminar property parameters need to be imported. Strength parameters are necessary to introduce the Hashin damage criterion. In order to determine the mode I (G_{IC}) and mode II (G_{IIC}) interlaminar fracture toughness, double cantilever beam (DCB) and end-notched flexure (ENF) tests were conducted according to ASTM D 5528 and ASTM D 7905, respectively. For fabricating the DCB and ENF specimens, two separated GFRP specimens containing 5 laminates were prepared by wet prepreg manufacture technique as mentioned before. The two GFRP specimens were then bonded by photo, or thermal polymerizable resins as the adhesives with one piece of Teflon ply inserted to realize the initial crack on the intermediate slit of the DCB and ENF specimens. The specimens were then conducted to the same curing processing with tensile and bending specimens. For the convenience of the measurement of crack propagation length, calibrations were painted on the side face of the DCB specimens. The test parameters were strictly complied with ASTM and the displacement rate of both tests were 1 mm/s. The ultimate tensile strength and elastic modulus of neat polymer resins were obtained by tensile test on the cured resin specimens fabricated utilizing rubber mold. The photographs of DCB, ENF and resin specimen tensile tests processing are illustrated in Fig. 15, Fig. 16 and Fig. 17, respectively. Fig. 18 shows the typical load-displacement curves of photo and thermal polymerizable resin bonded DCB specimens. The photo polymerizable resin bonded DCB specimens exhibit a better crack propagation impediment comprehensively according to the load-displacement curves. The values of G_{IC} and G_{IIC} were both calculated using compliance calibration method. The central concept of this method is to introduce a component n, defined as the slope after the least squares fit of the log-log plot of crack length and the compliance, during the calculation. The primary material properties of unidirectional glass laminae, thermal polymerizable resins (KFR-120V) and photo polymerizable resins (TB 3033B) used in numerical works are shown in Table 1.

Table 1 Basic material properties for simulation

Properties	KFR-120V	TB 3033B	Glass lamina (KFR-120V)	Glass lamina (TB 3033B)
Density (tonne/mm^3)	1.16e-9	1.08e-9	1.85e-9	1.77e-9
E_{11} (MPa)	3.01e3	4.71e3	1.54e6	1.74e6
E_{22} (MPa)	3.01e3	4.71e3	3.73e4	3.96e4
E_{33} (MPa)	3.01e3	4.71e3	/	/
Nu_{12}	0.3	0.3	0.3	0.3
G_{12} (MPa)	2.02e3	2.7e3	3.98e3	4.14e3
G_{13} (MPa)	0.79e3	1.04e3	3.98e3	4.14e3
G_{23} (MPa)	0.79e3	1.04e3	3.29e3	3.75e3
X^T (MPa)	/	/	775	850
Y^T (MPa)	/	/	59	62
X^C (MPa)	/	/	430	520
Y^C (MPa)	/	/	300	320
S_{12} (MPa)	/	/	40	58
S_{21} (MPa)	/	/	10	12

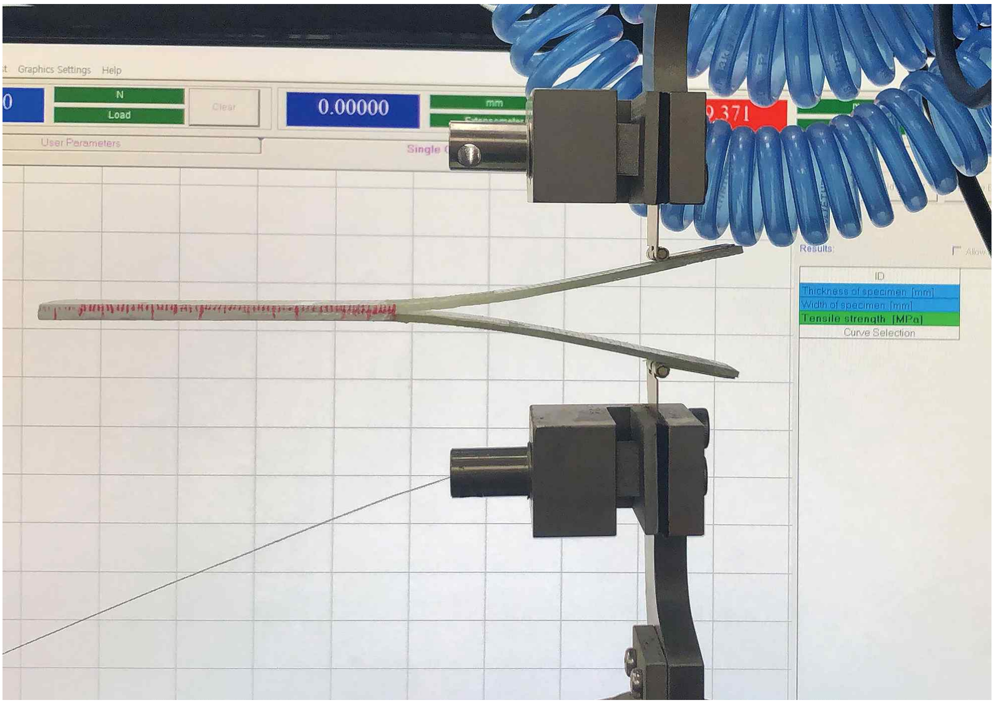

Fig. 15 Photograph of DCB test processing

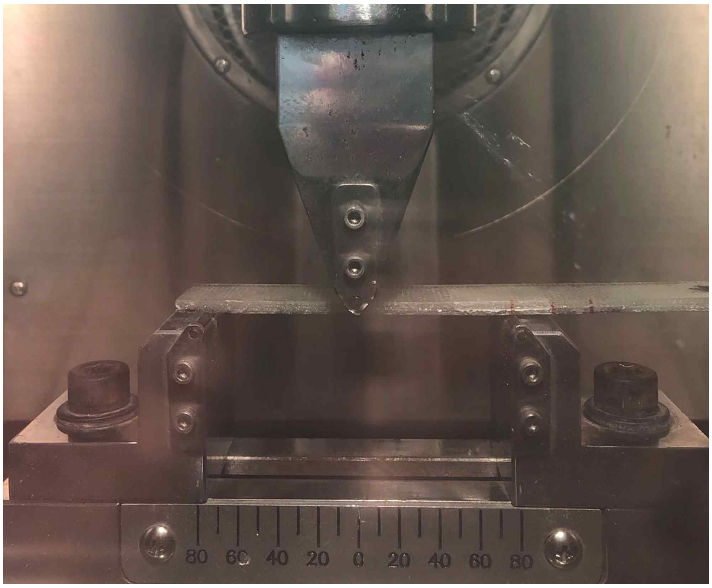

Fig. 16 Photograph of ENF test processing

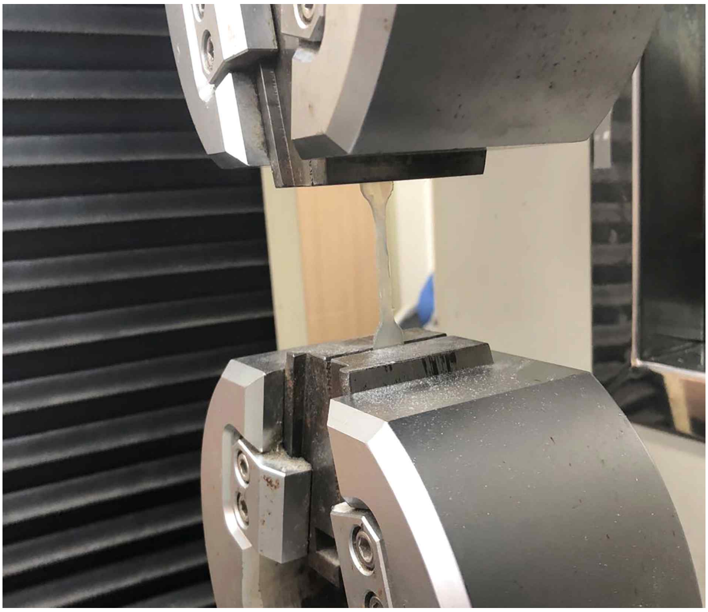

Fig. 17 Photograph of resin specimen tensile test processing

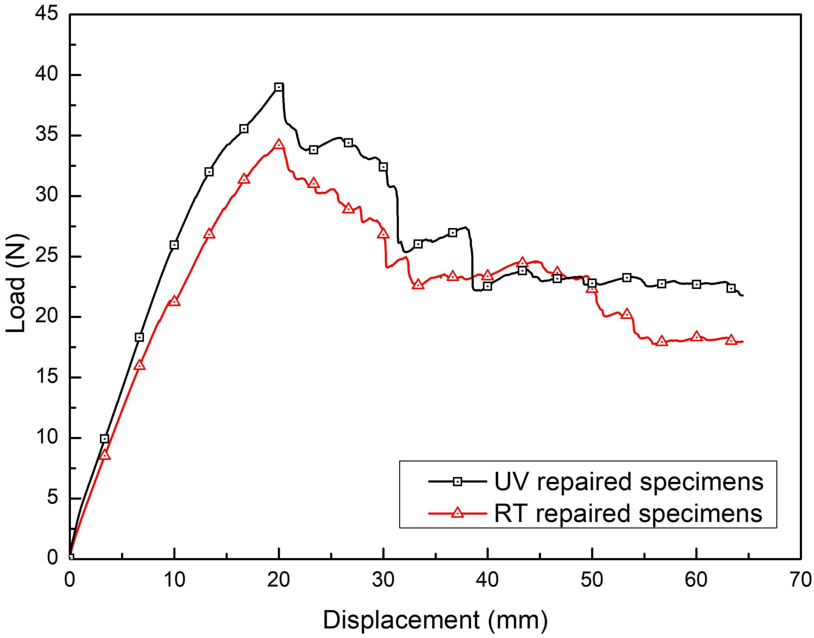

Fig. 18 Typical load-displacement curves of photo and thermal polymerizable resins bonded DCB specimens

3.3.2 Geometry and material properties

Tensile and bending specimen models built in ABAQUS are shown in Fig. 19 and Fig. 20, respectively. The configurations of numerical specimen models were the same as the experimental specimens. The solid type models were used, and the section assignment was realized by continuum shell (SC8R) composite layup options which also assigned the same ply number and orientation with experimental specimens (Khalili, et al., 2011; Smojver & Ivančević, 2011). For tensile test processing, the boundary condition was controlled by two reference points coupling on the load-applied surfaces. For bending test processing, the loading indenter and supports were defined using discrete rigid body (R3D4) with cylindrical surfaces. The boundary conditions were added on the loading indenter and supports, the specimen suffered bending stress by surface interaction definition (Shi, et al., 2012; Buitrago, et al., 2010). Both tensile and bending specimens were meshed using sweep mesh technic with the sweep path corresponding with the laminate stack direction. The cohesive element was added between the fundamental specimens and external repair patches by surface-based contact method, and the thickness of the cohesive element was assigned to zero. The interfaces between external patches and fundamental specimens were represented using the penalty contact algorithm with a measured friction coefficient of 0.2 (Tan & Falzon, 2016). Hashin damage criterion was selected for fiber laminates, and traction damage behavior was selected for cohesive elements. For both tensile and bending simulation, the ABAQUS/EXPLICIT solver was implemented during the processing.

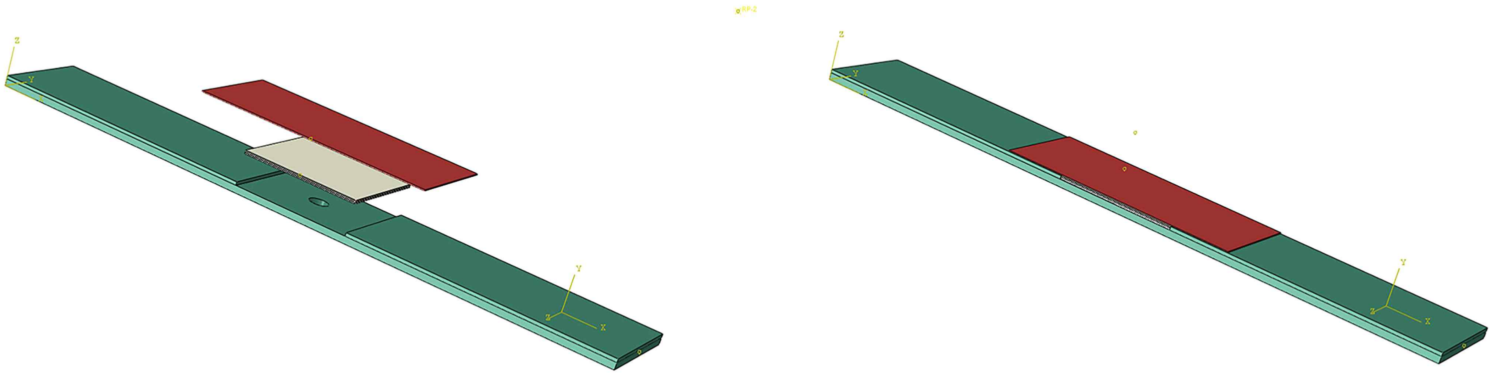

Fig. 19 Tensile specimen model built in ABAQUS

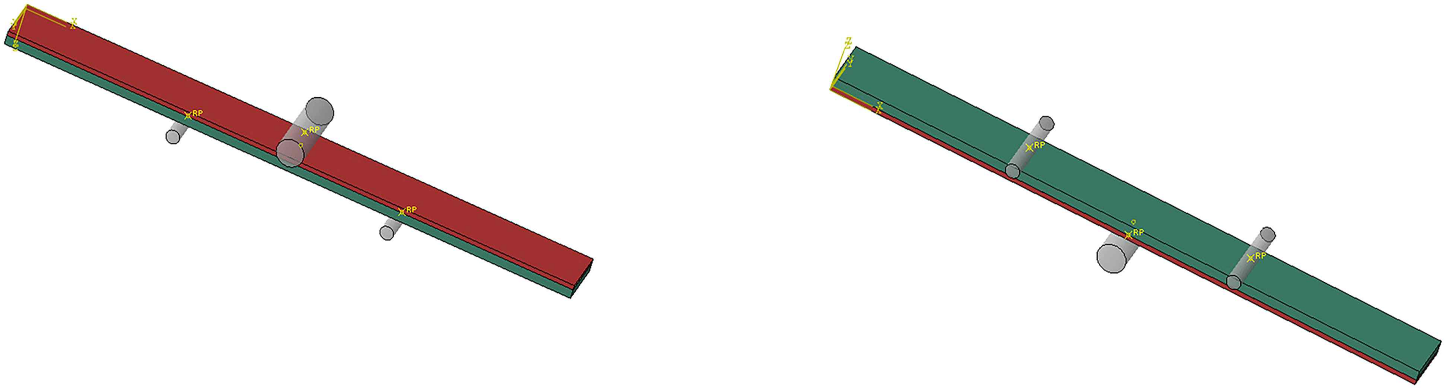

Fig. 20 Bending specimen model built in ABAQUS

3.3.3 Intralaminar damage model

During the numerical analysis, the failure modes of composite materials like tensile or compressive cracking, fiber-matrix shear-out and delamination can all represent the load capacity of the repaired patches and thus, the repair feasibility. It's very important to implement a well-established and proper damage criterion to do the failure analysis. The intralaminar damage model used in this numerical work was based on the Hashin damage criterion proposed by Hashin and Rotem (1973). Unlike the polynomial criteria such as the Tsai-Hill and Tsai-Wu criteria (1971), which propose a single equation to predict damage initiation. Hashin damage criterion (Hashin, 1980) separate the criterion for matrix failure mode from the criterion for fiber failure mode. The Hashin damage criterion, implemented in ABAQUS to analyze the progressive failure of the repaired specimens, is applied to identify the damage initiation in the numerical works of this chapter. The Hashin damage criterion contains four kind failure modes: (i) fiber breakage in tension (F_f^t), (ii) fiber buckling in compression (F_f^c), (iii) matrix cracking in tension (F_m^t) and (iv) matrix crushing in compression (F_m^c). The Hashin damage criterion is shown as the following equations:

$$F_f^t = \left(\frac{\sigma_{11}}{S_{t1}}\right)^2 + \alpha\left(\frac{\sigma_{12}}{S_{S12}}\right)^2 \leq 1.0 \text{ and } \sigma_{11} \geq 0 \tag{1}$$

$$F_f^c = \left(\frac{\sigma_{11}}{S_{C1}}\right)^2 \leq 1.0 \ and \ \sigma_{11} < 0 \tag{2}$$

$$F_m^t = \left(\frac{\sigma_{22}}{S_{t2}}\right)^2 + \left(\frac{\sigma_{12}}{S_{S12}}\right)^2 \leq 1.0 \ and \ \sigma_{22} \geq 0 \tag{3}$$

$$F_{m}^{C} = \left(\frac{\sigma_{22}}{S_{S23}}\right)^{2} + [(\frac{S_{C2}}{2S_{S23}}) - 1]\frac{\sigma_{22}}{2S_{S23}} + \left(\frac{\sigma_{12}}{S_{S12}}\right)^{2} \leq 1.0 \; and \; \sigma_{22} < 0 \tag{4}$$

where σ_{11}, σ_{22} and σ_{12}, are the applied stresses, S_{ti} is the tensile strength, S_{ci} is the compressive strength and S_{sij} is the shear strength. The α is a coefficient ($0.0 \leq \alpha \leq 1.0$) that accounts for shear stress σ_{12} contribution to fiber breakage in tension criterion. In this work, the value α =1.0 is used.

Fig. 21 shows the bilinear damage evolution curve based on Hashin damage criterion. The damage occurrs at the elastic limit, curve before elastic limit indicates the elastic stage of the material and curve after elastic limit represents the stiffness degradation process. Parameter d_I represents mode I damage variable and its expression is defined as below:

$$d_{I} = \frac{\varepsilon_{I,eq}^{f}(\varepsilon_{I,eq} - \varepsilon_{I,eq}^{0})}{\varepsilon_{I,eq}(\varepsilon_{I,eq}^{f} - \varepsilon_{I,eq}^{0})} \tag{5}$$

Where $\varepsilon_{I,eq}^{0} \leq \varepsilon_{I,eq} \leq \varepsilon_{I,eq}^{f}$; $I \in (f_{c}, f_{t}, m_{c}, m_{t})$; $\varepsilon_{I,eq}^{0}$ is the equivalent displacement of the damage initiation; $\varepsilon_{I,eq}^{f}$ is the equivalent displacement of the eventual failure of the material (d_I= 1) which can be calculated from Eq. (6).

$$\varepsilon_{I,eq}^{f} = \frac{2G_{IC}}{\sigma_{I,eq}^{0}} \tag{6}$$

Where G_{IC} is the fracture energy or the fracture toughness; $\sigma_{I,eq}^{0}$ is the equivalent stress on the damage initiation moment.

In ABAQUS framework, the Hashin criterion can be implemented in conjunction with a damage evolution law, which is based on the specification of fracture energy G_{IC} values, each corresponding to the material degradation in each mode. Additionally, it should be highlighted that standardized testing methods to obtain fracture energy values associated with the various failure modes that composites can experience are still in development (Tsai, 1965).

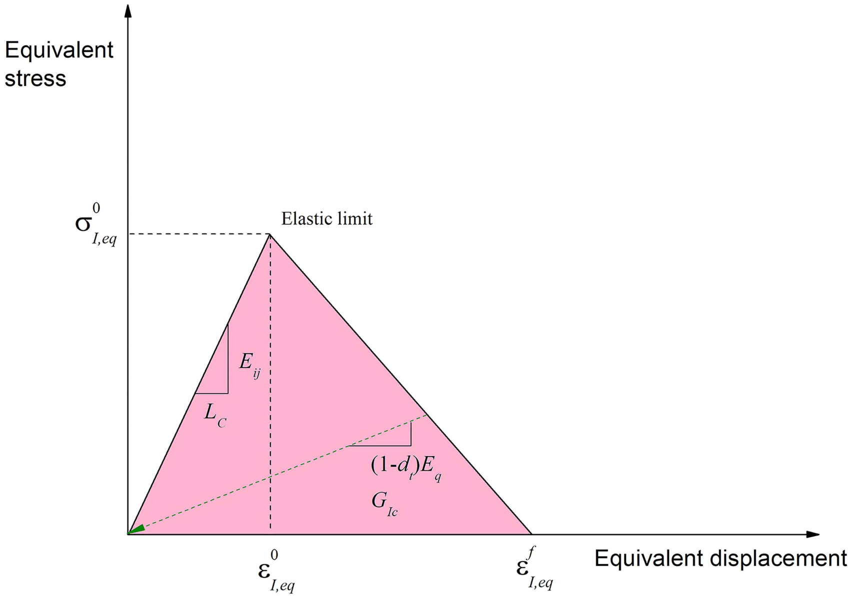

Fig. 21 Bilinear curve of Hashin damage evolution

3.3.4 Interlaminar damage model

Normally, the interlaminar damage evolution process is complex for FRP, the initial delamination and large-area damage process can be considered as the traction behavior of the adjacent laminae. The interlaminar damage initiation can be described using maximum stress/strain criterion and quadratic stress criterion, and the damage evolution process needs to be described using fracture energy (Camanho & Dávila, 2003; Liu, et al., 2018). In this chapter, the quadratic stress criterion was selected to govern the interlaminar failure initiation described in Eq. (7).

$$(\frac{\sigma_s}{S_{\max}})^2 + (\frac{\sigma_t}{T_{\max}})^2 + (\frac{\sigma_n}{N_{\max}})^2 \leq 1 \tag{7}$$

Where σ_s and σ_t are the in-plane nominal traction stresses and σ_n is the normal direction nominal traction stress. $S_{\max}$, $T_{\max}$ and $N_{\max}$ are the corresponding maximum stresses in each direction. The nominal traction stress $\sigma_i(\sigma_s, \sigma_t, \sigma_n)$ can be calculated using Eq. (8).

$$\sigma_i = K_i \varepsilon_i (i = s, t, n) \tag{8}$$

Where ε_i is the cracking distance or sliding strain. When achieving the damage initiation condition, the stiffness degradation occurred according to the parameter d range from 0~1. When d=0, damage initiates and when d=1, total interlaminar failure occurs with the separation of adjacent laminates. The expression of d is demonstrated in Eq. (8).

$$d = \frac{\varepsilon_m^f (\varepsilon_m^{\max} - \varepsilon_m^0)}{\varepsilon_m^{\max} (\varepsilon_m^f - \varepsilon_m^0)} \tag{9}$$

Where: $\varepsilon_m^{\max}$ represents the maximum mixed-mode strain during loading; ε_m is the overall mixed-mode strain including the in-plane and traction strain. The expression of ε_m was demonstrated in Eq. (10); ε_m^f represents the mixed-mode strain at eventual failure and ε_m^0 represents the mixed-mode strain at failure initiation.

$$\varepsilon_m = \sqrt{\varepsilon_n^2 + \varepsilon_s^2 + \varepsilon_t^2} \tag{10}$$

In this model, the Benzeggagh-Kenane (B-K) propagation criterion, Eq. (11), is used to calculate the mixed-mode strain at eventual failure.

$$\varepsilon_m^f = \begin{cases} \dfrac{2}{K\varepsilon_0^m}[G_{IC} + (G_{IIC} - G_{IC})\xi^n] & \varepsilon > 0 \\ \sqrt{(\varepsilon_s^f)^2 + (\varepsilon_t^f)^2} & \varepsilon < 0 \end{cases} \tag{11}$$

Where $\xi = \beta^2/(1+\beta^2)$, when $\xi = 0$. β represents the mixedness ratio ($\beta = \varepsilon_s/\varepsilon_n$). The parameter is the mixed-mode interaction coefficient determined from in-house experiments based on the ASTM D 6671 standard.

Typical bilinear traction-separation relationship is shown in Fig. 22. The delamination phenomenon occurs ($\varepsilon = \varepsilon_{eq}^0$) when the in-plane and normal traction stresses achieving their strength limits with the stiffness degradation according to parameter d simultaneously as shown in Eq. (9). The determined cohesive stiffness and cohesive strength of photo polymerizable resin impregnated glass fabric lamina and thermal polymerizable resin impregnated glass fabric lamina are shown in Table 2.

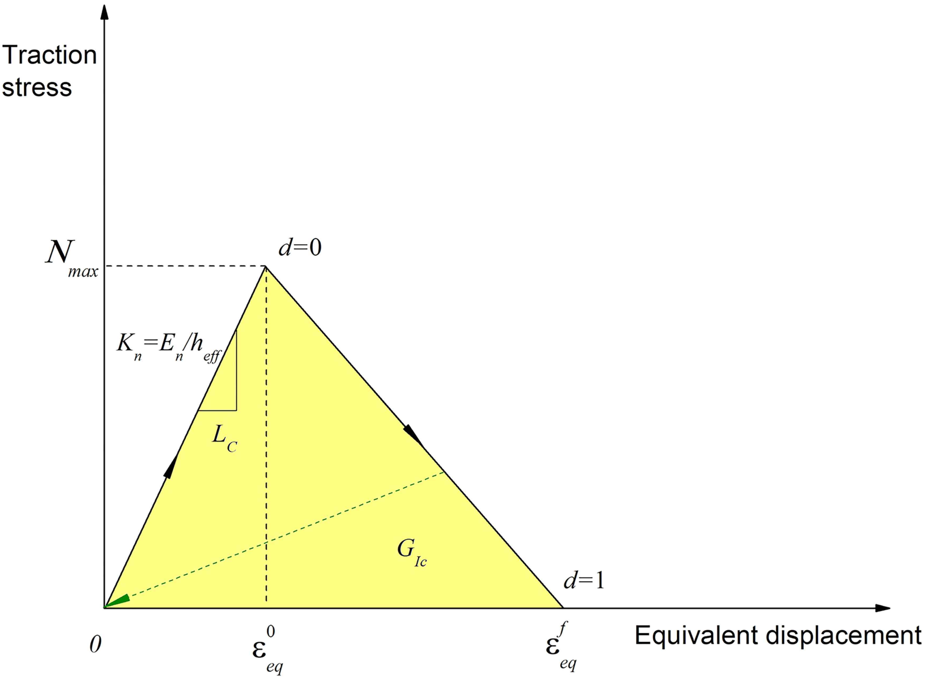

Fig. 22 Bilinear curve of traction-separation relationship

Table 2 Cohesive stiffness and cohesive strength of glass laminae using in numerical work

Materials	Glass lamina (KFR-120V)	Glass lamina (TB 3033B)
Fracture toughness (kJ · m^{-2})	G_{IC}=0.286e3 G_{IIC}=0.858e3	G_{IC}=0.429e3 G_{IIC}=1.289e3
B-K coefficient	1.76	1.98
Nominal cohesive strength (MPa)	s_I=17 s_{II}=29	s_I=20 s_{II}=35

3.3.5 Simulation results of tensile test

The load-displacement curves of UV and RT repaired tensile specimens are shown in Fig. 23, the green, blue and purple circles represent the displacement of 2 mm, 4mm and eventual failure moment and are corresponding to the cohesive damage criterion on the right side, respectively. The simulation results of tensile tests are 251 MPa for UV repaired specimens and 225 MPa for RT repaired specimens. The deviation of ultimate strength compare to experimental results are 2.3% and 8.2% for UV and RT repaired tensile specimens, respectively. For every specified displacement, the distribution of cohesive damage criterion of UV and RT repaired specimens have almost the same tendency, but for RT repaired specimen (red curve), the value of cohesive damage criterion is higher than UV repaired specimen which indicates the more great extent of cohesive damage. The fundamental tensile specimen mainly subjected to the tensile stress and it plays a role of 'master' part of the repaired specimen for bearing the tensile load directly, while the external repair patches mainly dominated to shear and traction stress because they are the 'slave' part of the repaired specimen. The initial cohesive failure occurred on the edges of the repaired part because of submitting the pure shear stress and traction; but for the rest contact parts, the cohesive elements show delayed failure for the mainly shear stress domination. At the eventual failure moment, the edge of repair laminates; cover ply and hole all present cohesive failure in different extent and the RT repaired specimen show severer cohesive damage than UV repaired specimen.

The hashin damage criterion and stress distribution of UV repaired tensile specimens on different displacements corresponding with Fig. 23 are shown in Fig. 24- Fig. 26. The UV repaired specimen shows higher ultimate strength and modulus than RT repaired specimen which has the same tendency of experimental specimen. The stress and hashin fiber tension damage distribution of the top repaired side are more complex than the bottom side which has multiple effects of cohesive behavior, tension behavior and complex geometry. The stress concentration is on the edge of the center hole and repaired laminae. The fibers are observed as the main load-bearing subject. The fiber failure of hashin criterion initiated on the edge of the hole because of the stress concentration. The crack propagation direction is vertical to the tension direction and along the fiber direction.

The eventual failure was observed as a intralamina failure which initiated from the edge of the center hole, together with the delamination phenomenon of repair patches which initiated on the cohesive boundaries. The cohesive elements presented better stress transferability and performed secondary damage initiation which indicates the feasibility and reliability of this repair method for tension behavior.

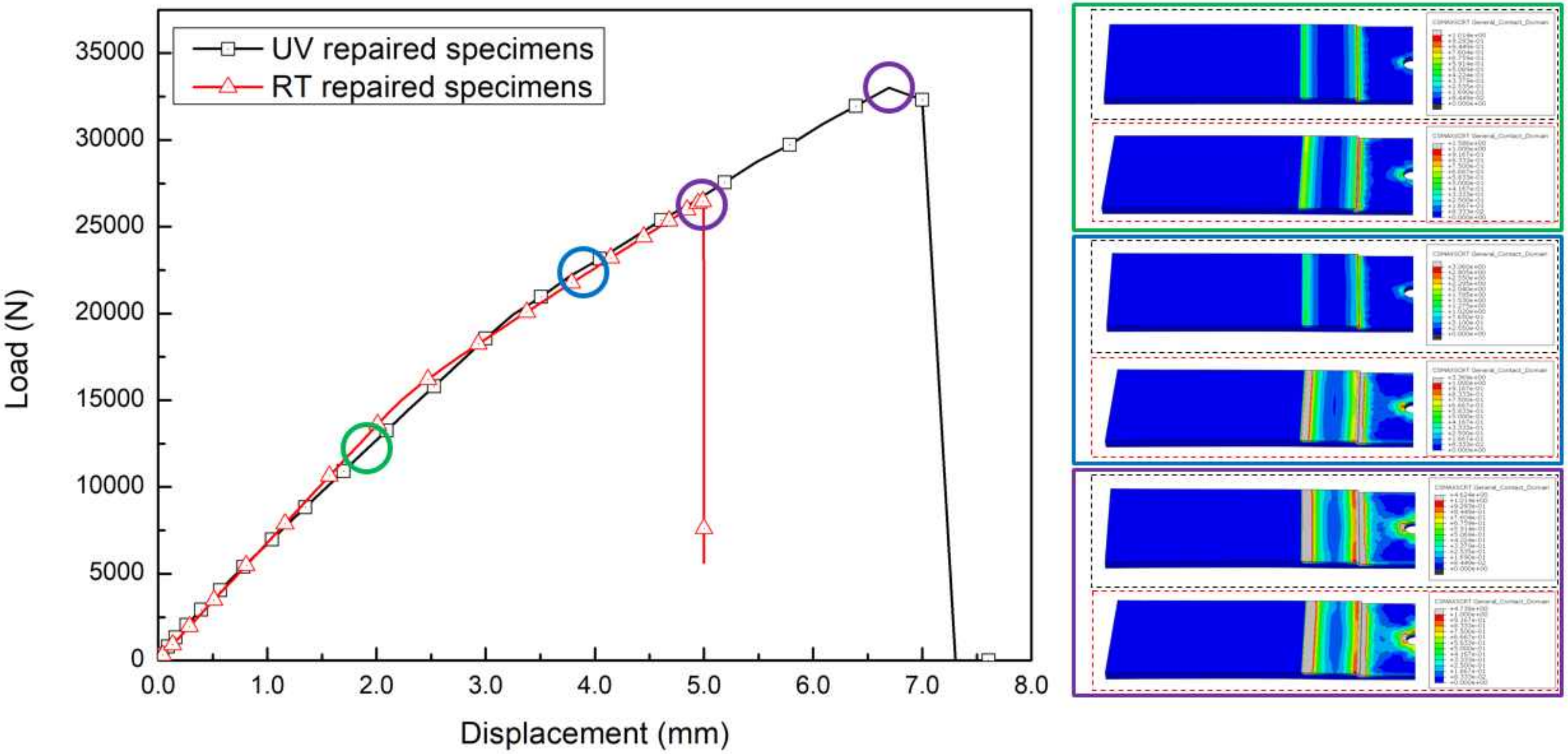

Fig. 23 Load-displacement curves of UV and RT repaired tensile specimens with cohesive damage distribution

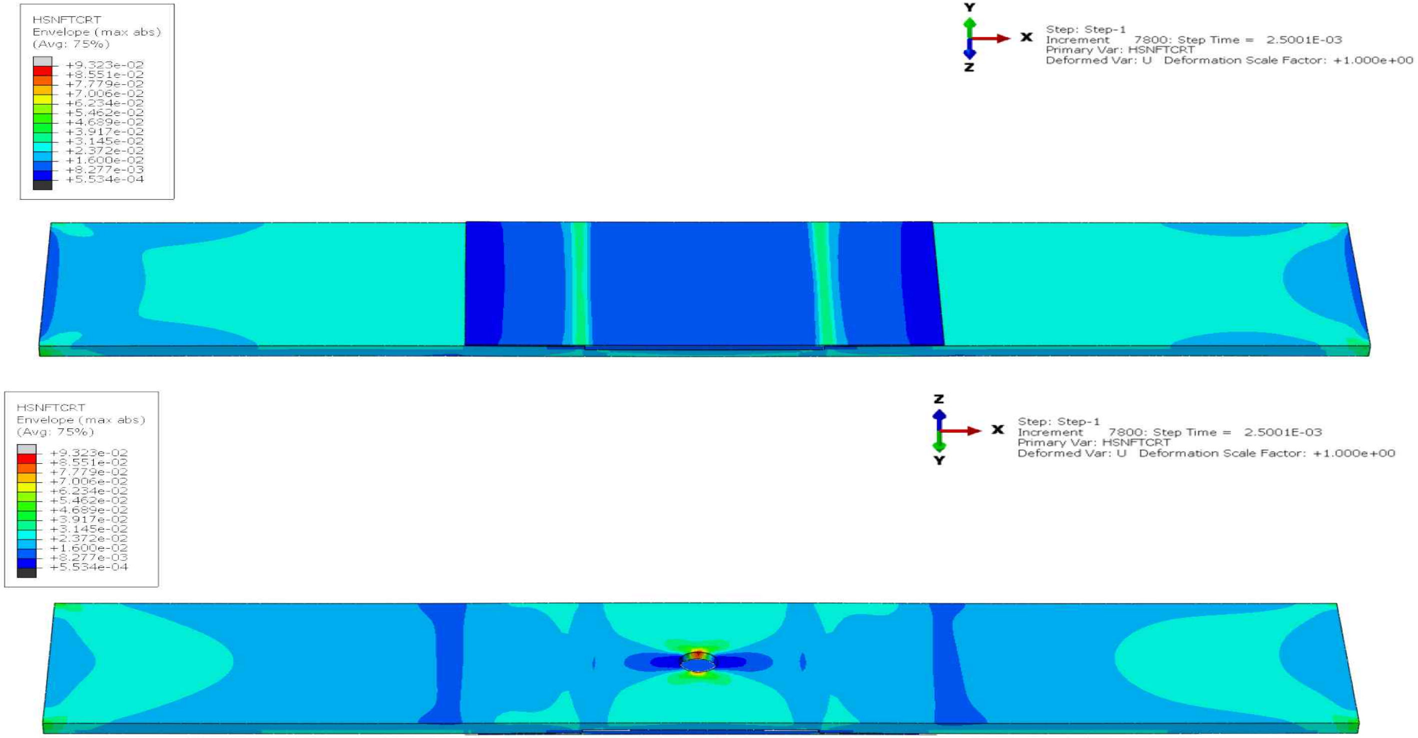
HSNFTCRT
Envelope (max abs)
(Avg: 75%)
+9.323e-02
+8.551e-02
+7.779e-02
+7.006e-02
+6.234e-02
+5.462e-02
+4.689e-02
+3.917e-02
+3.145e-02
+2.372e-02
+1.600e-02
+8.277e-03
+5.534e-04
Y
X
Z
Step: Step-1
Increment 7800: Step Time = 2.5001E-03
Primary Var: HSNFTCRT
Deformed Var: U Deformation Scale Factor: +1.000e+00
HSNFTCRT
Envelope (max abs)
(Avg: 75%)
+9.323e-02
+8.551e-02
+7.779e-02
+7.006e-02
+6.234e-02
+5.462e-02
+4.689e-02
+3.917e-02
+3.145e-02
+2.372e-02
+1.600e-02
+8.277e-03
+5.534e-04
Z
X
Y
Step: Step-1
Increment 7800: Step Time = 2.5001E-03
Primary Var: HSNFTCRT
Deformed Var: U Deformation Scale Factor: +1.000e+00

(a)

-continued-

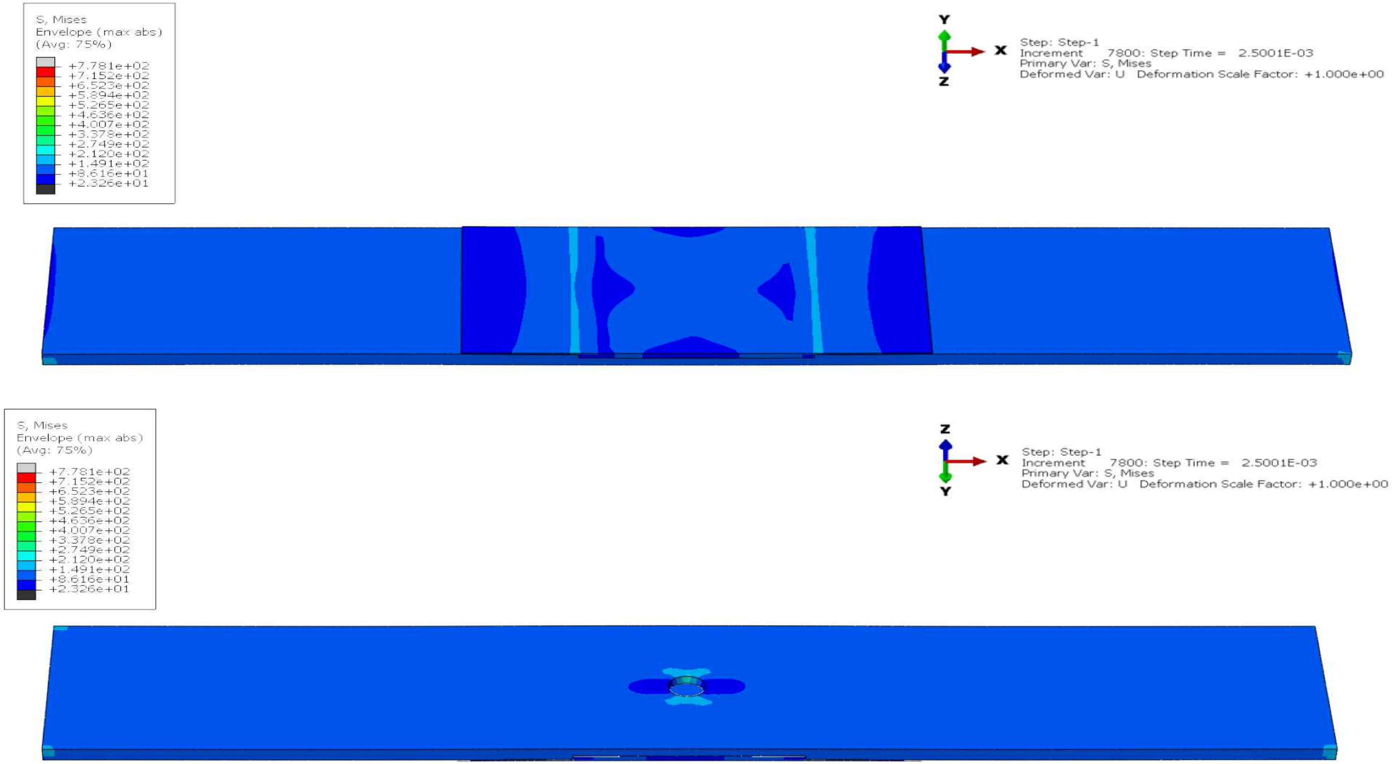

(b)

Fig. 24 Hashin fiber tension damage (a) and stress distribution (b) of UV repaired tensile specimens on displacement of 2.0 mm

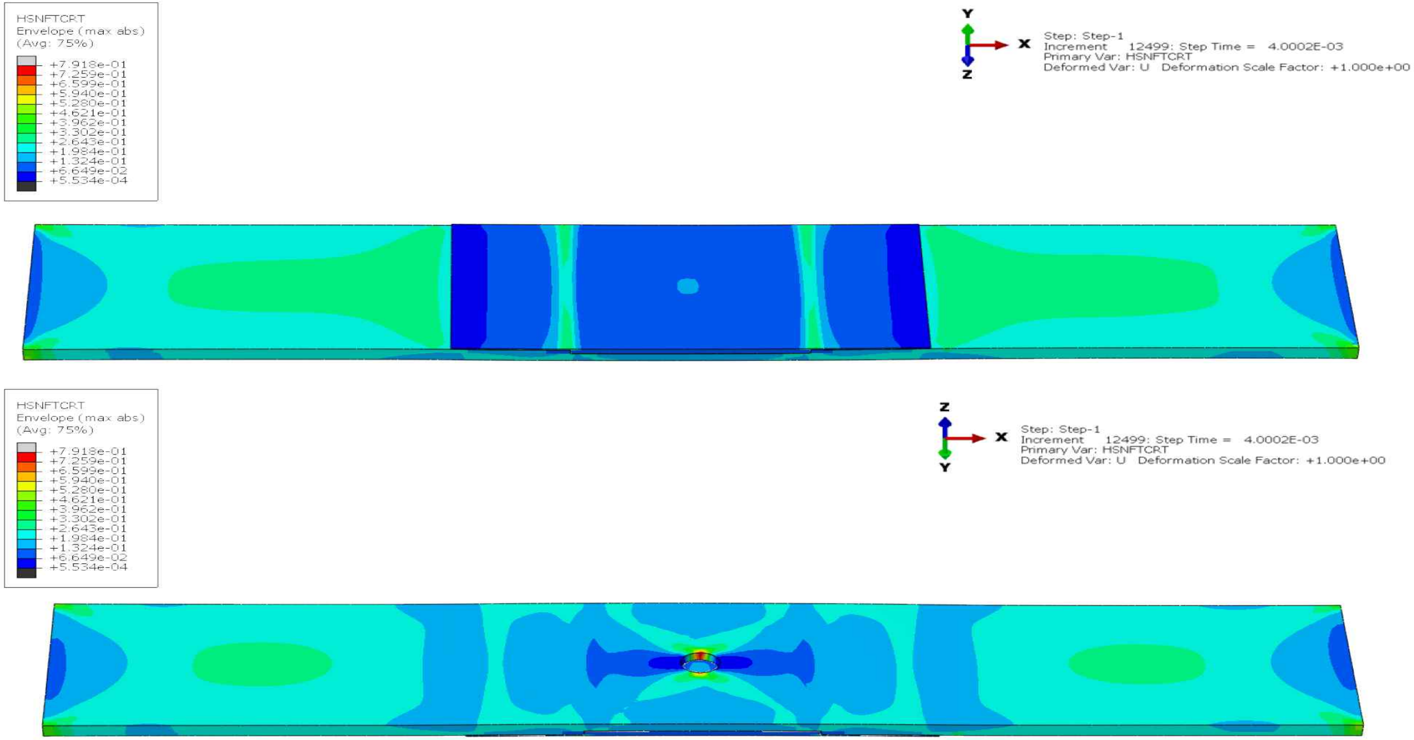
HSNFTCRT
Envelope (max abs)
(Avg: 75%)
+7.918e-01
+7.259e-01
+6.599e-01
+5.940e-01
+5.280e-01
+4.621e-01
+3.962e-01
+3.302e-01
+2.643e-01
+1.984e-01
+1.324e-01
+6.649e-02
+5.534e-04
Y
X
Z
Step: Step-1
Increment 12499: Step Time = 4.0002E-03
Primary Var: HSNFTCRT
Deformed Var: U Deformation Scale Factor: +1.000e+00
HSNFTCRT
Envelope (max abs)
(Avg: 75%)
+7.918e-01
+7.259e-01
+6.599e-01
+5.940e-01
+5.280e-01
+4.621e-01
+3.962e-01
+3.302e-01
+2.643e-01
+1.984e-01
+1.324e-01
+6.649e-02
+5.534e-04
Z
X
Y
Step: Step-1
Increment 12499: Step Time = 4.0002E-03
Primary Var: HSNFTCRT
Deformed Var: U Deformation Scale Factor: +1.000e+00

(a)

-continued-

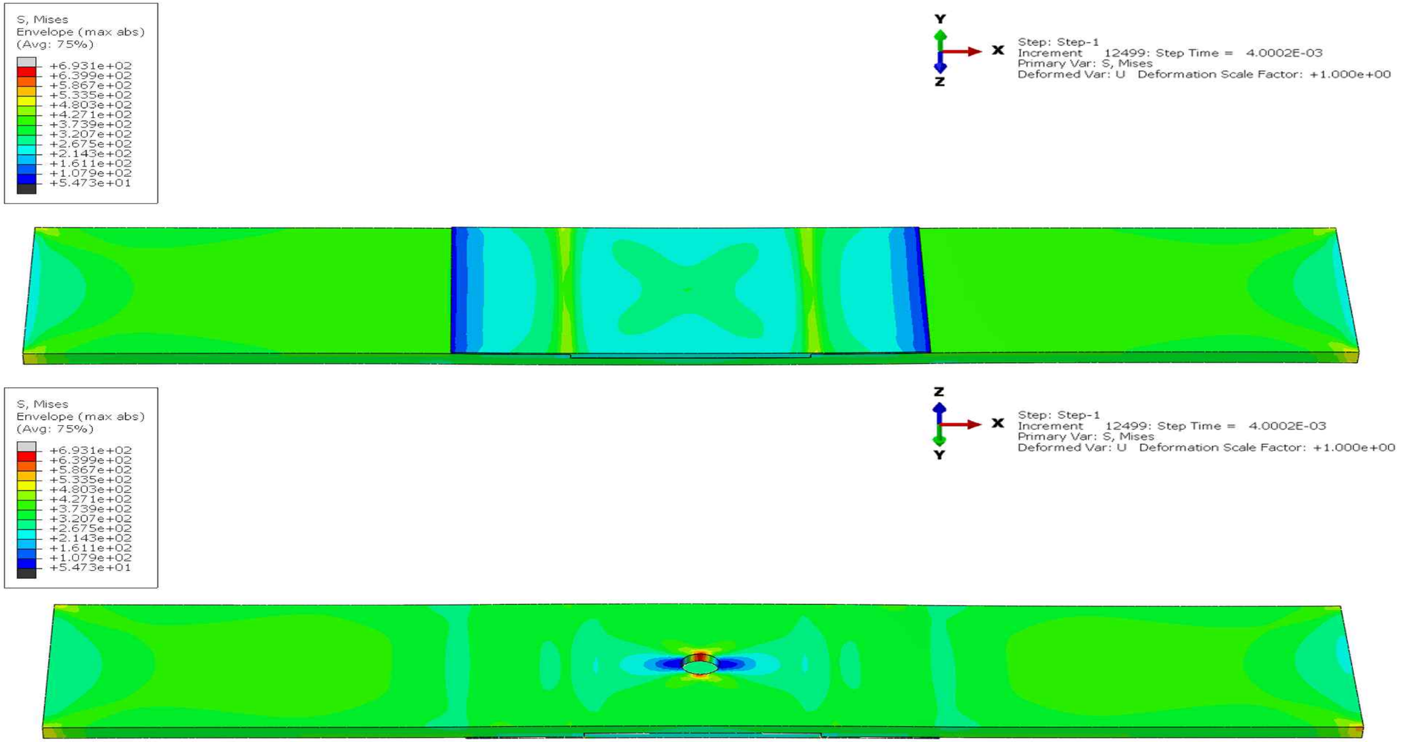

(b)

Fig. 25 Hashin fiber tension damage (a) and stress distribution (b) of UV repaired tensile specimens on displacement of 4.0 mm

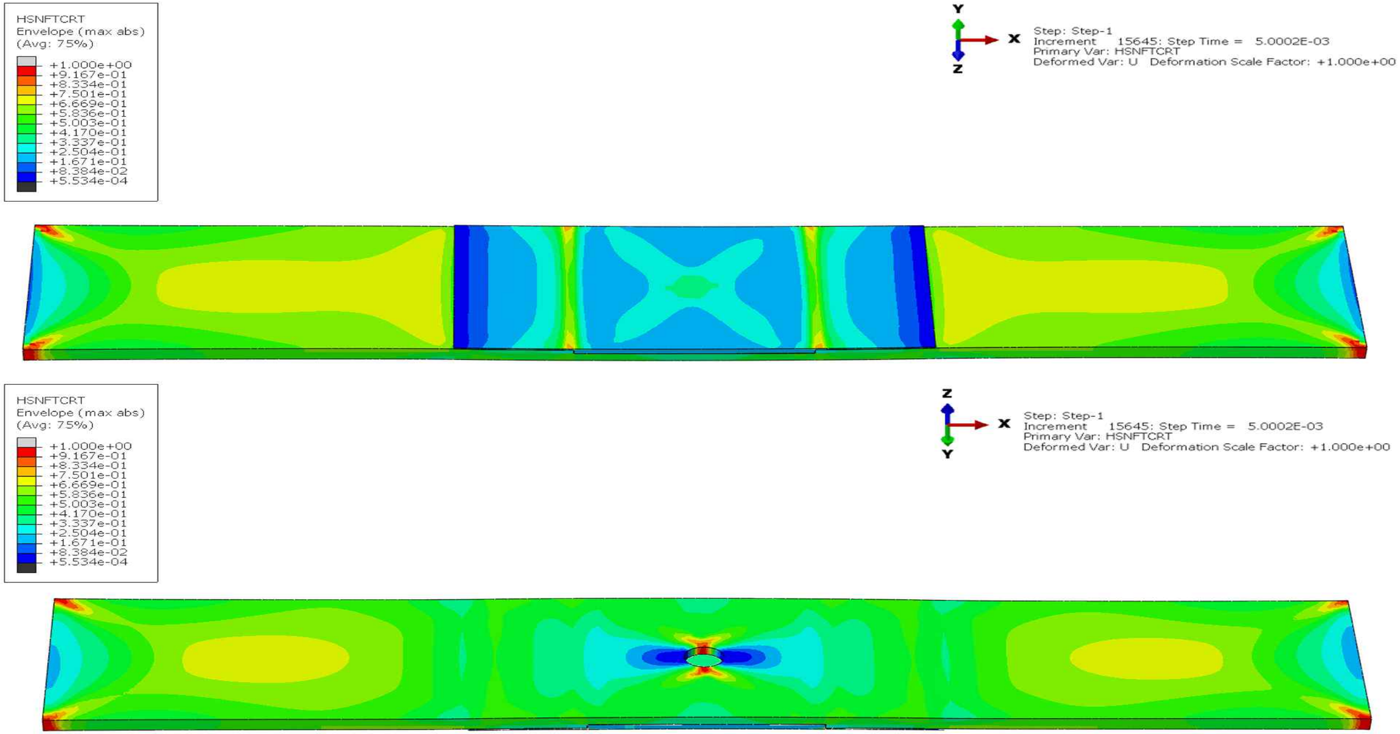
HSNFTCRT
Envelope (max abs)
(Avg: 75%)
+1.000e+00
+9.167e-01
+8.334e-01
+7.501e-01
+6.669e-01
+5.836e-01
+5.003e-01
+4.170e-01
+3.337e-01
+2.504e-01
+1.671e-01
+8.384e-02
+5.534e-04
Y
X
Z
Step: Step-1
Increment 15645: Step Time = 5.0002E-03
Primary Var: HSNFTCRT
Deformed Var: U Deformation Scale Factor: +1.000e+00
HSNFTCRT
Envelope (max abs)
(Avg: 75%)
+1.000e+00
+9.167e-01
+8.334e-01
+7.501e-01
+6.669e-01
+5.836e-01
+5.003e-01
+4.170e-01
+3.337e-01
+2.504e-01
+1.671e-01
+8.384e-02
+5.534e-04
Z
X
Y
Step: Step-1
Increment 15645: Step Time = 5.0002E-03
Primary Var: HSNFTCRT
Deformed Var: U Deformation Scale Factor: +1.000e+00

(a)

-continued-

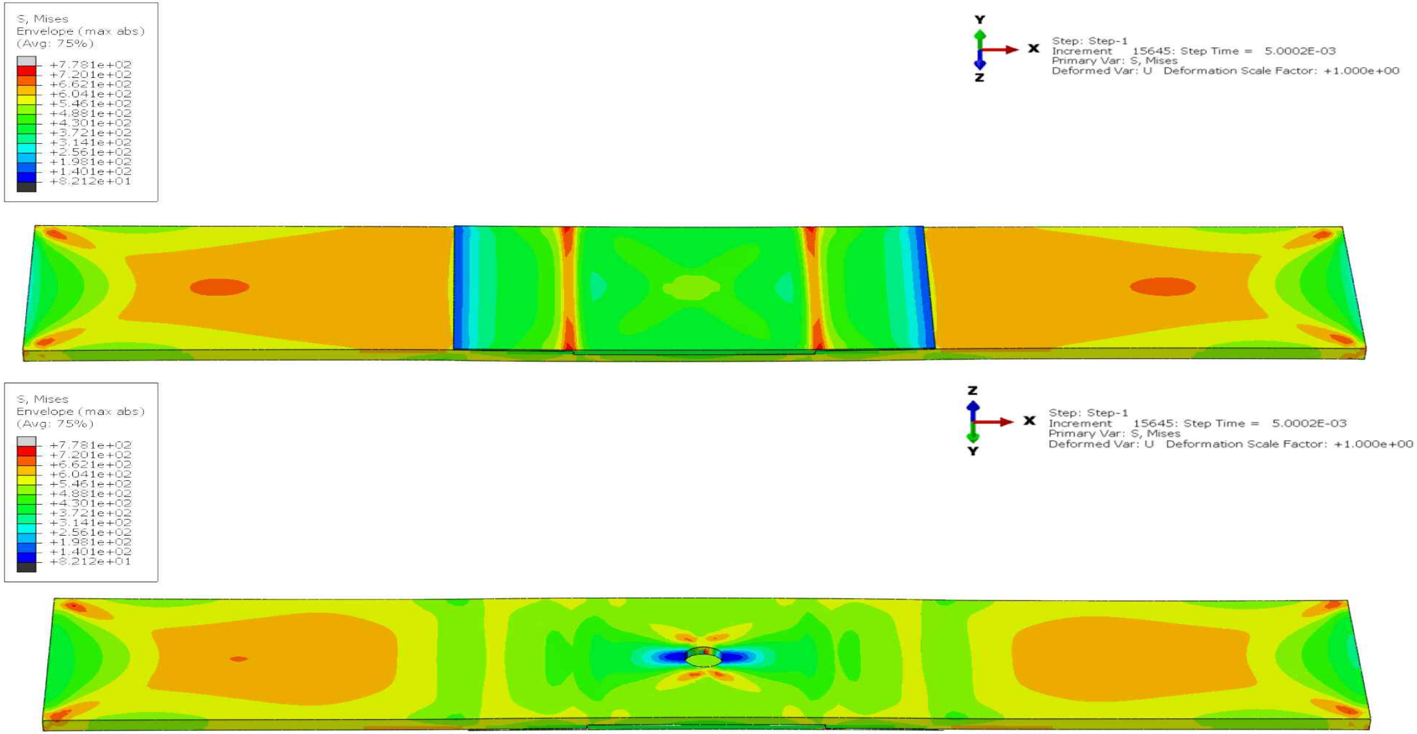

(b)

Fig. 26 Hashin fiber tension damage (a) and stress distribution (b) of UV repaired tensile specimens on eventual failure

3.3.6 Simulation results of bending test

The load-displacement curves of UV and RT repaired bending specimens are shown in Fig. 27, the green, blue and purple circles represent the displacement of 1 mm, 2 mm and eventual failure moment and corresponding to the cohesive damage criterion on the right side, respectively. The simulation results of bending tests are 287 MPa for RT repaired specimens and 388 MPa for UV repaired specimens. The deviation of ultimate strength compare with experimental results are 2% and 5.9% for UV and RT repaired bending specimens, respectively. The distribution of cohesive damage of bending specimen is on the long edge of the contact surfaces and the positions beside the top loading indenter. The stress distribution of UV and RT repaired bending specimens are almost the same at load beginning stage but differed later. For the UV repaired specimens (black line), the eventual crack initiates and propagates without the cohesive surface delamination but for RT repaired specimen (red line) the cohesive surface presents failure area during the load imposing procedure which demonstrate the excellent adhesion of photo polymerizable resin and the feasibility and reliability of this repair method for compression behavior.

The hashin damage criterion and stress distribution of UV repaired bending specimens on different displacements are shown in Fig. 28 - Fig. 30. For bending specimens, the tension and compressive of hashin damage criterion were both set as an output option. The bottom laminae of specimen suffered tension stress, and the top laminae of specimen suffered compressive stress. Moreover, the stress distribution was simpler than tensile test because of the uniform geometry of bending specimens. The stress concentration position is the most curved area which caused by top loading indenter. The failure of fiber tension and fiber compression occurred almost the same moment. The crack caused by tension failure initiated on the bottom laminae and penetrated through the thickness direction which is reasonable to be thought as the critical crack leading to eventual failure.

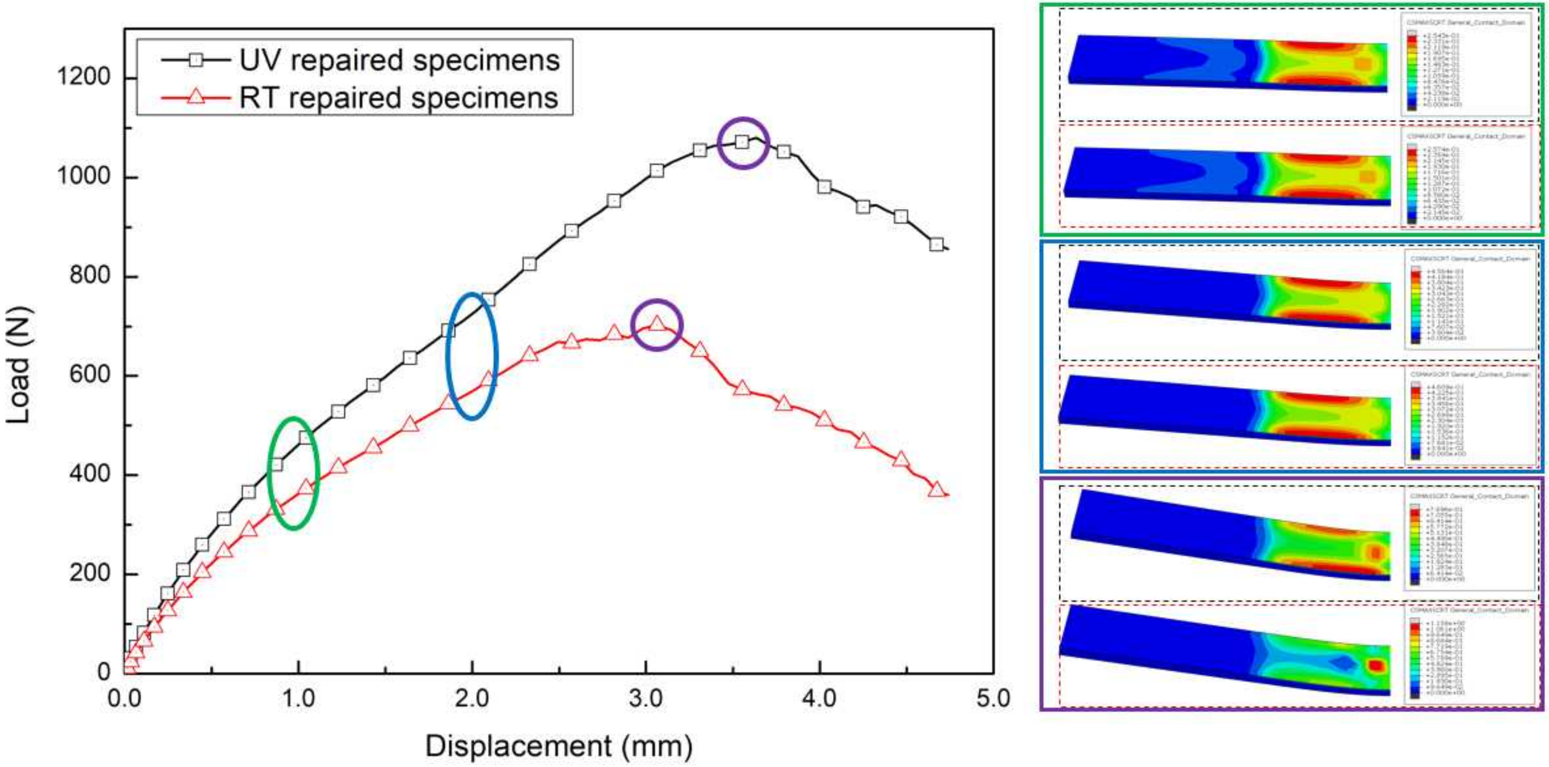

Fig. 27 Load-displacement curves of UV and RT repaired bending specimens with cohesive damage distribution

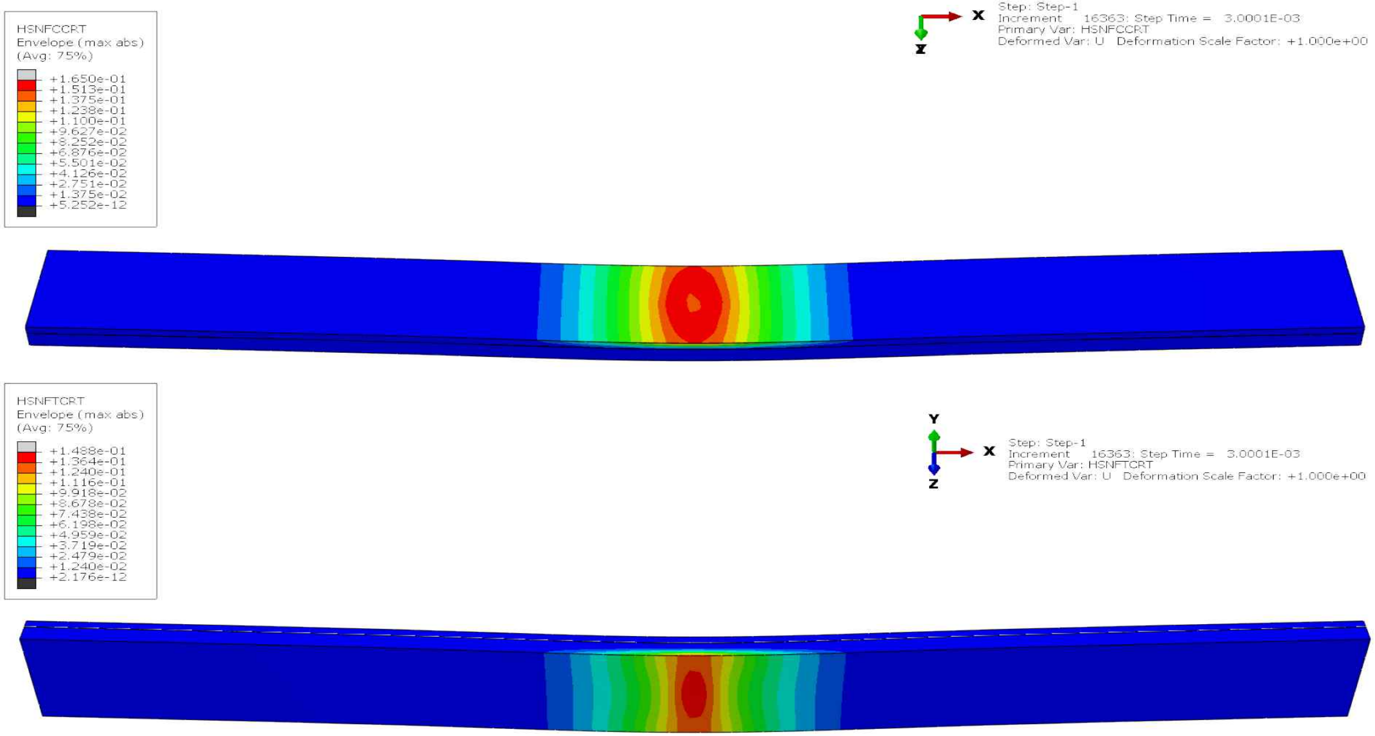
HSNFCCRT
Envelope (max abs)
(Avg: 75%)
+1.650e-01
+1.513e-01
+1.375e-01
+1.238e-01
+1.100e-01
+9.627e-02
+8.252e-02
+6.876e-02
+5.501e-02
+4.126e-02
+2.751e-02
+1.375e-02
+5.252e-12
X
Z
Step: Step-1
Increment 16363: Step Time = 3.0001E-03
Primary Var: HSNFCCRT
Deformed Var: U Deformation Scale Factor: +1.000e+00
HSNFTCRT
Envelope (max abs)
(Avg: 75%)
+1.488e-01
+1.364e-01
+1.240e-01
+1.116e-01
+9.918e-02
+8.678e-02
+7.438e-02
+6.198e-02
+4.959e-02
+3.719e-02
+2.479e-02
+1.240e-02
+2.176e-12
Y
X
Z
Step: Step-1
Increment 16363: Step Time = 3.0001E-03
Primary Var: HSNFTCRT
Deformed Var: U Deformation Scale Factor: +1.000e+00

(a)

-continued-

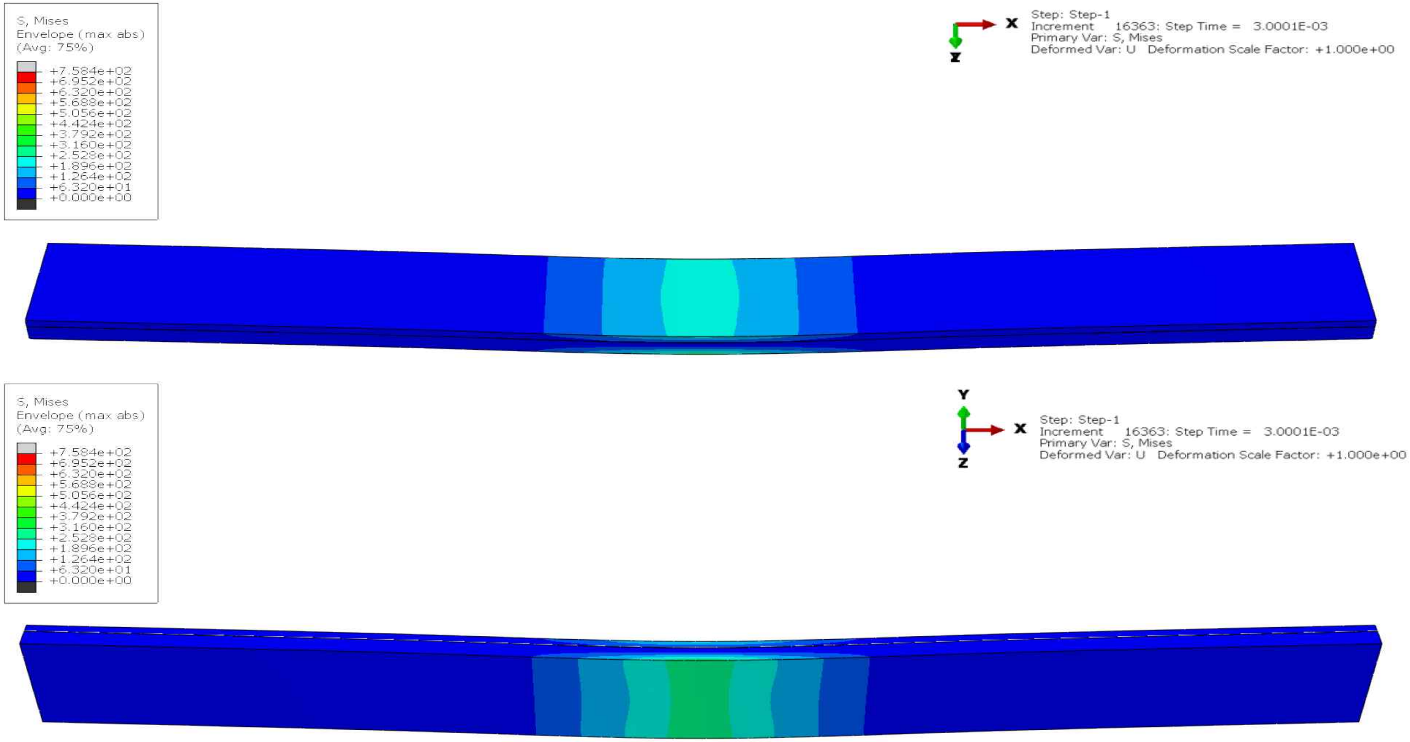

(b)

Fig. 28 Hashin fiber damage (a) and stress distribution (b) of UV repaired bending specimens on displacement of 2.0 mm

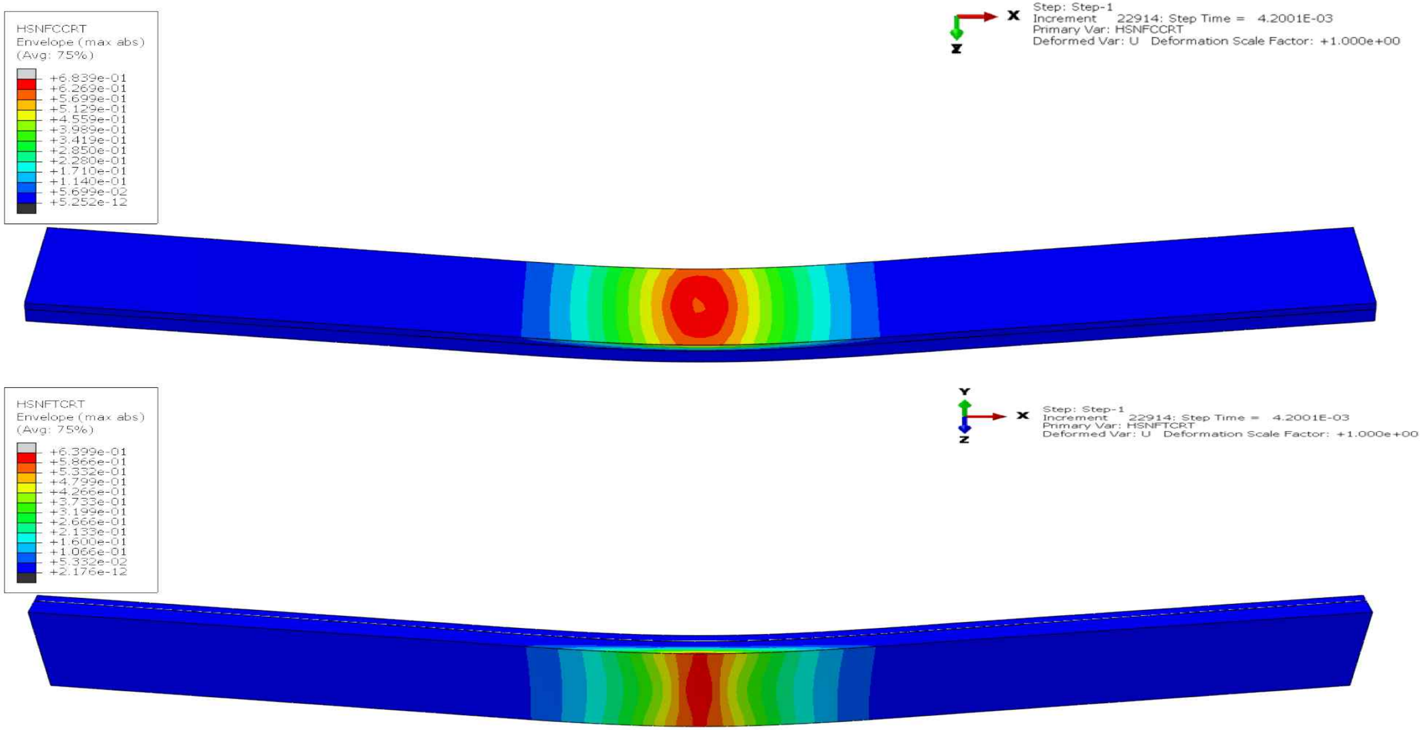
HSNFCCRT
Envelope (max abs)
(Avg: 75%)
+6.839e-01
+6.269e-01
+5.699e-01
+5.129e-01
+4.559e-01
+3.989e-01
+3.419e-01
+2.850e-01
+2.280e-01
+1.710e-01
+1.140e-01
+5.699e-02
+5.252e-12
X
Z
Step: Step-1
Increment 22914: Step Time = 4.2001E-03
Primary Var: HSNFCCRT
Deformed Var: U Deformation Scale Factor: +1.000e+00
HSNFTCRT
Envelope (max abs)
(Avg: 75%)
+6.399e-01
+5.866e-01
+5.332e-01
+4.799e-01
+4.266e-01
+3.733e-01
+3.199e-01
+2.666e-01
+2.133e-01
+1.600e-01
+1.066e-01
+5.332e-02
+2.176e-12
Y
X
Z
Step: Step-1
Increment 22914: Step Time = 4.2001E-03
Primary Var: HSNFTCRT
Deformed Var: U Deformation Scale Factor: +1.000e+00

(a)

-continued-

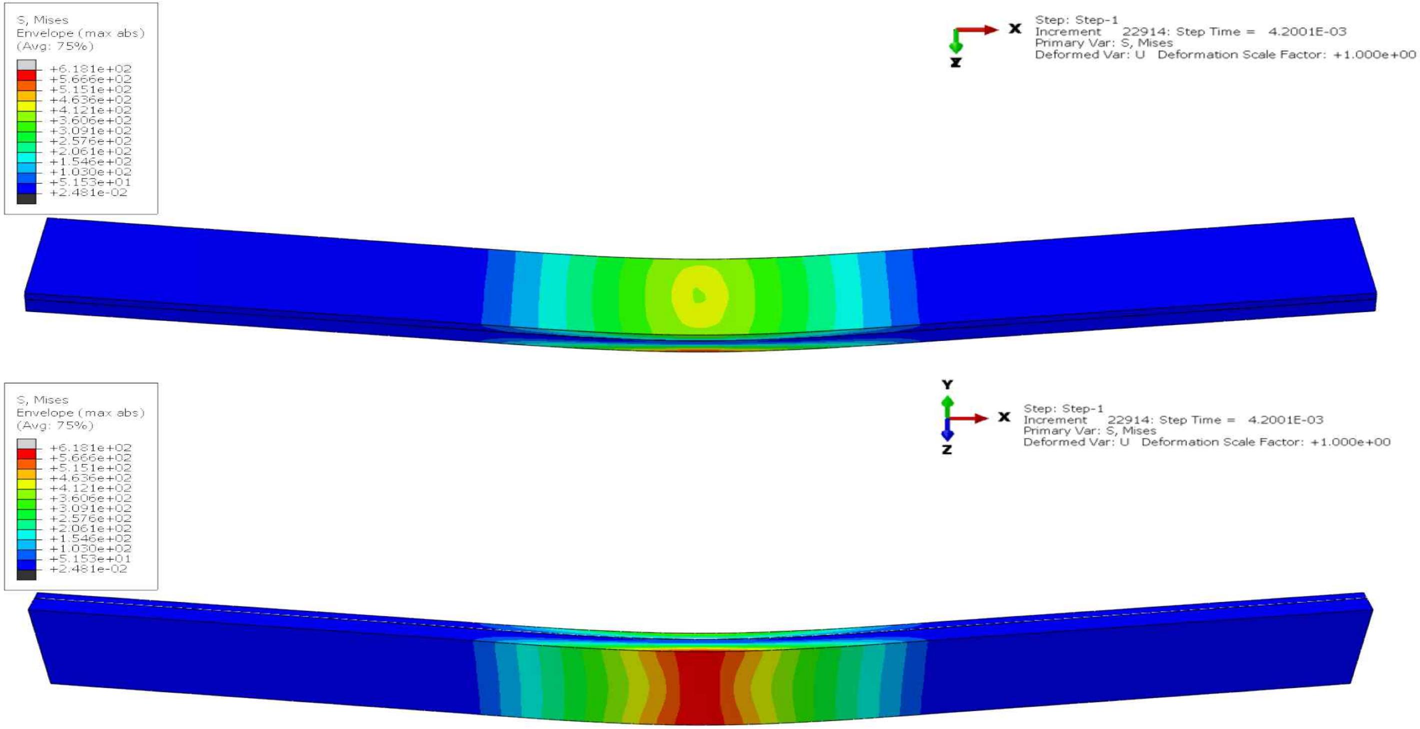

(b)

Fig. 29 Hashin fiber damage (a) and stress distribution (b) of UV repaired bending specimens on displacement of 4.0 mm

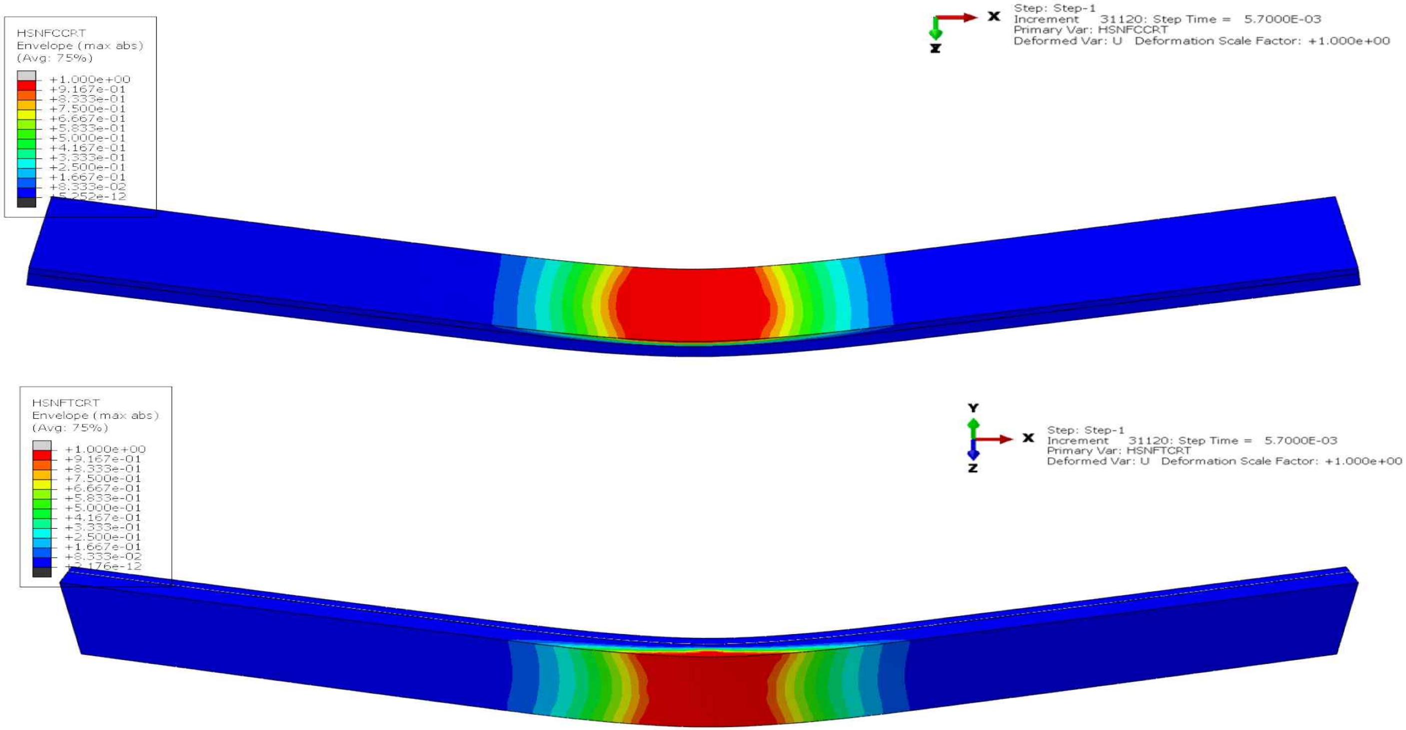
HSNFCCRT
Envelope (max abs)
(Avg: 75%)
+1.000e+00
+9.167e-01
+8.333e-01
+7.500e-01
+6.667e-01
+5.833e-01
+5.000e-01
+4.167e-01
+3.333e-01
+2.500e-01
+1.667e-01
+8.333e-02
+5.252e-12
X
Z
Step: Step-1
Increment 31120: Step Time = 5.7000E-03
Primary Var: HSNFCCRT
Deformed Var: U Deformation Scale Factor: +1.000e+00
HSNFTCRT
Envelope (max abs)
(Avg: 75%)
+1.000e+00
+9.167e-01
+8.333e-01
+7.500e-01
+6.667e-01
+5.833e-01
+5.000e-01
+4.167e-01
+3.333e-01
+2.500e-01
+1.667e-01
+8.333e-02
+2.176e-12
Y
X
Z
Step: Step-1
Increment 31120: Step Time = 5.7000E-03
Primary Var: HSNFTCRT
Deformed Var: U Deformation Scale Factor: +1.000e+00

(a)

-continued-

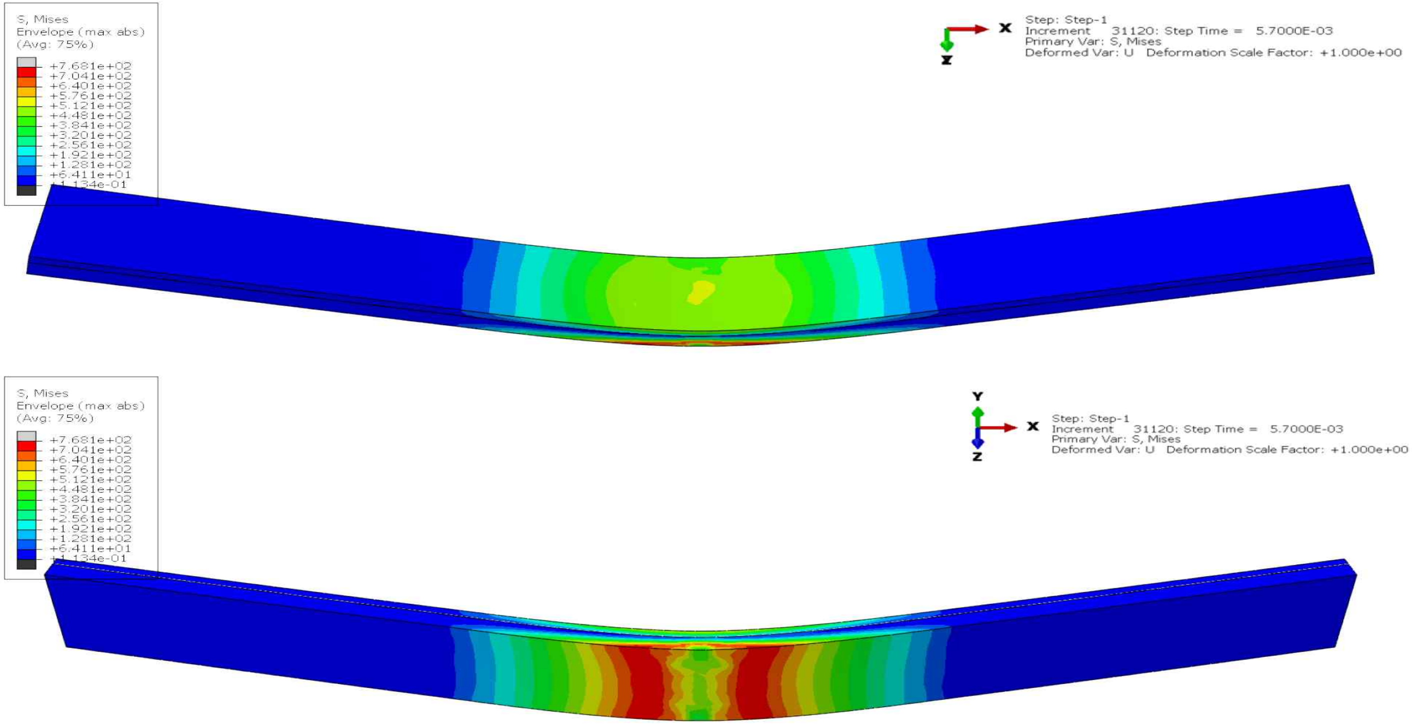

(b)

Fig. 30 Hashin fiber damage (a) and stress distribution (b) of UV repaired bending specimens on eventual failure

3.4 Conclusions

In this study, patch remediation was conducted to GFRP specimens by utilizing photo and thermal polymerizable resins. Experimental and numerical works were implemented to investigate the tensile and bending behavior of repaired specimens. During the numerical work performed by ABAQUS, hashin damage criterion was used to initiate and propagate the intralaminar failure of laminae, while quadratic stress criterion and B-K criterion were used to simulate the interlaminar failure. Additional DCB and ENF tests were conducted to determine the cohesive fracture toughness parameters. Base on the results, the following preliminary conclusions are obtained:

(1) The ultimate strength of tensile and bending tests are 257 and 396 MPa for UV repaired specimens, 245 and 304 MPa for RT repaired specimens, respectively. The numerical and experimental results show the similarity in both values and tendencies. Moreover, UV repaired specimens showed smaller deviation than RT repaired specimens according to experimental result. The load-displacement curves of experimental and numerical data also showed a good agreement which validated the reliability of the simulation results.

(2) For the tensile specimens, the initial cohesive failure occurred on the edges of the repaired part. RT repaired specimens show severer cohesive damage compare to that of UV repaired specimens. The fiber damage initiated at the edge of the center hole and propagated along fiber orientation. The eventual failure is observed as fiber/matrix failure together with the delamination phenomenon on repaired laminae of UV repaired specimen, which indicates the better stress transferability of the cohesive layer.

(3) For the bending specimens, the distribution of cohesive damage criterion of bending specimen is on the longitude edge of the contact surfaces. The eventual crack initiated and propagated without the cohesive element

delamination for UV repaired specimens. For RT repaired specimen, the delamination phenomenon occurred, which reveals the excellent adhesion of photo polymerizable resin and the feasibility and reliability of this repair method for compression behavior.

(4) The UV repaired specimens show better tensile and bending properties than RT repaired specimens according to the experimental and numerical data. Patch remediation method utilizing photo polymerizable resin also has features of rapid and effective processing. Furthermore, this repair method is considered to be especially suitable for harsh and complex working environments.

4. Effect of Low Temperature Environment on UV repaired GFRP

The objectives of this chapter are to investigate a novel remediation methodology for GFRP manufactured wind turbine blades for improving their properties under low temperature environments. The fundamental specimens that were fabricated using wet prepreg manufacture technic were pre-damage followed by attachment of external glass fiber patches as the repair part. The repair patches were impregnated by thermal or photo polymerizable resin, followed by ambient, 80℃ curing or ultraviolet irradiation curing, respectively. Tensile, flexure, short beam shear tests and end notch flexure tests were conducted both in the room and low temperature environments according to ASTM standards. The UV repaired specimens reveal better properties than RT repaired specimens both in low and room temperature environments. The higher external-fundamental laminate interfacial bonding strength and lower velocity of crack diffusion, as well as the initiation of residual thermal stress, which resulted in better mechanical properties under low temperature environment. Besides, the outstanding performance of photo polymerizable resin is considered as the high crystallinity content curing by ultraviolet irradiation and the great inherent strength of itself.

4.1 Introduction

With a growing number of glass fiber reinforced composites wind turbines now in service, their maintenance is becoming an urgent issue. In China, most wind farms are developing towards plateaus with low temperature environment and while in service (Liu, et al., 2019), wind turbine blades experience various modes of loading (Huang, et al., 2018; Sanaa, et al., 2018; Shigeru, 2013). The investigation of a new method in the remediation of GFRP wind turbine blades to realize quickly and cost-effectively repair under the specified environment and loading is necessary.

UV-irradiation polymerization is a powerful method to achieve a rapid and effective attachment of repair patches through highly cross-linked polymers and has been used before in GFRP patches for composites (Zidani, et al., 2015; Sangermano, et al., 2018; Murray, et al,, 2019). The resins can release rapid in-situ remediation without a heat source, which especially suitable for the working environments of wind turbine blades. Also, it doesn't require high altitude disassembly and transportation; thus that can improve the efficiency of repair and reduce losses.

It is evident that environmental conditions must also affect the mechanical performance of the composites. The adverse effects of high temperatures have been demonstrated in the past, but little efforts (Mohammadreza & Ali, 2016; Cormier, et al., 2016) were devoted to identifying effects of exposure in low temperatures which most the wind turbine blades actual suffered.

In this chapter, laminated specimens were repaired by the ambient environment cured, and heat activated cured with thermal polymerizable resin and UV cured with photo polymerizable resin, respectively. In consideration of the environment in which wind turbines located, the mechanical properties including tensile and bending strength under low temperature were tested. The short beam shear test and end notch flexure tests were conducted for investing the internal defect initiation and propagation behavior. The microscopic morphology of the fracture surface was then observed by a scanning electron microscope (SEM) for exploring the interlaminar property and crack propagation.

4.2 Experimental works

The fundamental specimens prepared for repairing were fabricated using wet prepreg manufacture technic. During the processing, 20 layers laminate of glass fiber woven plains with a dimension of 300 mm × 500 mm were used as the reinforcement; while epoxy resin (KFR-120V) and hardener (KFR-141) were selected as the matrix. A piece Teflon was inserted into the middle laminates to form the pre-crack. All laminates were penetrated resin adequately by hand lay-up, then a piece of peel ply and vacuum bag were covered upon. The vacuum phenomenon was conducted after the vacuum bag was well sealed by the vacuum pump. Wet prepreg set-ups were stored in the oven for curing at 80℃ and settle for 12 hours with a uniformed heating and cooling time of 30 minutes. After demolding, the fundamental samples were cut into specimens.

Considering the repair effectiveness are impacted by increasing the load transfer between the parent material and the patch or by reducing the risk of the adhesive debonding, three parameters which were fiber surface treatment, surface roughness and using of cover layer were introduced (Andrew & Israel, 2006). Glass fiber laminate patches were processed surface treatment in 5 wt% NaOH solution bath heating for 3 hours, then rinsed by distilled water sufficiently and dried by hot plate for removing the contamination. In repair procedure, every specimen was ground by sanding machine (model 3037 supplied by Astro Pneumatic Co.) on the aimed area to increase the surface roughness and slightly reduce the thickness. Specimen surfaces were rinsed by acetone then dried at room temperature for removing the grinding residues. Four GF laminae were attached on the ground surface after penetrated by thermal or photo polymerizable resin (TB 3033B), an extra piece of an over-sized cover layer was then attached upon. Curing was conducted under the ambient or heated environment with thermal polymerizable resin or UV environment with photo polymerizable resin. The UV curing was realized by irradiation under 365 nm wavelength ultraviolet for 10 minutes by UV lamp (UV CURE-60PH supplied by LICHTZEN Co.) according to ASTM G 154.

The end notch flexure test was conducted by meaning simple three-point flexure experiments on specimens with a fixed initial delamination length refer to ASTM D 7905. The initial delamination length was 50 mm with span length 80 mm. During the process specimens were loaded and unloaded in the elastic range first to obtain compliance C with respect to initial delamination lengths of a=15 mm, 25 mm and 35 mm with a constant cross speed=0.5 mm/min. The delamination length was adjusted by keeping the supports fixed and sliding the specimen. Tensile, bending and short beam shear (SBS) tests were performed under both low and ambient environment according to ASTM D 3039, D 790, and D 2344, respectively.

4.3 Results and discussion

4.3.1 Tensile and bending strength

Fig. 31 shows the result of the tensile and flexure tests of repaired GFRP specimens. Like previous studies, the tensile specimens made by wet prepreg manufacture technique were pre-damaged with a hole in the center then repaired with glass fiber using different resins. From the result of tensile and flexure tests, as shown in Fig. 31, UV repaired specimens have higher strength both under room and low temperature test environment. Meanwhile, the strength tested at low temperature is higher than the ambient temperature. The tensile strength had a maximum value of 191 MPa and bending strength had a maximum value of 420 MPa. The Load-displacement curves of tensile and flexure tests are shown in Fig. 32 and Fig. 33. During the tensile test, smooth and steady load-displacement curves were obtained in all situations. The stiffness of specimens can be analyzed because the slope of the curves was consistent which had a small increase in low temperature. The elongation at break and the maximum stress values under low temperature test are higher than in room temperature. The similitude elastic modulus values were due to the fundamental specimen dominant volume fraction. The distinctions of ultimate strength and different elongations at break are caused by the strengthened external-fundamental laminate interfacial bonding strength and fracture toughness of specimens at different curing and test conditions. The strengthened phenomenon in UV repaired specimens can be validated by the macroscopic fracture morphologies which convert the failure pattern from adhesive debonding and delamination into integral breakage at the drilled position.

The Load-displacement curves of flexure test in Fig. 33 show rough and unstable failure processing. The flexure modulus of UV repaired specimens was higher than room temperature and 80℃ repaired specimens both in an ambient and low temperature test environments. The elongation at break in a low temperature environment have an enlarged value about 1 mm. Under the low temperature test situation, the specimens present the multi-stage plateau phenomenon which indicate the impediment of crack propagation leading to a delayed failure and higher ultimate strength. During the bending test, because of the contact of the repair laminates and the indenter, the properties of repair laminate itself become essential. The strong nature of photo polymerizable resin contribute to the higher ultimate strength and the impedance of crack propagation occurred in low test environment. The longer elongation revealed a strengthened interfacial bonding strength between external and fundamental laminates.

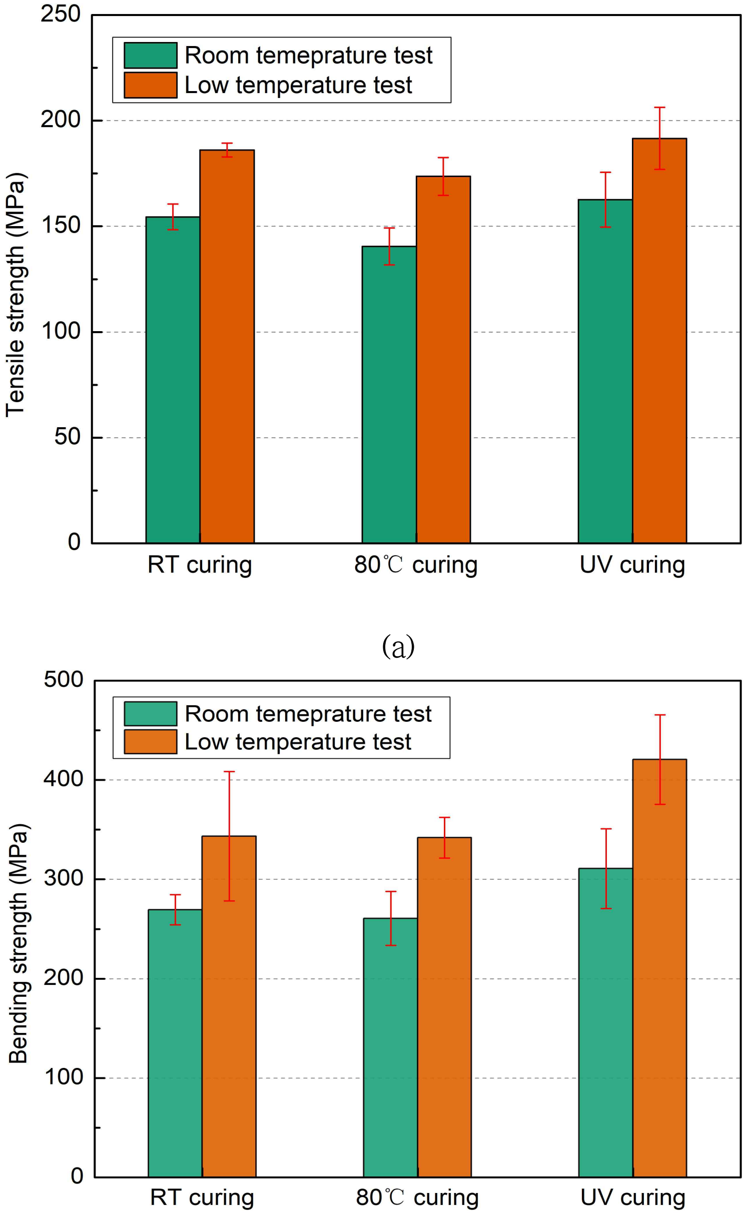

(a)

(b)

Fig. 31. Tensile (a) and bending (b) strength of different curing and test conditions

The little variation of modulus of tensile and bending test between the room and low temperature environment can be explained by the effect of residual thermal stress. Residual thermal stress which induces more stress on the bonded components as the temperature dropping, makes the polymeric matrix become more brittle, stiffer and stronger and causes the increase of modulus. The influence of residual thermal stress can be explained as below (Hartwig & Knaak, 1984; Abdulmohsen, et al., 2018):

$$S_f = S_{UTM} - S_{TR} \tag{1}$$

Where S_f is the effective free stress or strain, S_{UTM} is the presented value from universal test machine, S_{TR} is the residual thermal tensile stress or strain. In combination with low contraction of the fibers in low temperature environment, more and more residual thermal tensile stress or strain is accumulated on the matrix. This reduces the effective free stress or strain available for external loading. But in turns of the exiguity change of modulus, the effect of thermal residue stress is not considered as the main factor for ultimate strength and elongation.

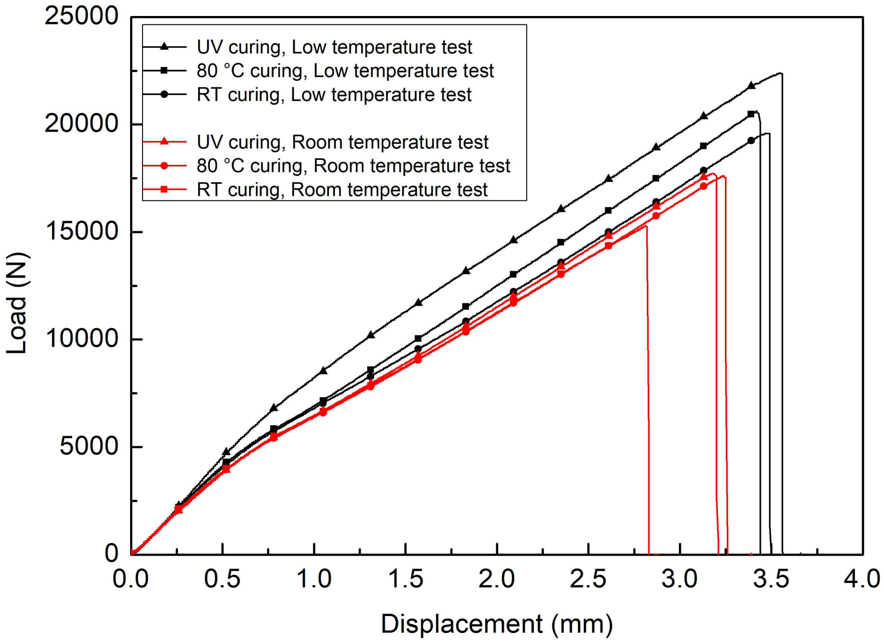

Fig. 32 Load-displacement curves of tensile test of different curing and test conditions

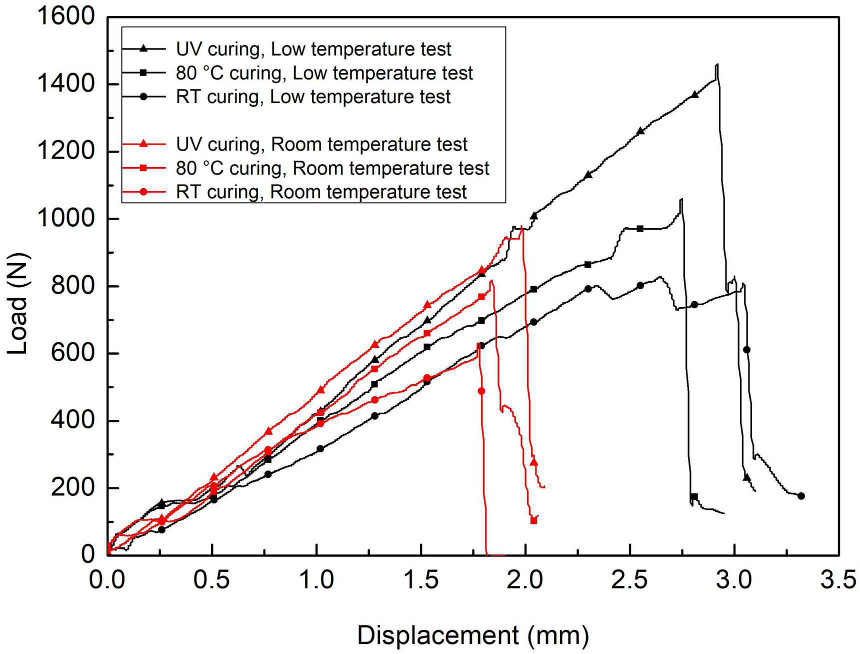

Fig. 33. Load-displacement curves of bending test of different curing and test conditions

4.3.2 Mold II fracture toughness

The value of mode II facture toughness (G_{IIC}) was determined according to 'Compliance-Based Beam Method'. After the compliance measurements, a least squares linear regression of the following form was performed:

$$C = C_0 + m'a^3 \qquad (2)$$

Where C is the loading point compliance, C_0 and m′ are the compliance calibration coefficients and a is the crack length.

The specimen was then positioned on the supporters with crack length to span length ratio=0.25, and loaded until the delamination started to grow from the insert. The Mode II fracture toughness was evaluated based on the compliance calibration as

$$G_{IIC} = \frac{3m'a^2P_c^2}{2b} \tag{3}$$

Where m′ is the compliance calibration coefficient determined before, P_c is the maximum force before delamination propagation begin, a is the crack length used in the fracture tests, and b is the specimen width (Baere, et al., 2012). The value of G_{IIC} and m′ are shown in Table 3:

Table 3 Summary of values of m′ and G_{IIC}

	Room temperature test			Low temperature test		
	RT curing	80℃ curing	UV curing	RT curing	80℃ curing	UV curing
m' ($N^{-1}\cdot m^{-2}$)	0.3067	0.3075	0.4285	0.2663	0.3061	0.3458
G_{IIC} ($J\cdot m^{-2}$)	985.9	1108	1254	1132	1248	1479

The result presents that the mode Ⅱ fracture toughness of RT curing, 80℃ curing and UV curing shown an obvious progressive relation and the highest value came out on UV curing condition both in ambient and the low temperature environment. The higher facture toughness value reveals a stronger resistance to brittle fracture when a crack is initiated already. And it is tending to have more possibility to endure ductile fracture also (Wu & Anthony, 2017; Bruno, et al., 2018; Xin, et al., 2018; Raghu Prasad & Pavan Kumar, 2008). The distinction of G_{IIC} values in three curing conditions is considered as the consequence of the different epoxy crystallinity content as well as the strength of resin itself, which indicate the UV repaired specimens have high curing degree and excellent matrix strength. The differences occurred on low temperature environments are considered as the rigid matrix and a denser chain of molecules caused by low temperature shrinkage which have a block effect of crack propagation.

4.3.3 Interlaminar shear strength

Fig. 34 illustrates the result of the short beam shear test of repaired GFRP specimens. As expected, UV repaired specimens show a higher interlaminar shear strength. However, 80℃ repaired specimens reveal a lower strength than room temperature repaired specimens.

During the test, it is noted that indentation damage around the loading indenter on the top surface preceded interlaminar delamination in the center of the specimen. In this SBS test processing, the ILSS result is hypothesized representing the shear strength of the adjacent laminae between the repair layer and the fundamental matrix (Pantano, et al., 2002; Ke, et al., 2016). This indicates that the 80℃ repaired specimens have a weaker adhesion strength between the repair patches and the fundamental matrix, in contrast to the UV repaired specimens.

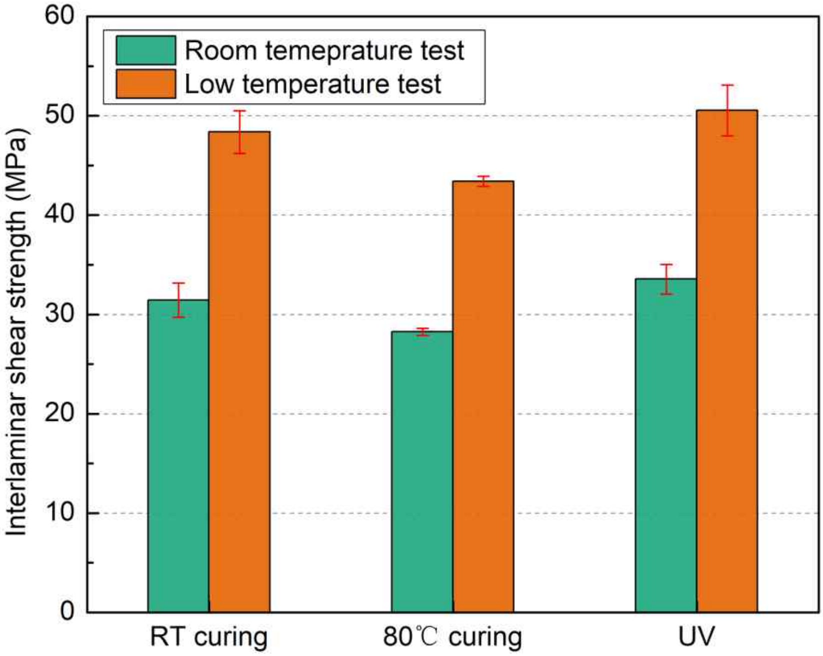

Fig. 34 Interlaminar shear strength of different test condition and curing temperatures

4.3.4 Microscopic observations

Fracture surfaces of short beam shear test specimens under room and low test temperature were observed by scanning electronic microscope as shown in Fig. 35.

In Fig. 35(a), severe delamination both in external patches and external-fundamental interlaminate were observed, together with the fiber breakage that occurred in the contact position of indenter and external patch, for which can be considered as the essential factor to restrict the ultimate strength. However, fiber breakage cannot be seen in Fig. 35(b), instead by the enormous separation of the external-fundamental interlaminates. The delamination surface presents a smooth morphology which reveals the weak cohesive bonding. This fracture pattern validates the low ILSS value in RT repaired specimens. Fig. 35(c) shows several delamination cracks, but the propagation behavior was limited which made the cracks uncritical. Fig. 35(d) illustrates the UV repaired specimens tested under low temperature which also have several blocked delamination cracks but with a fewer crack number. The fracture micrographs of UV repaired specimens demonstrate the strong nature of photo polymerizable resin and stronger bonding between laminates. Also, the ability to impede the crack propagation is the crucial factor for obtaining better interlaminar shear strength, which is in consistency with the mode II fracture toughness result.

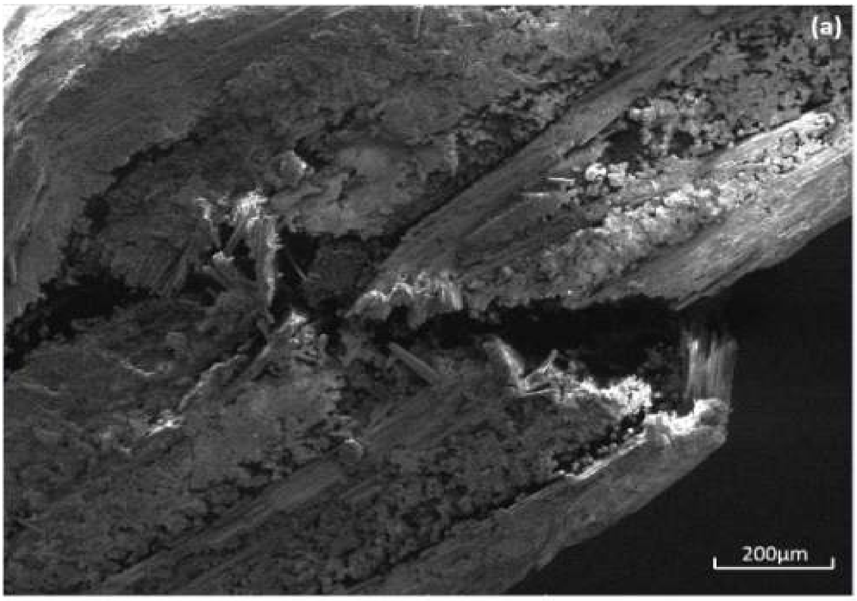

(a)

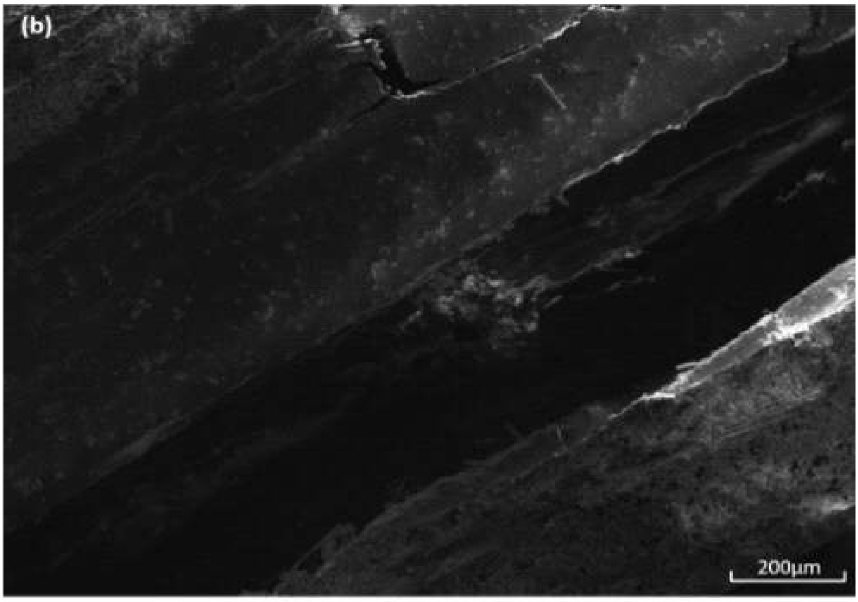

(b)

-continued-

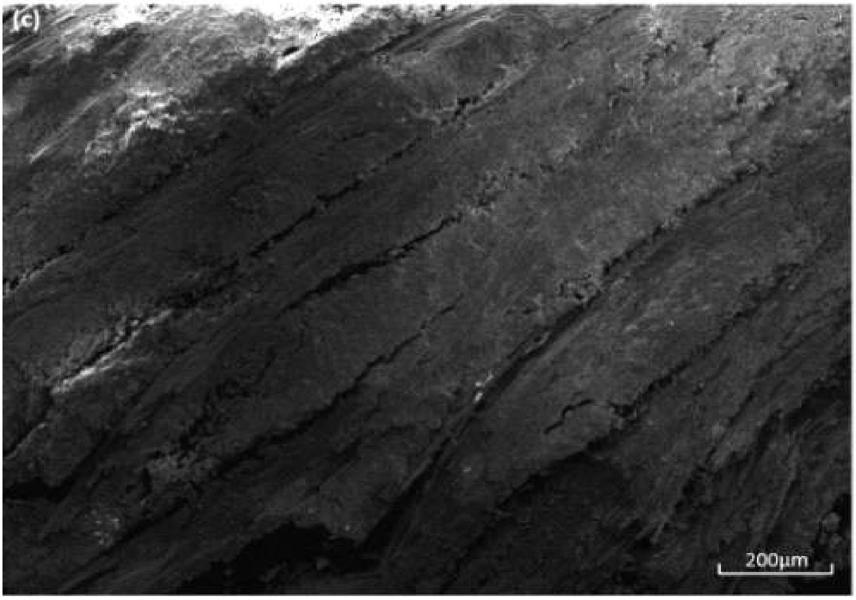

(c)

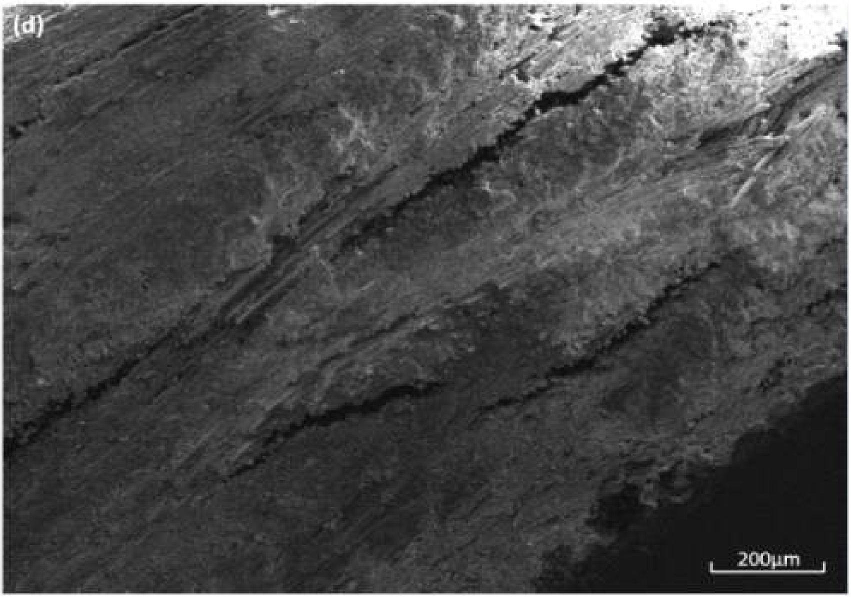

(d)

Fig. 35. SEM micrographs of fracture surfaces in (a) RT repaired room temperature tested specimen, (b) 80℃ repaired room temperature tested specimen, (c) UV repaired room temperature tested specimen and (d) UV repaired low temperature tested specimen

4.4 Conclusion

Based on the test results, the following preliminary conclusions are obtained:

(1) The utilization of photo polymerizable resin in GFRP remediation features in in-situ, high-speed, easy-operation and cost-effective aspects as well as good adaptability in the low temperature service environment. photo polymerizable resins have the potential as the alternative of conventional epoxy resin to conduct GFRP remediation.

(2) The mechanical properties tested in low temperature all show higher values than in ambient environment which are owing to the high external-fundamental laminate interfacial bonding strength and low velocity of crack diffusion. Moreover, the residual thermal stress at low temperature also exerts an influence on the ultimate strength.

(3) The post-curing repaired specimens have a better G_{IIC} value which is considered as the rigid matrix and a denser chain of molecules but lower bonding stress from the outcomes of short beam shear test comparing with ambient curing.

(4) The microscopic observations intuitively reveal the diversities between different repaired conditions which RT and 80℃ repaired specimens exist an external-fundamental laminate interfacial debonding. Meanwhile, UV repaired specimens show impediment of crack propagation especially in low temperature environment which is compatible agrees with the result of mode II fracture toughness.

5. Durability of UV repaired GFRP among Acidic Atmosphere

Photo polymerizable resins, as a novel matrix material and the alternative for thermal polymerizable resins, have drawn attention because of their short operation time, low price and low equipment requirements. This chapter investigate the durability of photo and thermal polymerizable resin repaired GFRP in long term acid atmosphere exposure environment, which represent the typical harsh wind turbines service environment. During the experiments, the fundamental GFRP specimens fabricated by wet prepreg manufacture technique were pre-damaged and then repaired by attaching an external photo or thermal polymerizable resin impregnated glass fabric patches followed by UV curing or room temperature curing, respectively. The repaired specimens were positioned into a laboratory-fabricated hermetically-sealed condensation device. 10 vol.% sulphuric acid (pH=0.76) was chosen as the source for generating the acidic atmosphere. The total ageing time sustained for 8 weeks (over 1,300 hours) and during every week, tensile, bending, SBS and DCB tests were performed. Glass transition temperature and micromorphologies of aged specimens were obtained for the durability assessment. The results reveal that the UV repaired specimens have better mechanical properties and stability compared to RT repaired specimens during acid ageing.

5.1 Introduction

As a significant type of novel sustainable development energy, wind power generation not merely save the routine energy resources, but also decrease pollution of the environment to bring preferable economic benefits and social benefits (Lee, et al., 2015; Thomas & Ramachandra, 2018). Nevertheless, the geometrical form and the manufacturing technique make the wind turbine blade more susceptible to damage (Tsai, et al., 2009). With the growing number of glass fiber reinforced composites structured wind turbines now in service, their maintenance is becoming an urgent issue (Gholami, et al., 2013). The repair techniques used recently are the scarf and lap (single or double) repair by wet hand lay-up or by the use of prepreg. The investigation of a remediation methodology of GFRP wind turbine blades to achieve rapidly and cost-effectively repair in a specified service environment is necessary.

UV irradiation curing technology is well established in many industries for its advantages like easy-operation, reduced costs and rapid production. However, for long-term harsh environmental exposure, the mechanical properties may exist further degradation, which has not been thoroughly examined to date (Thomas & Ramachandra, 2018). Although some mechanical devices were proposed for debonding failure prevention (Fu, et al., 2017; Wang & Zhou, 2017), environmental deterioration is challenging to impede (Feng, et al., 2014; Surendra, et al., 2007). Accurate service life prediction and durability evaluation methods are still in need (Zhai, et al., 2016; Amaro, et al., 2013). Thus, it is necessary to clarify the damage mechanism and predict the mechanical degradation of repaired GFRP under harsh environmental exposure.

Guoqiang Li, et al. (2013) drawn a conclusion that The photo polymerizable resin is a fast, strong, durable, and cost-effective repair method and can replace the ambient environment curing resin and the heat activated prepreg resin. For UV repaired specimens, conditioning by UV radiation can increase the residual tensile strength. Basma Hasiaoui, et al. (2018) manufactured GFRP with photo polymerizable resin matrix and found that when applying longer vacuum and impregnation steps, the specimens can lead to high flexure and shear strength. In this chapter, laminated specimens were repaired by thermal or photo polymerizable resin separately. The ageing processing under acidic environments after specimen repair was conducted lasting for 8 weeks as the simulation of typical wind turbine blades service environments. The mechanical properties including tensile and bending properties after a long time acidic environment ageing were investigated. DCB and SBS tests were conducted for evaluating the through-thickness properties. Mechanical tests were performed at the end of every week. Differential scanning calorimetry (DSC) was employed to do the thermal analysis of the resins before and after ageing. The microscopic morphologies of specimen surface were then observed by SEM.

5.2 Experimental works

5.2.1 Materials

Woven plain glass fabrics were supplied by GM composite Co., Ltd. photo polymerizable resin (TB 3033B, supplied by Three Bond Holdings Co., Ltd.) was used for external glass fabric impregnation. Thermal polymerizable epoxy resin (KFR-120V, supplied by KUKDO chemical Co., Ltd) and hardener (KFR-141, supplied by KUKDO chemical Co., Ltd) were used as the matrix for fundamental specimens and external glass fabric patches. The UV lamp (UVCure-60PH, supplied by LICHTZEN Co., Ltd) was employed as the UV source for curing processing. The chemical solvent of H_2SO_4 and NaOH were both supplied by ThreeBond Holdings Co., Ltd for performing the acid ageing and glass fabric treatment, respectively.

5.2.2 Fundamental specimens fabrication

The fundamental specimens preparing for further repair were fabricated using wet prepreg manufacture technique. During the processing, 20 laminae of glass fabric woven plains with dimensions of 300 mm × 500 mm were used as the reinforcement, epoxy resin and hardener were selected as the matrix. All laminates were resin impregnated and consolidated by FRP roller, a piece of peel ply and vacuum bag were then covered upon the glass laminates. A vacuum pump was connected to the sealed mold and vacuum phenomenon was conducted for estimating entrapped air and redundant resin. Wet prepreg set-ups were stored in oven for curing processing at 80℃ and settled for 12 hours with uniformed heating and cooling rate of 30 minutes. After demolding, the fundamental samples were cut into tensile, bending, SBS and DCB specimens by CNC cutting machine. The configuration of specimens all strictly observed ASTM standards.

5.2.3 Specimens remediation and ageing conditioning

Prior to repair step, glass fabric patches were proceeded surface treatment in 5 wt.% NaOH solution bath with 3 hours heating, then rinsed by distilled water sufficiently and dried by hot plate for removing the contamination. In the repair procedure, every specimen was ground by sanding machine (Model 3037 supplied by Astro Pneumatic Co., Ltd) on the aimed area in order to increase the surface roughness and slightly reduce the thickness.

The tensile specimens have a rectangular dimension of 36 mm × 200 mm × 3 mm according to ASTM D 3039. The specimens were firstly pre-damaged by an electrodrill in the middle (Φ = 6 mm), followed by four glass fabric patches (36 mm × 36 mm) attached on the ground surface with photo polymerizable resin or thermal polymerizable resin (weight ratio of resin:

hardener = 100:30) impregnated. An extra piece of double-sized cover layer (72 mm × 36 mm) was then attached upon. The photograph and schematic of the tensile specimen remediation are shown in Fig. 36. Bending and SBS specimens also have the configurations according to ASTM D 790 of 12.7 mm × 127 mm × 3 mm, and ASTM D 2344 of 18 mm × 6 mm × 3 mm, respectively. Similar to tensile specimens, four fully-covered and resin-impregnated glass fabric patches were attached on the ground specimen surface for implementing the repair processing. The DCB specimens have the length of 130 mm with an initial crack length of 65 mm from the specimen end or 50 mm from the load line. The initial crack length was realized by inserting the Teflon ply in the mid-plane of two half-laminated specimens which had only 10 laminae by adhering them using a photo or thermal polymerizable resins. The photograph of repaired DCB specimens is illustrated in Fig. 37.

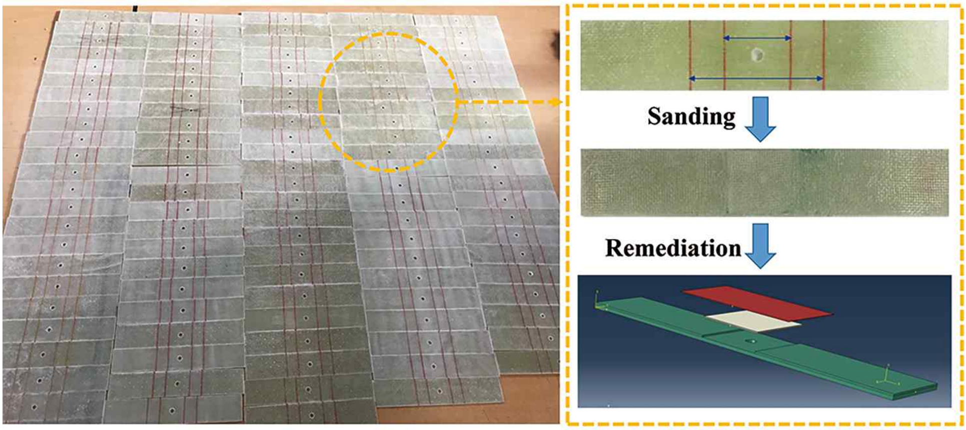

Fig. 36 Photograph and schematic of tensile specimen remediation

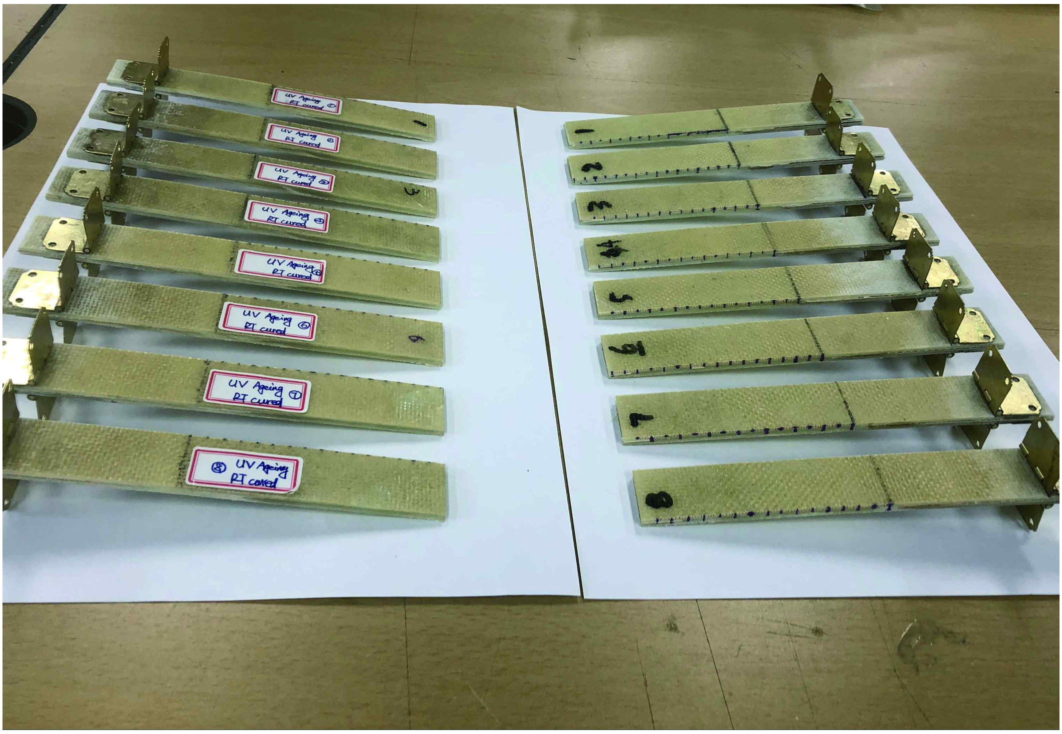

Fig. 37 photograph of repaired DCB specimens

The acidic atmosphere conditioning was proceeded according to ASTM D 5229 in a laboratory-fabricated hermetically-sealed condensation device that contains the sensor of temperature and humidity which are shown in Fig. 38. 10 vol.% sulphuric acid (pH=0.76) was chosen as the solution for proceeding acid ageing and the humidity inside the device was controlled by evaporating sulphuric acid. The evaporation was adjusted through a capillary phenomenon by using cotton thread to connect sulphuric acid and heater until achieving the wanted humidity level of 80%RH. The specimens were positioned inside the device equably without surface occlusion for achieving the uniform hydrosphere absorption.

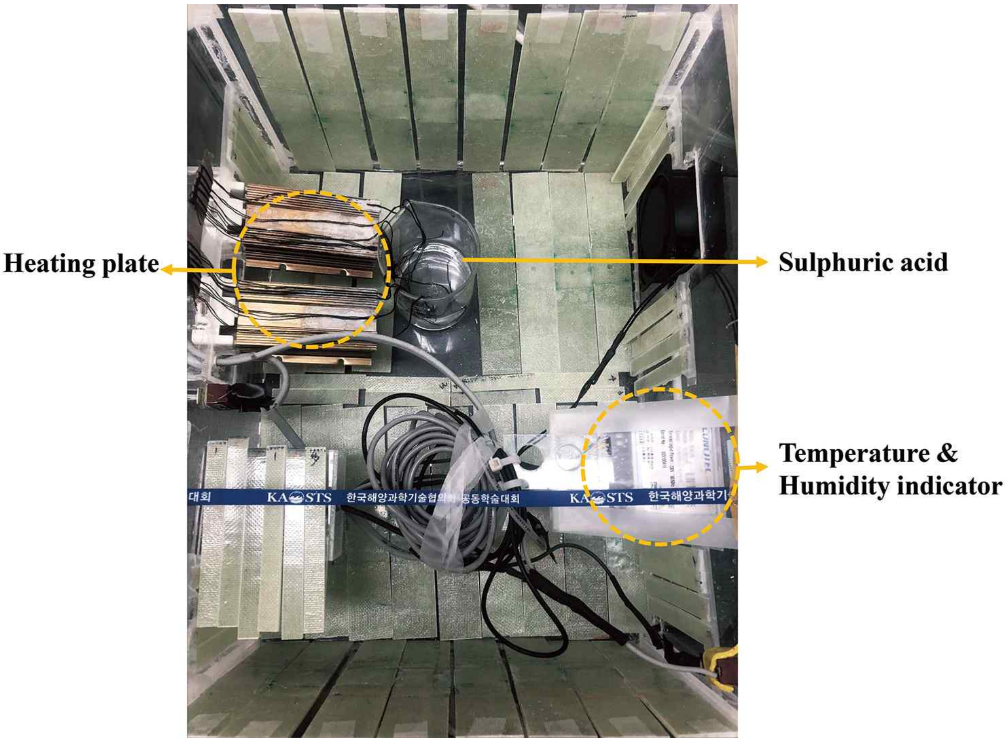

Fig. 38 Laboratory-fabricated condensation device for acid ageing conditioning

5.2.4 Characteristics

Specimens were taken from the condensation device and performed tests every week lasting for 8 weeks. Resin samples were taken out after 8 weeks ageing to do the evaluation on thermal property. Tensile, bending and SBS tests were all carried out in a universal testing machine (UTM KDMT-156) with a displacement rate of 2 mm/min according to ASTM standard. DCB test was performed referencing to ASTM D 5528 in an electromechanical testing machine (ETM 102A) with a displacement rate of 2 mm/min. Thermal analysis was conducted using differential scanning calorimetry (DSC N-650) instrument with the heating rate of 2℃/min ranging from 25℃ to 200℃.

5.3 Results and discussion

5.3.1 Tensile and bending strength

The tensile and bending strength tested every week during 8 weeks acid ageing of UV and RT repaired GFRP specimens are illustrated in Fig. 39. The tensile and bending strength of UV and RT repaired specimens both show a downward tendency. Fit-slopes of two UV repaired specimens the fitting lines are −1.71 and -0.34 respectively. Meanwhile, the fit-slopes of tensile and bending strength are -2.67 and -3.52 for the RT repaired specimens, respectively. The load-displacement bending curves of UV and RT repaired specimens after acid ageing are shown in Fig. 40. The elastic modulus and ultimate strength of UV and RT repaired specimens both have a significant decrease.

The decrease on tensile and bending strength after acid ageing is caused by means of chemical decomposition of the corroded layers. The fiber and matrix both have the essential contribution to the property degradation. The corrosion on glass fiber is considered as the ion-depletion behavior which is preferential leaching of non-siliceous oxides of the calcium, aluminum (CaO, Al_2O_3) in its major amount which was investigated and reported by Q. Qiu and M. Kumosa (Qiu & Kumosa, 1997). The depletion of calcium in sulfuric acid is ruled by union-controlled leaching because the sulfate anion can form an insoluble salt with the calcium ion. Acid ageing effect on the polymer resin has complex corrosion behavior in an acid environment and according to the research by Hideki, et al. (2003), the adding of hardener will increase the penetration speed of sulfuric acid and may change the penetration pattern from surface reaction type to laminate penetration type.

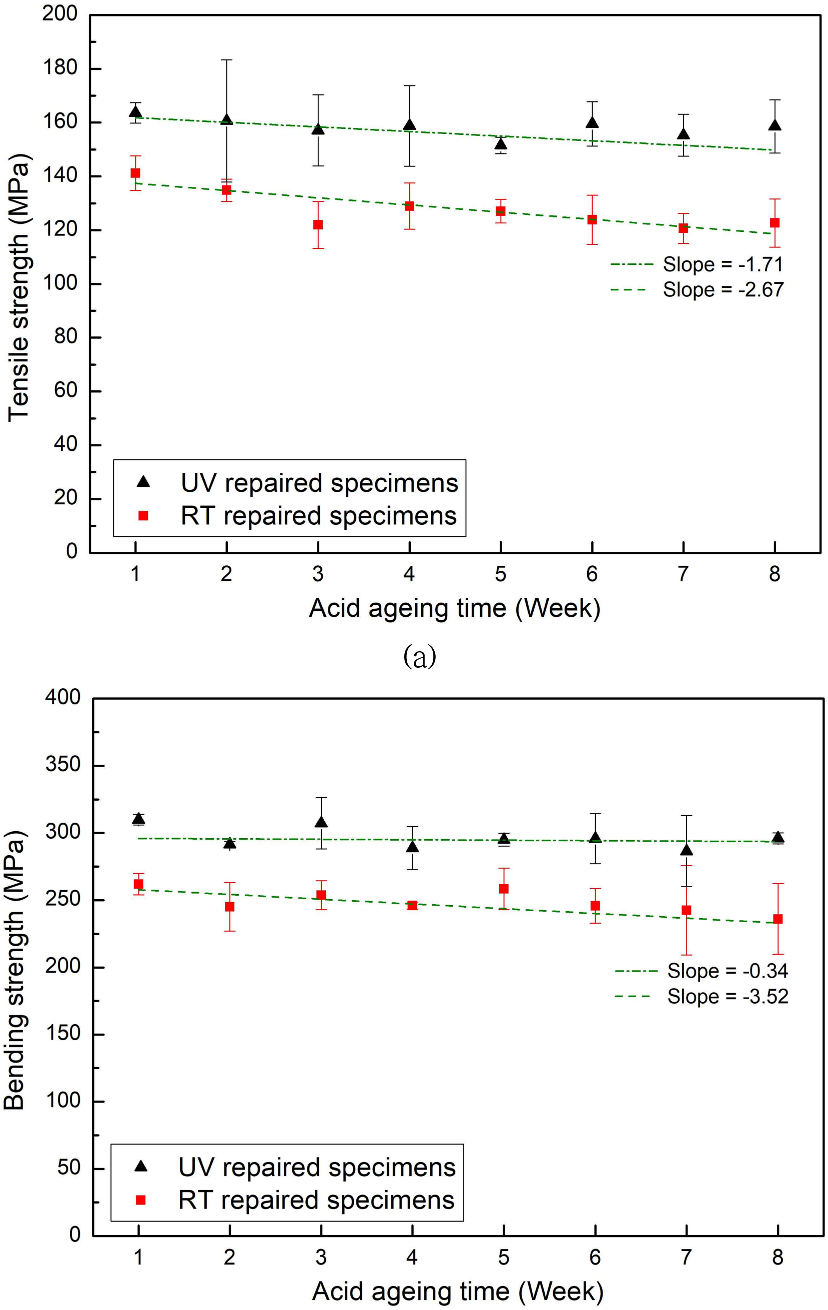

(a)

(b)

Fig. 39 Tensile (a) and bending (b) strength tested every week during 8 weeks acid ageing

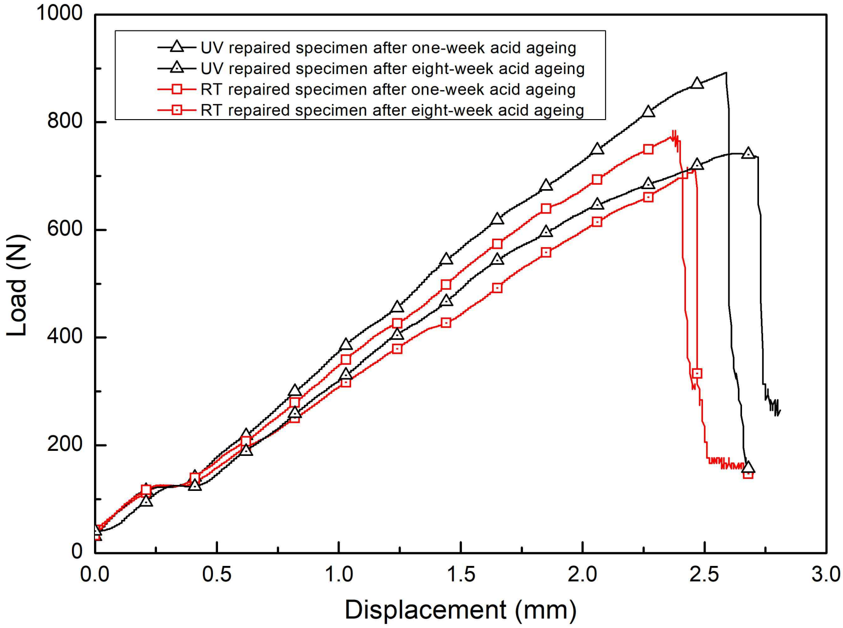

Fig. 40 Load-displacement curves after acid ageing of UV and RT repaired bending specimens

5.3.2 Mode I fracture toughness

In this chapter, the Mode I fracture toughness (G_{IC}), was calculated using compliance calibration method. A least squares fit of the log-log plot of specimen compliance as a function of delamination length was performed to obtain a slop. Where:

$$C=\delta/P \tag{1}$$

$$\text{Log } C = K + n \text{ Log } a \tag{2}$$

Where: C is the compliance, δ is the displacement and P is the load value at the crack propagation point. K is a constant, n is the slope after the least squares fit of log-log plot and a is the crack length. After the n is determined the Mode I fracture toughness G_{IC} is calculated from n along with the P, δ and a values associated with the delamination onset from the insert:

$$G_{IC} = \frac{nP\delta}{2ba} \tag{3}$$

The results of the mode I fracture toughness at crack initiation and 2nd propagation of UV and RT repaired specimens after 1 week and 8 weeks acid ageing are shown in Fig. 41. $G_{IC\text{-initiation}}$ is presented to the Mode I fracture toughness of the onset of the initiation crack while the $G_{IC\text{-propagation}}$ is presented to the Mode I fracture toughness of 2nd crack propagation. The $G_{IC\text{-initiation}}$ and $G_{IC\text{-propagation}}$ values of UV repaired specimens all perform higher than RT repaired specimens in acid ageing condition.

The $G_{IC\text{-initiation}}$ and $G_{IC\text{-propagation}}$ values reveal the crack resistance ability at crack initiation and propagation stages. The excellent performance in crack resistance ability of UV repaired specimens demonstrates a better stability and reliability of the application of photo polymerizable resin in acid exposure service environments. The stability of interlaminar fracture toughness of UV repaired specimens are considered as the consequence of the less sensitivity of acid corrosion in acid exposure environment. In the observation of the interlaminar fracture toughness results of RT repaired specimens, the values of $G_{IC\text{-propagation}}$ perform gentler and smoother reduction which differ with values of $G_{IC\text{-initiation}}$. That is because that the outer surfaces of specimens were exposed to the ageing environments at the very beginning and suffered the longest exposure time overall. The severe property degradation of glass fabrics and resins contributed to the noticeable $G_{IC\text{-initiation}}$ decrease but for the $G_{IC\text{-propagation}}$, as occurred at the 2nd crack propagation, performed a more gentle deterioration. The fracture surfaces of DCB specimens after 8 week acid ageing obtain by optical microscope are shown in Fig. 42. The UV repaired specimens present a total delamination and adhesive fracture morphology reveal by exposed fiber and small through-thickness adhesive fracture on the fabric wrap space, which indicate a strong adhesion retained between matrix and fiber. The RT repaired specimens present a partially adhesive-cohesive fracture morphology and the fracture surface is flatter and smoother than UV repaired specimens which revealed the degraded adhesion.

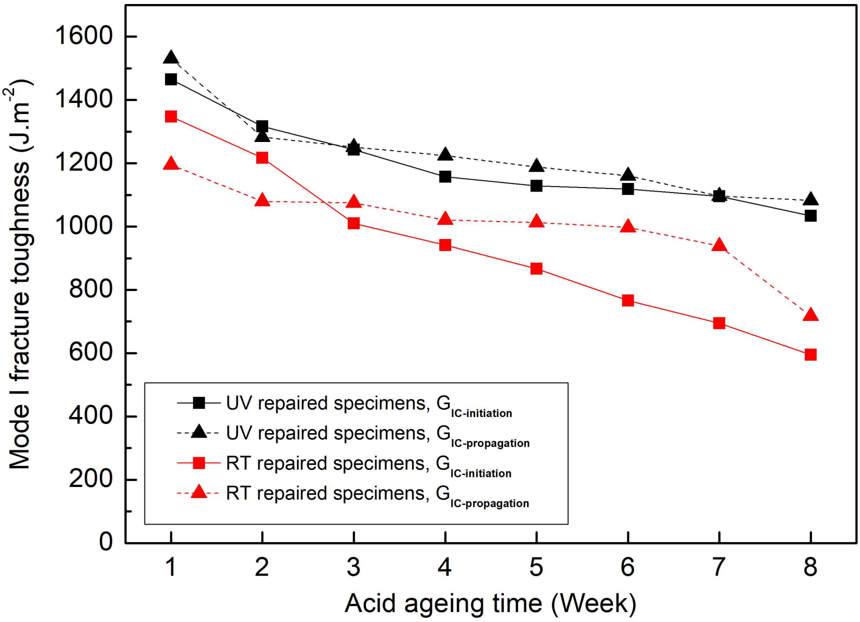

Fig. 41 Mode I fracture toughness of UV and RT repaired specimens after 1 week and 8 weeks acid ageing

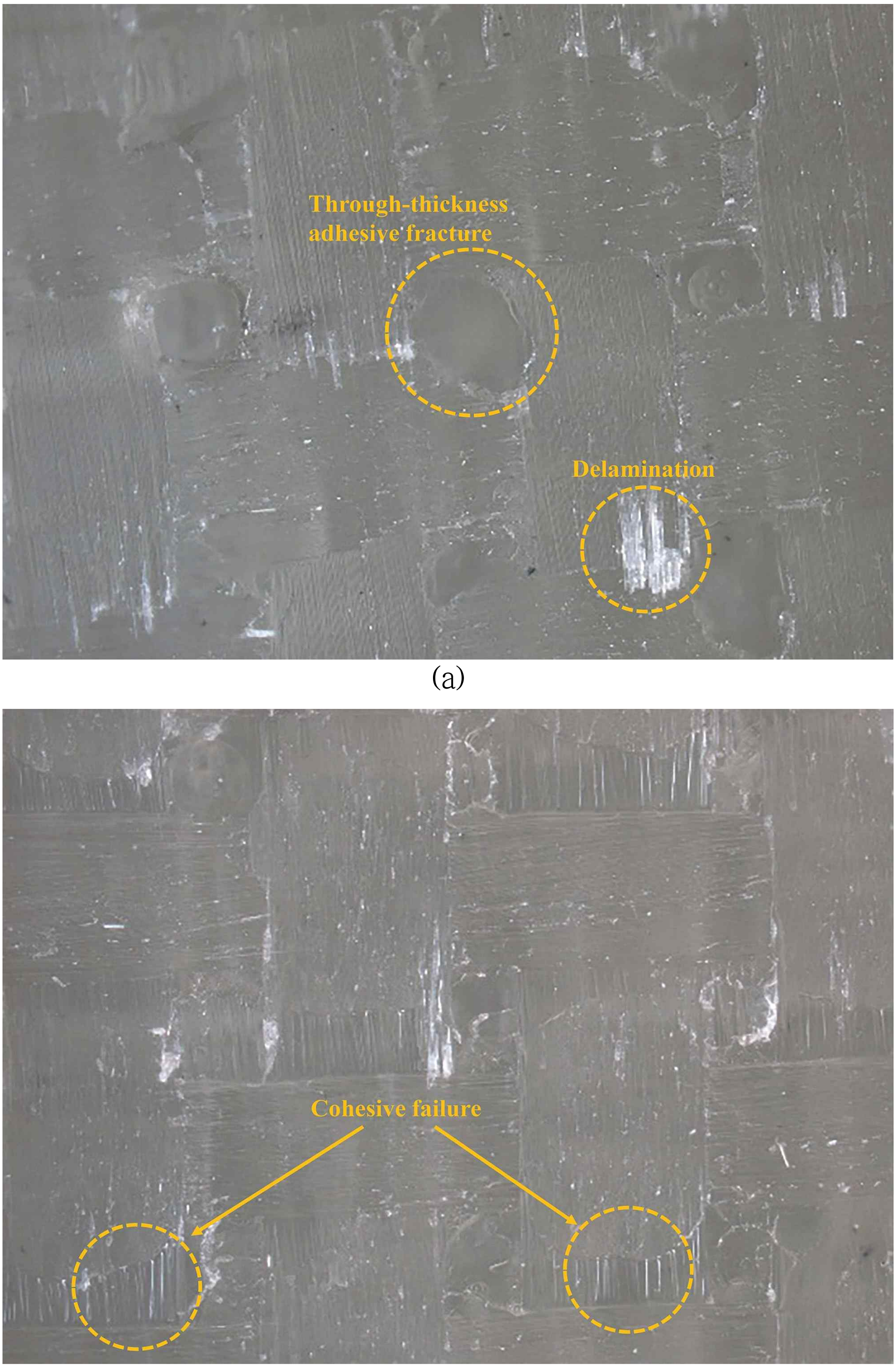

(a)

(b)

Fig. 42 Photograph of fracture surfaces of UV repaired (a) and RT repaired (b) DCB specimens after acid ageing

5.3.3 Interlaminar shear strength

The results of the short beam shear test of repaired specimens after 8 weeks ageing are shown in Fig. 43. As expected, UV repaired specimens show a higher interlaminar shear strength. Decreasing tendencies of interlaminar shear strength are presented in both UV and RT repaired specimens after acid ageing. During the test, it is noted that indentation damage around the indenter on the top surface occurred prior to interlaminar delamination on the intermediate layer of the specimens. In this chapter, the ILSS results are hypothesized to represent the shear strength of the adjacent laminae between the repair patches and the fundamental matrix where the critical failure occurred. The results of ILSS indicate that the RT repaired specimens have a weaker cohesive bonding and shear resistance ability between the glass fabric patches and the fundamental specimens compare to the UV repaired specimens. Also, the results of ILSS are more discrete as the comparison to previous results.

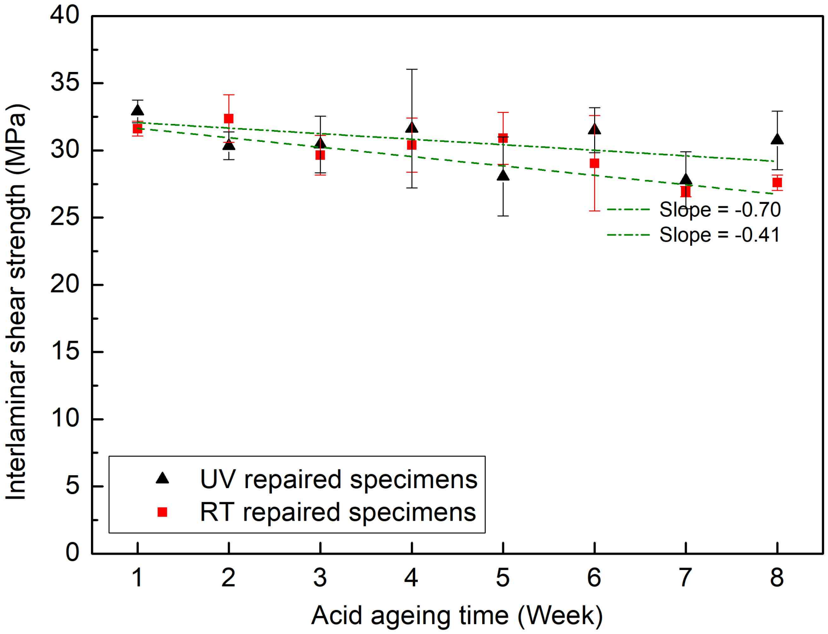

Fig. 43 Interlaminar shear strength of UV repaired and RT repaired specimens after acid ageing during 8 weeks

5.3.4 Thermal analysis

The sequence of differential scanning calorimetry (DSC) curves before and after ageing of UV and RT UV repaired specimens are shown in Fig. 44. According to the DSC curves, the glass transition temperature (T_g) can be obtained. After 8 weeks acid ageing, the T_g value of UV repaired specimens is around 52℃ which is almost the same value as before. The T_g values of RT repaired specimens also has a slight shift around 3℃ before and after acid ageing, as the consequence of the spontaneously post curing behavior even without a certain external heat source. The T_g shift of UV and RT repaired specimens supported other previous results in polymer crystallinity aspect.

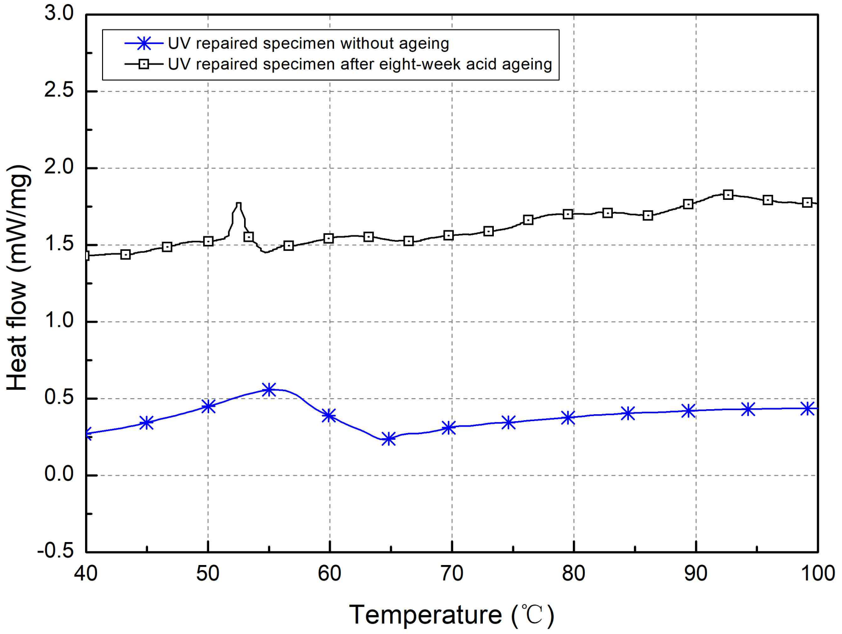

(a)

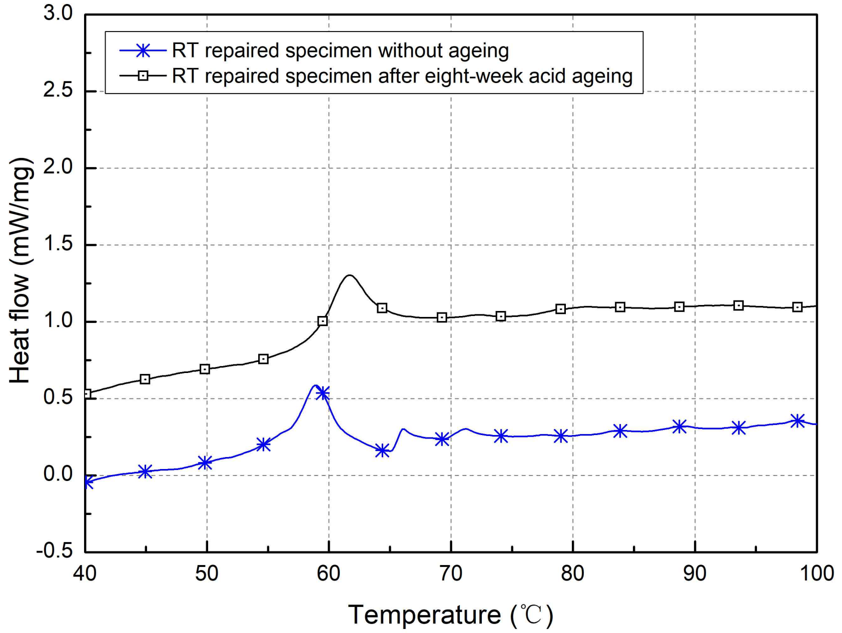

(b)

Fig. 44 DSC curves before and after ageing conditions of photo (a) and (b) thermal polymerizable resins

5.3.5 SEM observations

Surfaces of repaired specimens before and after acid ageing are observed by SEM and shown in Fig. 45. During acid ageing, the thermal polymerizable resin is more sensitive to the acidic environment. Fig. 45(b) shows the RT repaired specimen surface after 8 weeks acid ageing and the obvious corrosion and degradation occurred on matrix part can be observed. The corrosion on its surface formed a huge depression area together with micro porosities which are critical for the attenuation of the fiber-matrix integrity. The forming mechanism of this morphology can be explained by the study of Hammami and Al-Ghuilani. (2004), that the combined action of water and corrosive fluids lead to matrix expansion and the occurrence of pits. The generated blisters, which may start growing by swelling (pressure), will finally collapse and result in severe damage to the integrity and properties. Fig. 45(d) shows the UV repaired specimen surface after 8 weeks acid ageing. In spite of the ineluctable degradation of matrix, the specimens retain the relative smooth surface and exist few micro porosities morphologies. The violent degradation on the matrix of the RT repaired specimens leads to the decrease of comprehensive properties.

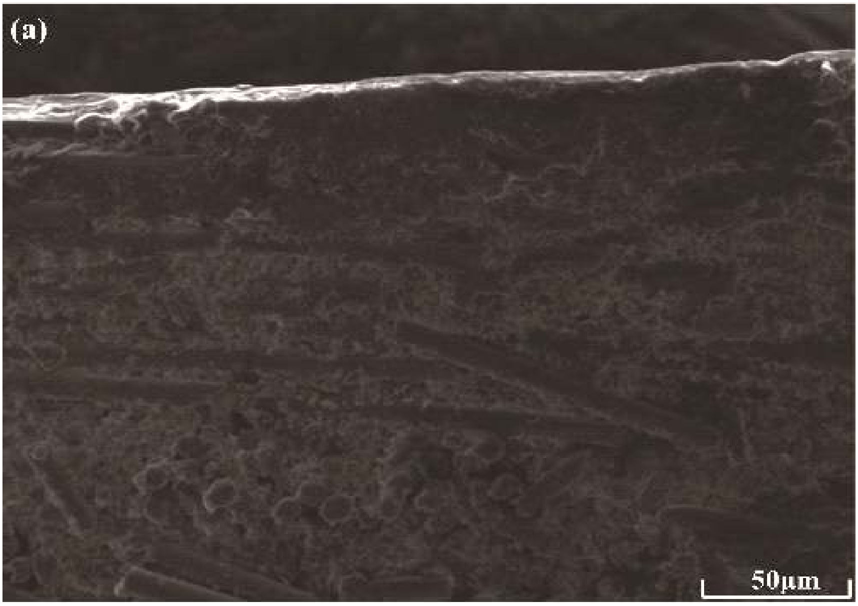

(a)

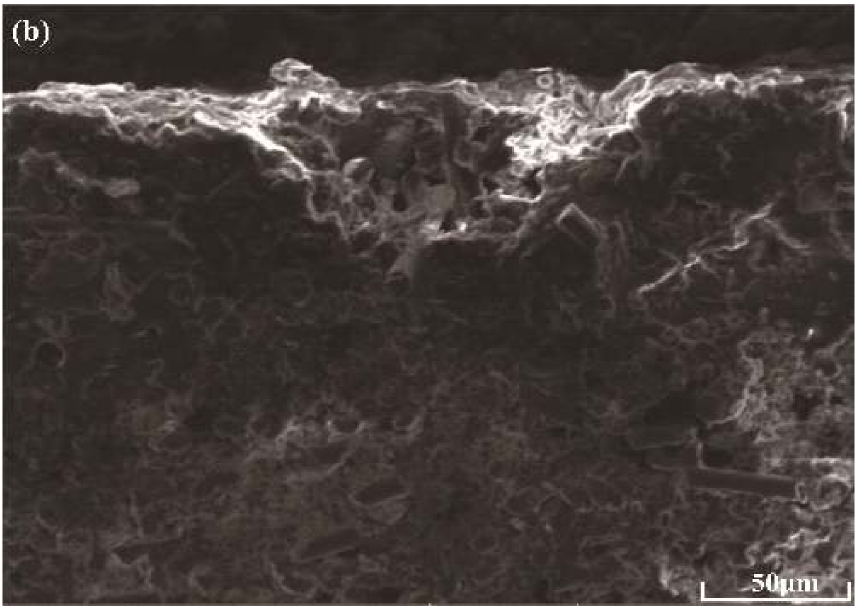

(b)

-continued-

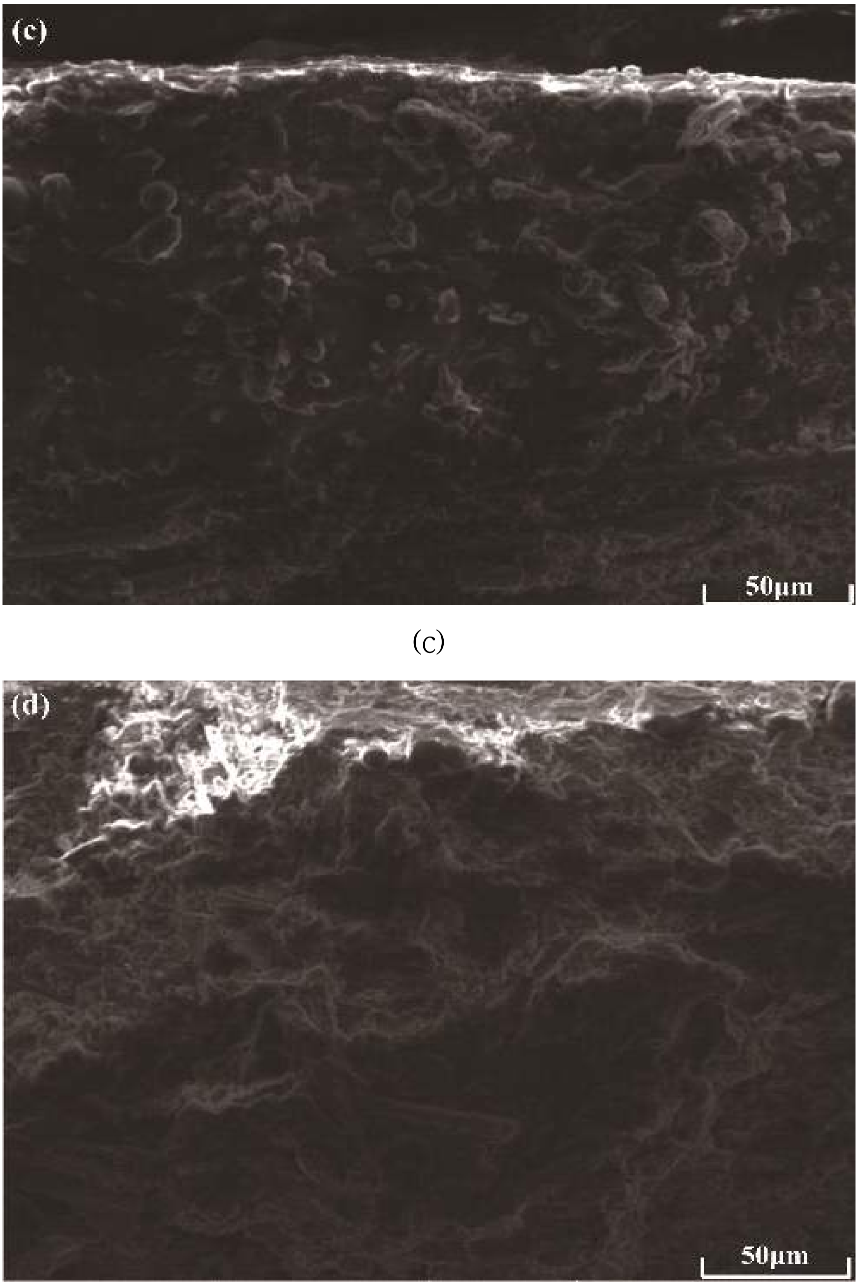

(c)

(d)

Fig. 45 SEM micrographs of surfaces on RT repaired specimen before (a) and after (b) acid ageing and UV repaired specimen before (c) and after (d) acid ageing

5.4 Conclusions

In this chapter, fundamental GFRP specimens fabricated by wet prepreg manufacture technique were pre-damaged and then repaired by attaching an external photo, or thermal polymerizable resin-impregnated glass fabric patches followed with UV curing or room temperature curing, respectively. Ageing processing in an acidic environment was conducted to evaluate the durability. Tensile, bending, SBS and DCB tests were performed; DSC test was employed to do the thermal analysis, and SEM was used to do the surface morphology observation. Base on the test results, the following preliminary conclusions were obtained:

(1) During acid ageing, the strength of specimens degraded due to the ineluctable chemically deteriorated on fiber and resin. The properties decrease rate of UV repaired specimens are slower than RT repaired specimens as the consequence of the photo polymerizable resin have no utilization of hardener, which is a factor to increase the acid penetration speed, during the curing processing.

(2) The T_g values of UV repaired specimens show little distinction before and after acid ageing while that of RT repaired specimens demonstrate a slight increase about 3℃ because of its spontaneous curing behavior. The acid environment leads to negligible changes in the overall curing degree of both photo and thermal polymerizable resins.

(3) During the surface morphology observation, the RT repaired specimens presente massive depression and micro porosities on external surfaces while the UV repaired specimens show milder damaged surface. The violent degradation of RT repaired specimens resulted in their decreased mechanical

properties. In other words, the flaking and degradation of acid-exposed resin surface led to the decreased mechanical properties, while the internal integrity of repaired specimens is almost maintained.

6. Performance of UV repaired GFRP during UV ageing Process

As for the high altitude location and harsh remediation condition of wind turbine blades, a photo polymerizable resin repair method was investigated because of its short operation time and low equip requirement. This chapter demonstrated the durability under UV irradiation environment of photo and thermal polymerizable resin repaired GFRP which is the essential material for manufacturing wind turbine blades. During the experiments, the fundamental GFRP specimens fabricated by wet prepreg manufacture technique were pre-damaged and then repaired by attaching an external photo or thermal polymerizable resin-impregnated glass fabric patches followed with UV and room temperature curing, respectively. Long-term UV ageing (over 1,300 hours) was conducted to repaired specimens by employed a 365 nm wavelength UV lamp. Mechanical properties, thermal properties and surface morphology were evaluated before and after ageing. The results reveal that the UV repaired specimens have better mechanical properties and stability compared to RT repaired specimens in UV ageing environments.

6.1 Introduction

From the 20th century to now, the application of wind turbines showed constant growth to generate clean, renewable and sustainable wind energy. With the development of material technology, GFRP was employed to build the main component of a wind turbine blade in terms of their high specific strength and stiffness, anti-corrosion and reasonable prices. With the extensive serving number, the wind turbine blades have a potential risk of being damaged because of exposure to the hazard environment such as long term intense UV irradiation.

UV light curing technology is well established in many industries for its advantages like easy-operation, reduced costs and rapid production times. The resin formulated with a photoinitiator is the basic concept to realize the photopolymerization which initiates an extremely rapid cross-link cure mechanism, often complete in several minutes or even in several seconds as opposed to several hours (epoxies and prepregs), when under the exposure to UV irradiation. UV curing resins can also cure with sunlight alone and are therefore more practical for field use where additional effort would be necessary to protect the joint from the environment during a lengthier cure, or impractical levels of energy are input into the system to quicken the cure. However, the durability on UV exposure environment needs further assessment.

Mahat, et al. (2016) investigated short (200 hours) and long (300 hours) term UV exposures on the thermal and mechanical properties of CF/PPS thermoplastic composites and found the glass transition temperature, storage modulus, and tensile strength have a significant decrease. Costa, et al. (2010) performed the ILSS and Iosipescu testes of PPS/glass fiber composites after 300, 600 and 900 hours UV exposure. A small actual decrease was observed and the authors suggested that degradation due to UV exposure was only marginal and resulted from surface phenomena. Akonda, et al. (2012) investigated the physical, thermal and tensile properties of regenerated cellulosic, synthetic glass, ceramic and steel fibers, which were thought as the potential enhance factors for glass/silicate composite, after total 240 hours UV exposure. The results showed slightly decreased thermal stability of these fibers because of photo-oxidation.

In this chapter, pre-damaged specimens were repaired by attaching thermal or photo polymerizable resins impregnated external fabric patches. The ageing processing under UV environment after specimen remediation were conducted lasting for 8 weeks to do the durability assessment. Thermal and mechanical properties after long period UV ageing were investigated together with surface morphology observation.

6.2 Experimental works

6.2.1 Materials

The materials used in experimental works were woven plain glass fabrics, photo polymerizable resin, thermal polymerizable resin, NaOH solvent which had the same specifications with materials described in Chapter 5.

6.2.2 Specimens remediation and ageing conditioning

The fundamental specimens for further repair were fabricated by wet prepreg manufacture technique. Total 20 plies of glass fabric woven plain laminae were selected as the reinforcements with the polymeric matrix. The detailed manufacture and curing processing was described in Chapter 5. After curing processing, tensile, bending, SBS and DCB specimens were cut from the fabricated samples using the CNC cutting machine according to ASTM standards. Specimens remediation processing were absolutely the same as that described in Chapter 5. The photograph and schematic of tensile specimen remediation are shown in Fig. 36. For conducting the curing processing of repaired specimens, a piece of transparent bulky glass sheet was put on the repaired specimens with a hole in the center as the venting gate. After that, a piece of over-sized vacuum bag was covered upon and sealed to conduct vacuum atmosphere by a vacuum pump which is shown in Fig. 46. Curing processing was conducted under UV environment with photo polymerizable resin repaired specimens or under an ambient environment with thermal polymerizable resin repaired specimens. The UV curing was realized by irradiation under 365 nm wavelength ultraviolet for 10 minutes and the RT curing was conducted in ambient temperature for 24 hours.

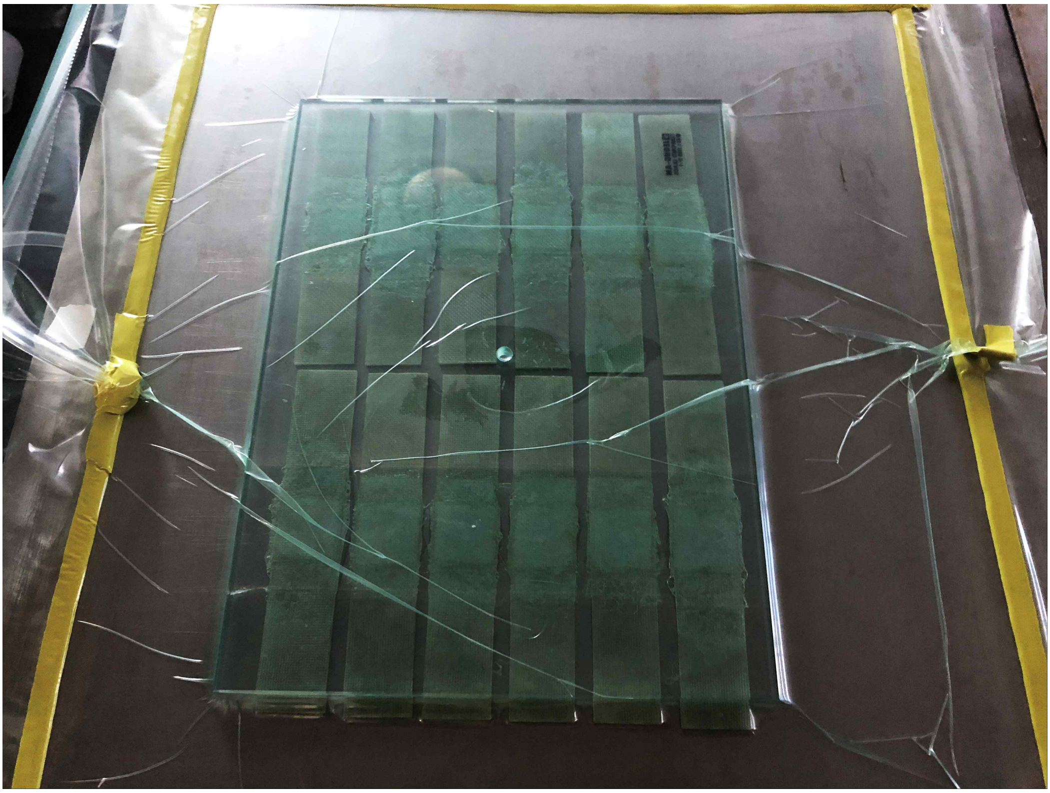

Fig. 46 Mold set-up of UV repaired tensile specimens

The photograph of UV ageing conditioning is shown in Fig. 47. The detailed UV ageing condition was conducted by illuminating the specimens according to ASTM G 154 by using UV lamp (λ =365 nm) with a proper specimen position (height = 600 mm) to realize uniform irradiation. An electric fan was settled to keep the ambient temperature, which was aimed to eliminate the external heat effects and avoid potential danger caused by excessive heat. Specimens for every test condition were taken out and conducted to tests.

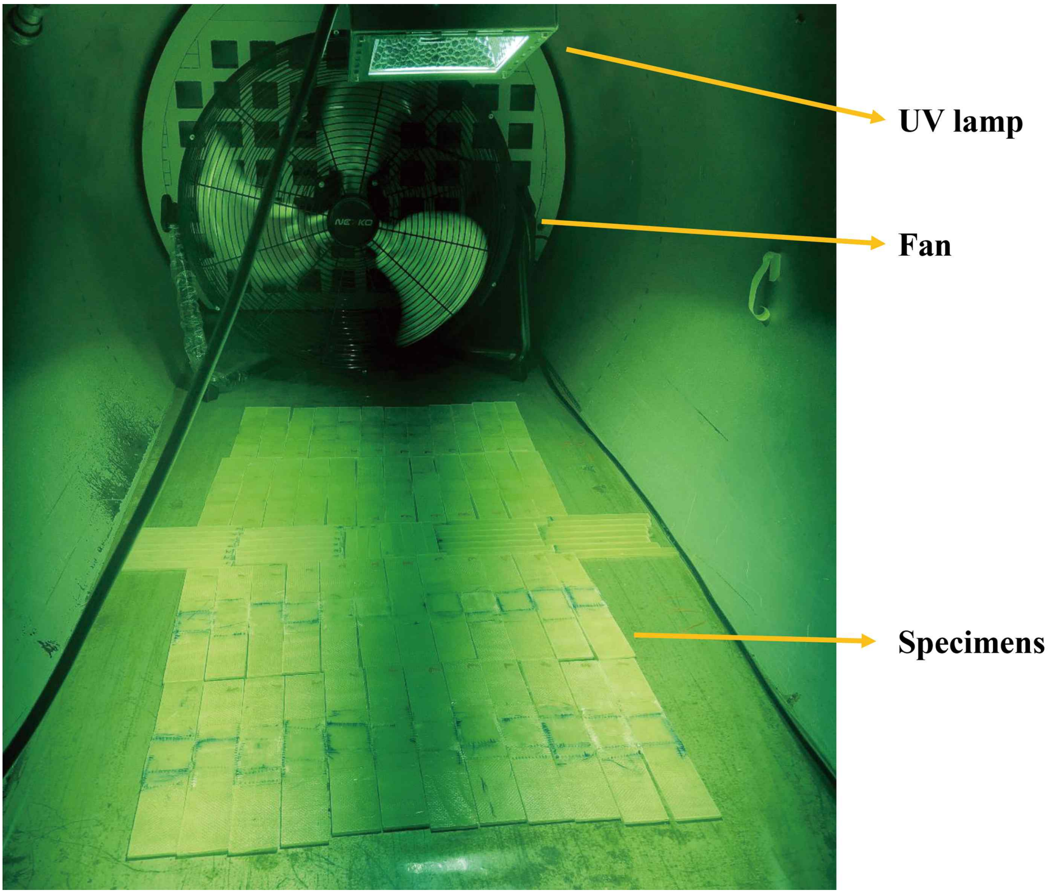

Fig. 47 UV ageing conditioning by using UV lamp

6.2.3 Characteristics

Tensile, bending and SBS tests were all carried out in a universal testing machine (UTM KDMT-156) with a displacement rate of 2 mm/min according to

ASTM standards. Five specimens were included for every test to ensure the reliability. Double cantilever beam (DCB) test was performed referencing to ASTM D 5528 in an electromechanical testing machine (ETM 102A) with an open-force displacement rate of 2 mm/min. The UV ageing of repaired GFRP contained four kinds of test specimens with unique dimensions and photo/thermal polymerizable resin samples. Thermal analysis was conducted using differential scanning calorimetry (DSC N-650) instrument with a heating rate of 2℃/min ranging from 25℃ to 200℃.

6.3 Results and discussion

6.3.1 Tensile and bending strength

Fig. 48 shows the results of the tensile and bending test of UV and RT repaired GFRP specimens tested every week during 8 weeks UV ageing. Note that the fitting lines of experimental data were generated using the least square method for evaluating the increase or decrease tendencies of properties. The tensile strength of UV repaired specimens generally presents a gentle upward trend with ageing time and the slope of the fitting line is 0.82. On the contrast, the tensile strength of RT repaired specimens shows a sharp decline during the ageing processing and the slope of the fitting line is -4.93. The bending strength of UV and RT repaired specimens during UV ageing both demonstrate the decrease tendencies and the slope of the fitting lines is -2.43 and -5.53, respectively.

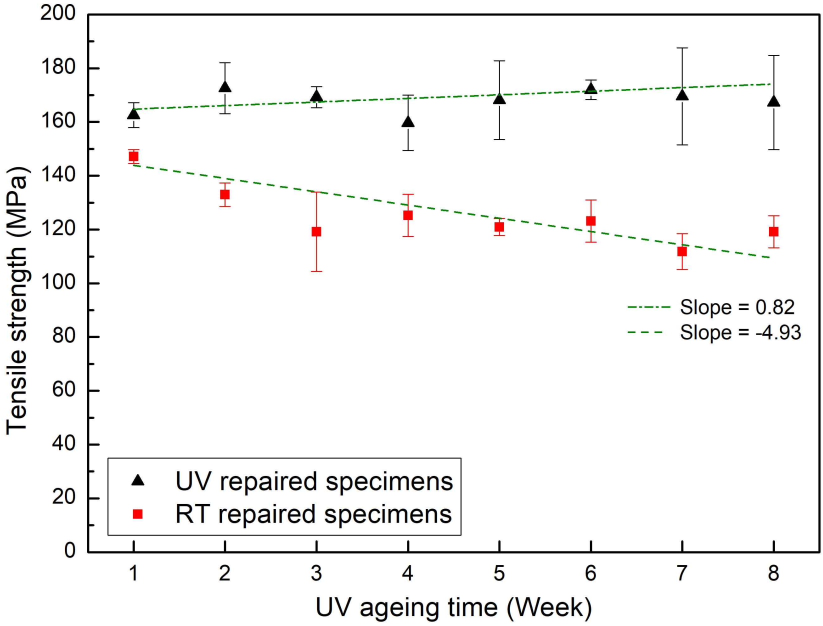

(a)

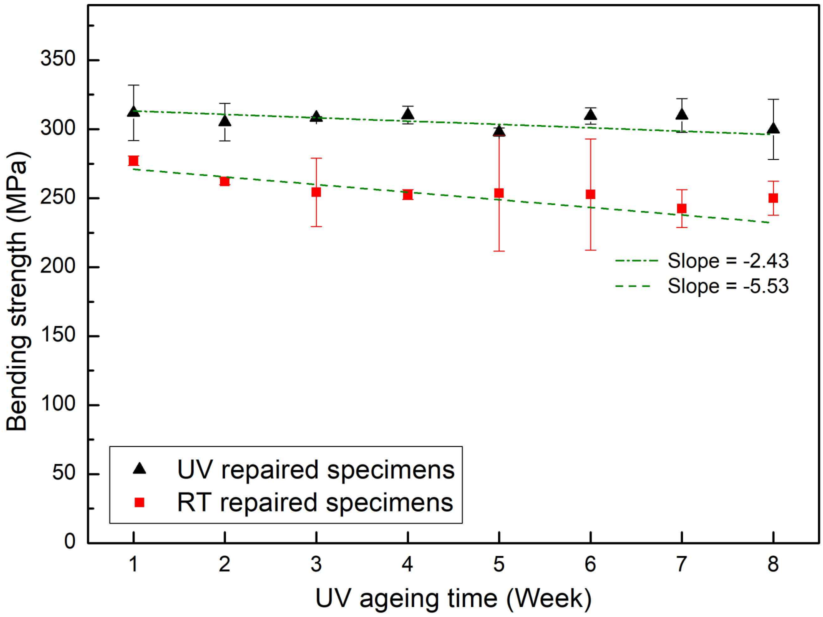

(b)

Fig. 48 Tensile (a) and bending (b) strength tested every week during 8 weeks UV ageing

Fig. 49 shows the load-displacement curves after 1 week and 8 weeks ageing of UV and RT repaired bending specimens. The maximum bending load and elasticity modulus of UV repaired specimens have a little difference after UV ageing while for the RT repaired specimens, the maximum load, elasticity modulus, and elongation at the break all decrease obviously.

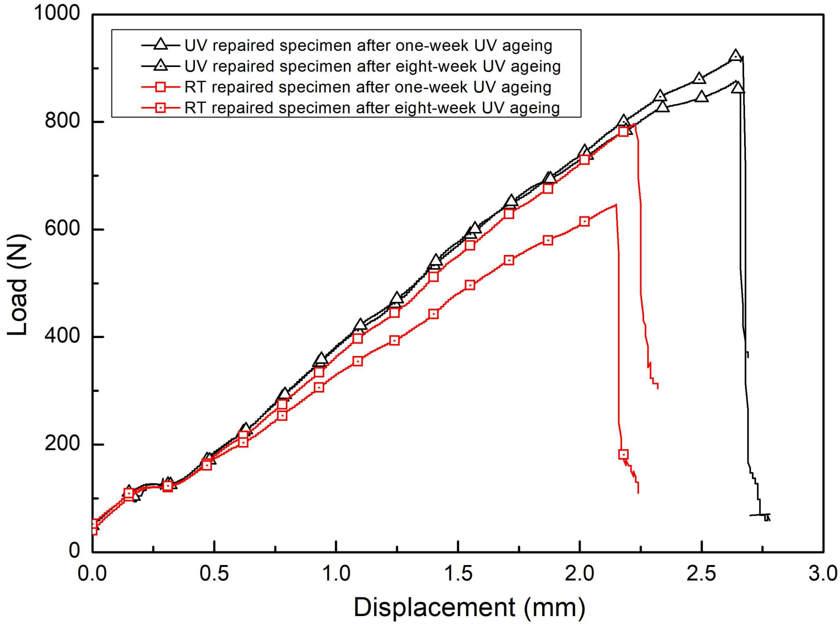

Fig. 49 Load-displacement curves after UV ageing of UV and RT repaired bending specimens

For the UV repaired specimens during UV ageing, the photo polymerizable resin exhibits a post-curing behavior under UV radiation, especially for those resin impregnated glass fabric patches attached on the bottom side. Because of the translucent morphology of glass fabric and photo polymerizable resin, the bottom side impregnated glass fabric patches absorbed less UV intensity compared to the top patches due to UV radiation attenuation. As the result, the curing degree of glass fabric patches decreased progressively from top to bottom in the UV curing stage. During the ageing processing, the specimens were exposed to the UV radiation quite a long period, which gave UV repaired specimens sufficient time for conducting post curing on the bottom glass fabric patches even with the reduced UV intensity. The increased curing degree reveals the increase of crosslink density of photo polymerizable resin, which has a positive influence for making the matrix more strengthened and toughened. The resin with high crosslink density, rigid backbone segments tends to have a high storage modulus, results in a high stiffness that means a low percent elongation and poor energy dissipation.

On the other hand, during the UV ageing processing, the photo-oxidation phenomenon occurred inevitably on both thermal and photo polymerizable resins. Photo-oxidation is a chemical reaction that can reduce the weight of polymer molecule and as a consequence, the polymer becomes brittle and with a reduction of its mechanical properties. The UV repaired specimens have both post curing and photo-oxidation phenomena at the same time during UV ageing processing, which indicates the ‘positive’ and ‘negative’ effects occur simultaneously. As a consequence, the tensile strength has a gentle increase and the bending strength have a little decrease of UV repaired specimens, while the RT repaired specimens have their tensile and bending strength drastically decreased. Of course, the photo polymerizable resin has the limitation of curing degree and at that moment, crosslink density inside the polymer will not increase anymore. The limitation of curing degree is difficult to be decided in this chapter and further study may be required.

6.3.2 Mode I fracture toughness

The Mode I fracture toughness (G_{IC}) was calculated using compliance calibration method. The main concept of this method is to generate a least squares fit of the log-log plot of specimens compliance as a function of delamination length. The detailed calculation processing was demonstrated in Chapter 5. The results of mode I fracture toughness at crack initiation and 2nd propagation of UV and RT repaired specimens after 1 week and 8 weeks ageing are shown in Fig. 50. $G_{IC\text{-initiation}}$ is presented to the Mode I fracture toughness of the onset of the initiation crack while the $G_{IC\text{-propagation}}$ is presented to the Mode I fracture toughness of 2nd crack propagation (Ye, et al., 2011). The $G_{IC\text{-initiation}}$ and $G_{IC\text{-propagation}}$ values of UV repaired specimens both perform higher than RT repaired specimens in UV ageing condition. The $G_{IC\text{-propagation}}$ values of UV repaired specimens always perform higher than their $G_{IC\text{-initiation}}$ values while the $G_{IC\text{-propagation}}$ of RT repaired specimens are lower than their $G_{IC\text{-propagation}}$ values. The excellent performance in crack resistance ability of UV repaired specimens in UV ageing condition demonstrate a better stability and reliability of the application of photo polymerizable resin in UV exposed service environments. The stability of interlaminar fracture toughness of UV repaired specimens is thought as the consequence of their post curing behavior and high damage tolerance in UV exposed environment.

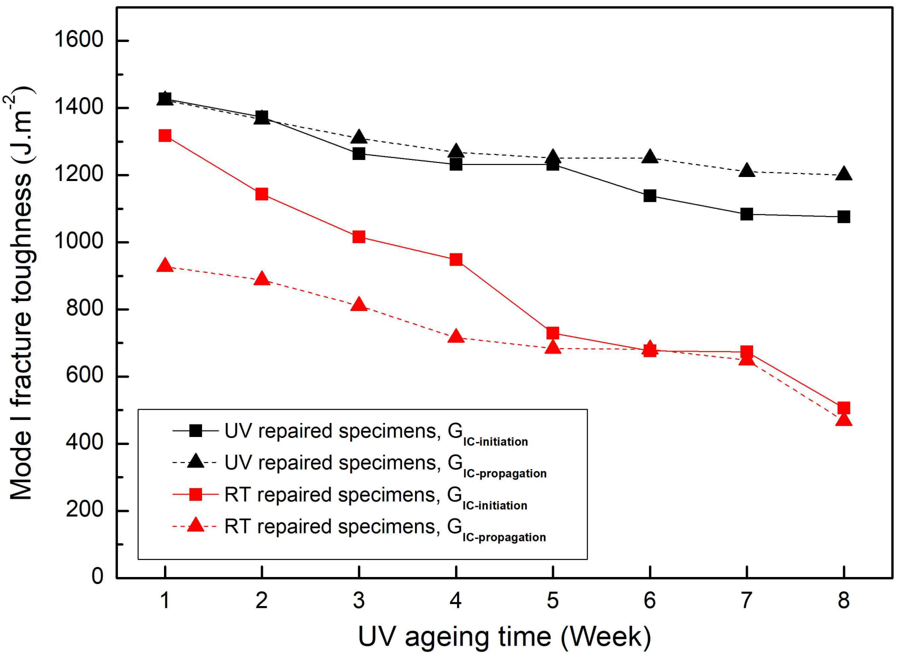

Fig. 50 Mode I fracture toughness after 1 week and 8 weeks UV ageing

6.3.3 Interlaminar shear strength

The results of the short beam shear test of repaired specimens after 8 weeks ageing are shown in Fig. 51. As expected, UV repaired specimens show higher interlaminar shear strength. During the UV ageing condition, the UV repaired specimens show an increase tendency while the RT repaired specimens show a decrease tendency in interlaminar shear strength. During the test, it is noted that indentation damage around the indenter on the top surface occurred prior to interlaminar delamination on the intermediate layer of the specimens. In this chapter, the ILSS results are hypothesized to represent the shear strength of the adjacent layer between the repair patches and the fundamental matrix where the critical failure occurred. The results of

ILSS indicate that the RT repaired specimens have a weaker cohesive bonding and shear resistance ability between the glass fabric patches and the fundamental specimens compared to the UV radiation repaired specimens. Also, the results of ILSS are more discrete as the comparison to previous results.

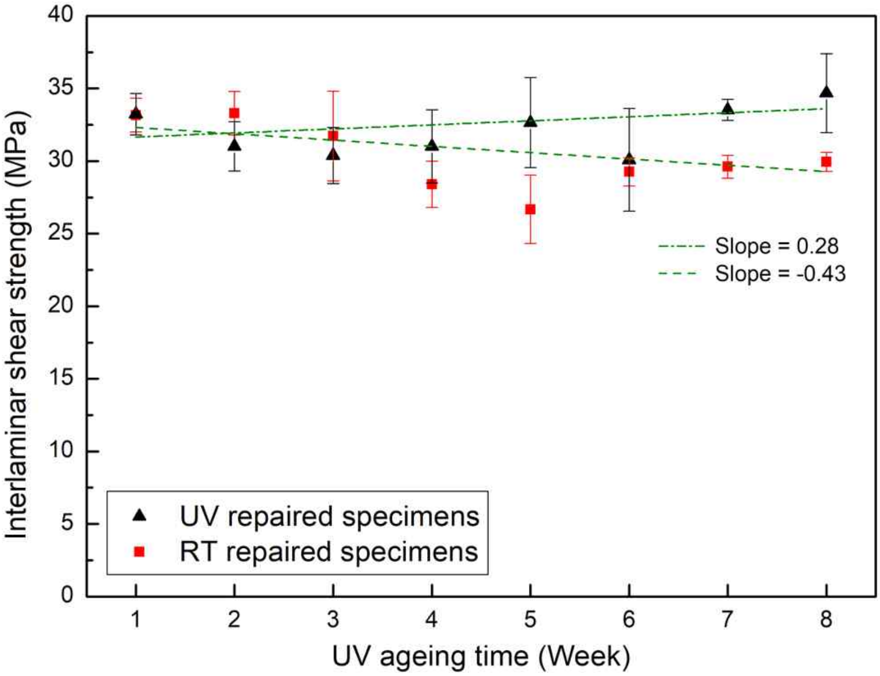

Fig. 51 Interlaminar shear strength after UV ageing during 8 weeks

6.3.4 Thermal analysis

A sequence of differential scanning calorimetry (DSC) curves before and after ageing of the UV and RT repaired specimens are shown in Fig. 52. After 8 weeks UV ageing, the T_g value of UV repaired specomens became higher at 58℃ after 8 weeks UV ageing which indicated a better crystallinity, higher density of chemical crosslink contributed by the UV irradiation. The T_g values of RT repaired specimens also have slight shift around 3℃ before and after UV ageing, as the consequence of the spontaneously post curing behavior even without a certain external heat source. As the T_g values of RT repaired specimens after UV curing a present small distinction, the negligible effect of UV irradiation on the crystallinity of thermal polymerizable resin is validated. The T_g shifts of UV and RT repaired specimens before and after ageing support other previous results in polymer crystallinity aspect.

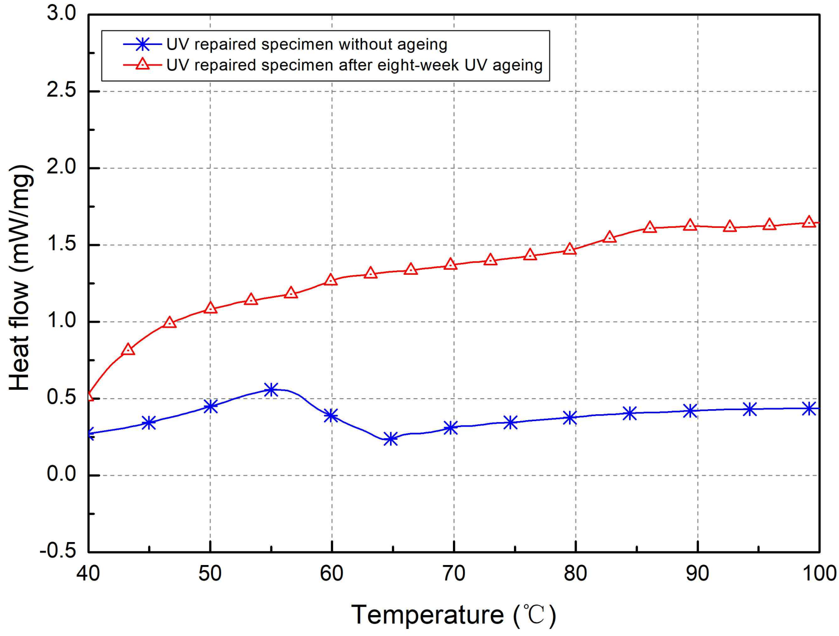

(a)

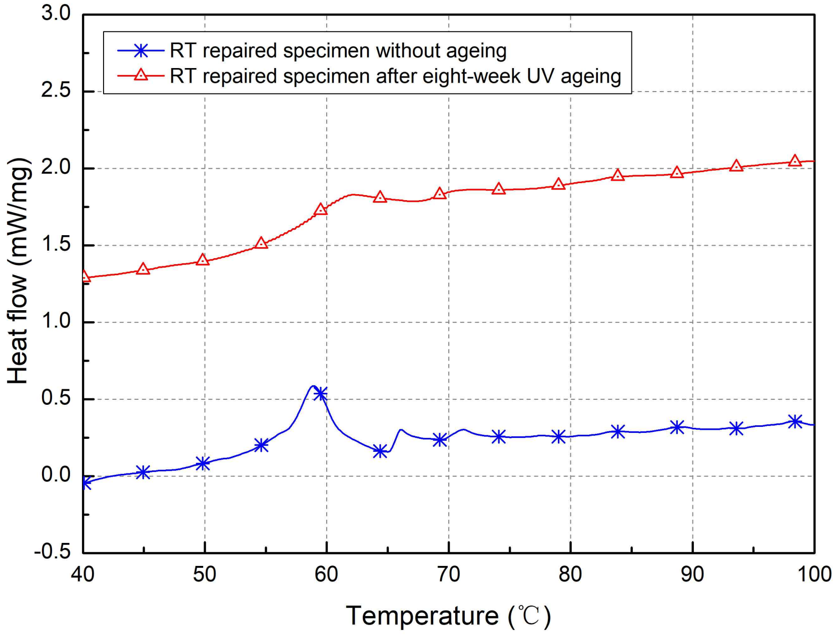

(b)

Fig. 52 DSC curves before and after UV ageing of photo (a) and (b) thermal polymerizable resins

6.3.5 SEM observations

Surfaces of repaired specimens before and after ageing observed by SEM are shown in Fig. 53. After 8 weeks UV ageing, the glass fibers became exposed on the surface of RT repaired specimens because of the UV irradiation which are shown in Fig. 53(b). The reduced matrix morphology is the consequence of the photo-oxidation reaction on the thermal polymerizable resin. In Fig. 53(d), the UV repaired specimens also exist phenomena like fiber exposure and resin diminution, but the severity is slighter than RT repaired specimens. The distinction between the surface morphology of UV and RT repaired specimens after ageing also validates that the UV curing resin repaired specimens have better stability to resist photo-oxidation because of its post-curing behavior under UV irradiation environment.

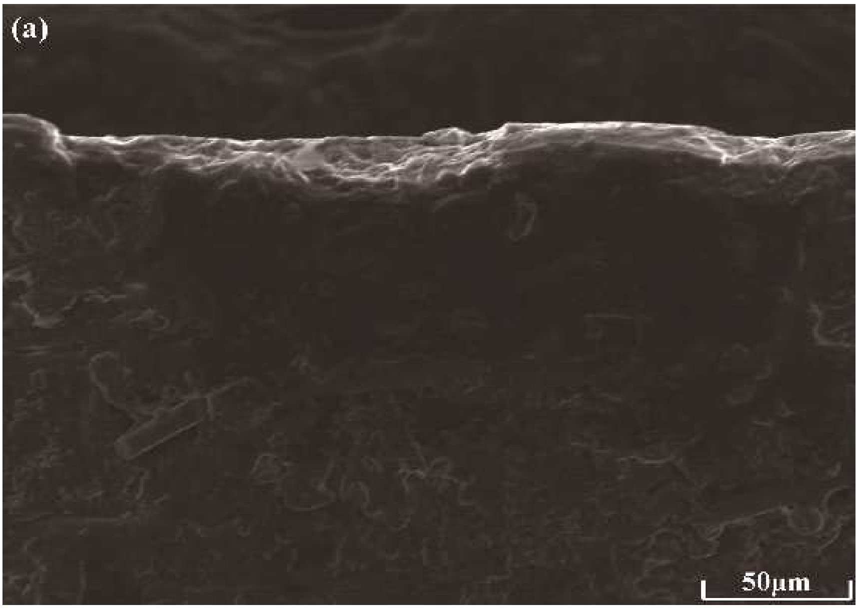

(a)

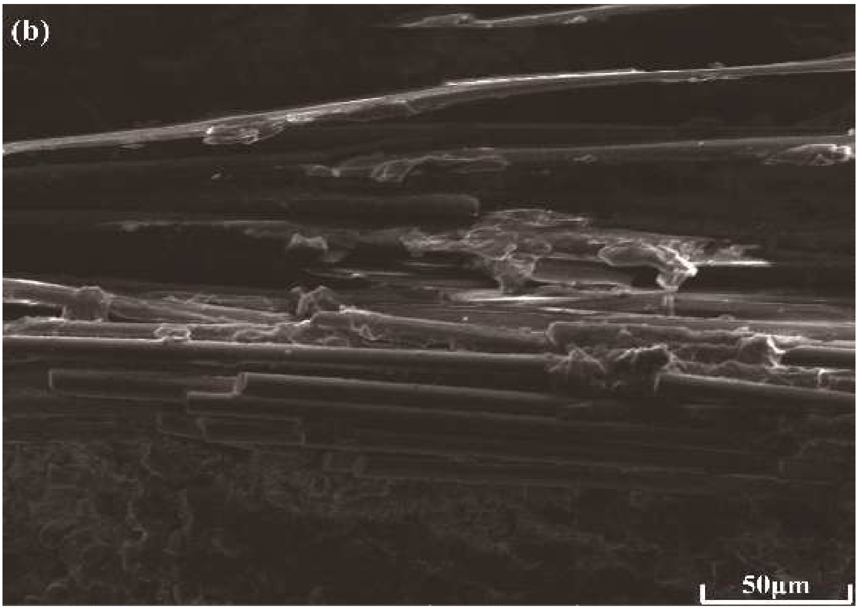

(b)

-continued-

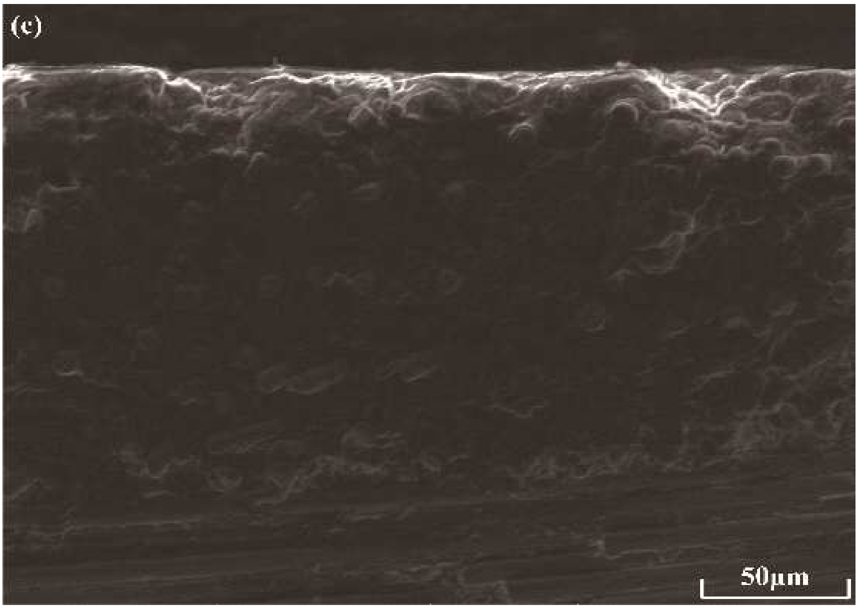

(c)

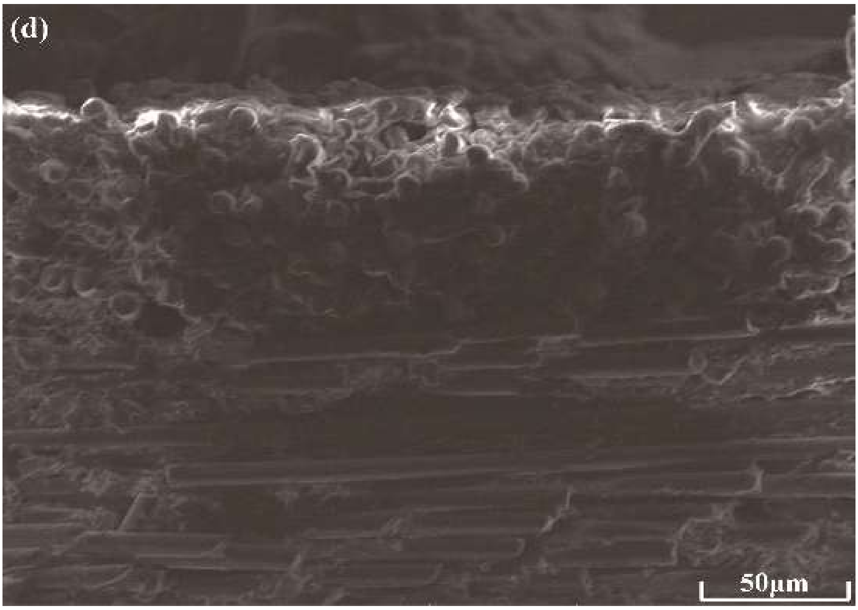

(d)

Fig. 53 SEM micrographs of surfaces on RT repaired specimen before (a) and after (b) UV ageing and UV repaired specimen before (c) and after (d) UV ageing

6.4 Conclusions

In this chapter, fundamental GFRP specimens fabricated by wet prepreg manufacture technique were pre-damaged and then repaired by attaching an external photo or thermal polymerizable resin-impregnated glass fabric patches followed with UV curing or room temperature curing, respectively. UV ageing was conducted to evaluate the durability of repaired specimens. Tensile, bending, SBS and DCB tests were performed. DSC and SEM were employed to do the thermal analysis and morphology observation, respectively. Base on the test results, the following preliminary conclusions are obtained:

(1) The tensile and bending strength together with the ILSS and mode I fracture toughness of UV repaired specimens exhibited higher values compared to RT repaired specimens after 8 weeks UV ageing. Especially the tensile strength and ILSS of UV repaired specimens exhibit increased values after ageing while that of RT repaired specimens all show the downward tendency. The spontaneous strengthen behavior of UV repaired specimens in UV irradiation environment result in excellent durability in UV ageing.

(2) During UV ageing, the UV repaired specimens were conducted post curing resulting in a strengthened and stiffened matrix which show better stability during UV irradiation environment. The RT repaired specimens present apparent matrix degradation phenomenon because of the photo-oxidation.

(3) The results of DSC reveal that the better crystallinity, higher density of chemical crosslink contributed by the UV irradiation is the explanation of the high durability of UV repaired specimens. SEM observation demonstrates slighter matrix degradation of UV repaired specimens after UV ageing which validate the good stability and durability of this repair methodology.

7. Summary and Conclusions

The photo polymerizable resin was well established in recent years in industries for its advantages like easy-operation, reduced costs, and rapid production. This dissertation investigates the comprehensive properties of UV repaired GFRP using for wind turbine blades by experimental and numerical analysis. The feasibility of the employment of photo polymerizable resin to realize the patch remediation on GFRP specimens is validated. Excellent mechanical properties in low temperature environment and durability in long-term acid and UV ageing are under evaluation for UV repaired GFRP specimens. The photo polymerizable resin is thus considered as the alternative of conventional thermal polymerizable resin and has enormous potential in the applications of wind turbine blades remediation. Base on the results obtained from previous chapters, the following preliminary conclusions are obtained:

(a) Feasibility validation of patch remediation by numerical analysis

(1) The numerical analysis was performed by ABAQUS, hashin damage criterion, quadratic stress criterion, and B-K criterion were employed to simulate the intralaminar and interlaminar fractures. The criterions are found to be well established in the modeling and simulation processing of repaired GFRP specimens.

(2) The numerical results of tensile and bending tests both show good agreements with that of experimental works. The adjacent two laminae of the external patch and fundamental specimen are the high-risk areas of fatal failure occurrence. A higher ultimate strength, stronger interlaminar cohesion and delayed crack propagation for UV repaired specimens are observed

through the import of failure criterions.

(3) The excellent adhesion and the better stress transferability of photo polymerizable resin reveal the feasibility and reliability to be utilized for patch remediation than thermal polymerizable resin.

(b) Mechanical behavior in low temperature

(1) The UV repaired specimens performed excellent adaptability of mechanical properties in low temperature environment compare to RT and post-curing repaired specimens which are considered a consequence of rigid polymeric matrix and denser crosslink of molecules.

(2) The mechanical properties tested in low temperature all have higher values than in ambient environment which is owing to the strengthened cohesive strength of the adjacent external and fundamental laminae, as well as the decreased velocity of crack diffusion. The residual thermal stress at low temperature also exerts a significant influence leading to higher ultimate strength.

(3) The morphology observations intuitively reveal the diversities between different repaired conditions which RT and post repaired specimens exist delamination phenomenon on external-fundamental lamina interface. UV repaired specimens show impediment of crack propagation, especially in a low temperature environment which result in higher ultimate strength and interlaminar fracture toughness.

(c) Durability assessment for acid ageing

(1) During acid ageing, UV and RT repaired specimens both present downward tendency in tensile and bending strength as well as ILSS and mode I fracture toughness. The drop mechanism is the inevitable attack on external

exposed polymeric surfaces by the acid environment. The RT repaired specimens show more violent property decrease compared to UV repaired specimens. The utilization of hardener is a potential factor resulting in the accelerated acid penetration rate during curing processing.

(2) The T_g values of UV repaired specimens are substantially identical before and after 8 weeks of acid ageing while that of RT repaired specimens present 3℃ upward. The increased T_g value of RT repaired specimens is the consequence of spontaneous curing behavior in room temperature. The negligible effect of acid ageing on T_g reveal the preservation of the overall integrity.

(3) The degradation phenomena on the external surfaces of both photo and thermal polymerizable resin repaired specimens are manifested as depressing, flaking, swelling and micro-size porosities. The severer damage of RT repaired specimens can be recognized compared to UV repaired specimens. The damaged matrix is the main results of decreased properties and reduced structural integrity.

(d) Durability assessment for UV ageing

(1) During UV ageing, the UV repaired specimens were conducted post-curing by suffering long-term UV irradiation, which result in a strengthened and stiffened matrix. The RT repaired specimens present obvious matrix degradation phenomenon because of the photo-oxidation phenomenon which inherent for all polymers. The post-curing phenomenon counteract the photo-oxidation for UV repaired specimens and lead to a better stability in UV irradiation environment.

(2) The results of DSC reveal that the better crystallinity and higher density of chemical crosslink contributed by the UV irradiation is the enhancement mechanism of the good durability of UV repaired specimens.

(3) SEM observations demonstrate slighter fiber exposure and resin diminution phenomena of UV repaired specimens compared to RT repaired specimens after UV ageing which validate the good stability and durability of this repair methodology.

Acknowledgements

Finishing this doctoral dissertation brings me a mix of satisfaction and nostalgia difficult to describe. Looking back in time, I quickly realize that these three years of research were a memorable stage in my life. Therefore, I want to express my gratitude to those who have contributed the most for my academic, professional and personal growth.

First and foremost, I would like to express my sincere appreciation to my Professor Yun-hae Kim for the advice guidance, support, and encouragement he provided during the studies, research and my daily life in Korea. What I learned from him is not only the method of learning but also the philosophy of life. His wisdom and romanticism will last me a lifetime.

In addition, my profound thanks to all my colleagues in our laboratory, Jeong-Hyo Hong, Jin-Woo Lee, Chang-Wook Park, Soo-Jeong Park, Seok-Hee Han, Kyung-Seok Jung, Ji-Su Choi, Kyo-moon Lee, Seong-jae Park and Kyung-In Cho with whom I have the great luxury of working.

Moreover, my profound thanks to my parents for their selfless love and unconditional support, what warms me up and makes me brave. Thank them for making me the person I want to be.

Lastly, I would like to express my special thanks to Yu Tianyu. He is my colleague, my friends, and the same existence as a family. I am very grateful for his supporting and understanding of me. Maybe I am still immature but he is so tolerant and caring. I look forward to understanding the meaning of life with him in the coming days.

References

Abdulmohsen, A., Sohail, M.A.K,M., Bachir, B.B., Bel, A.B.B. & Faycal, B., 2018. Effect of the patch length on the effectiveness of one-sided bonded composite repair for aluminum panels. *International Journal of Adhesion and Adhesives*, 81, pp.83-89.

Abraham, D., Matthews, S. & McIlhagger, R., 1998. A comparison of physical properties of glass fiber epoxy composites produced by wet lay-up with autoclave consolidation and resin transfer moulding. *Compos A Appl Sci Manuf*, 29, pp.795-801.

Advani, S.G. & Murat, S.E., 2010. *Process Modeling in Composites Manufacturing*. CRC Press, New York.

Advani, S.G. & Sozer, E.M., 2010. *Process modeling in composites manufacturing* (2nd ed.), Taylor & Francis, London.

Akonda, M.H., Kandola, B.K. & Horrocks, A.R., 2012. Effect of alkali and ultraviolet aging on physical, thermal, and mechanical properties of fibers for potential use as reinforcing elements in glass/silicate composites. *Polym. Adv. Technol,* 23, pp.1454-1463.

Alimardani, M., Toyserkani, E. & Huissoon, J.P., 2007. Three-dimensional numerical approach for geometrical prediction of multilayer laser solid freeform fabrication process. *Journal of laser applications*, 19(1), pp.14-25.

Amaro, A.M., Reis, P.N.B., Neto, M.A. & Louro, C., 2013. Effects of alkaline and acid solutions on glass/epoxy composites. *Polymer Degradation and Stability*, 98, pp.853-862.

Andrew, J.G. & Israel, H., 2006. Parametric study of scarf joints in composite structures. *Composite Structures*, 75, pp.364-376.

Armaroli, N. & Balzani, V., 2006. The Future of Energy Supply: Challenges and Opportunities. *Angewandte Chemie International Edition*, 46, pp. 52–66.

Ashby, M., Shercliff, H. & Cebon, D., 2007. *Materials: Engineering, Science , Processing and Design*. Published by Elsevier Ltd.

Asif, M. & Muneer, T., 2007. Energy supply, its demand and security issues for developed and emerging economies. *Renewable Sustainable Energy Reviews*, 11(7), pp.1388–1413.

Baere, I.D., Jacques, S., Paepegem, W.V. & Degrieck, J., 2012. Study of the Mode I and Mode II interlaminar behavior of a carbon fabric reinforced thermoplastic. *Polymer Testing*, 31, pp.322-332.

Bao, L., Okazawa, T., Xu, A. & Shi, J., 2018. A simple repair method for GFRP delamination using ultraviolet-curable resin. *Adv Compos Mater*, 27, pp.249-259.

Bendemra, H., Compston, P. & Crothers, P.J., 2015. Optimisation study of tapered scarf and stepped-lap joints in composite repair patches. *Compos Struct*, 130, pp.1-8.

Bond, G.G., Griffith, J.M., Hahn, G.L., Bongiovanni, C. & Boyd, J., 2008. Non-autoclave prepreg manufacturing technology. *Proc 40th int SAMPE tech conf,* Society for the Advancement of Material and Process Engineering, Memphis, TN.

Boyd, J. & Maskell, R.K., 2001. Product design for low cost manufacturing of composites for aerospace applications, *Proc SAMPE 2001 conf*, *Society for the Advancement of Material and Process Engineering*, Long Beach, CA.

Brondsted, P., Lilholt, H., Lystrup, A. & Annu., 2005. Composite materials for wind power turbine blades. *Annual Review of Materials Research*, 35, pp.505-538.

Bruno, M.L., Luiz, F.M.L., Vitor, L.Reis., Maurício, V.D. & Nubia, N.A.D.S., 2018. Strain rate effects on the intralaminar fracture toughness of composite laminates subjected to compressive load. *Composite Structures*, 186, pp.94-105.

Budhe, S., Banea, M.D. & Barros, D.S., 2018. Bonded repair of composite structures in aerospace application: a review on environmental issues. *Appl Adhes Sci*, 6, pp.3.

Buitrago, B.L., Santiuste, C. & Sánchez-Sáez, S., 2010. Modelling of composite sandwich structures with honeycomb core subjected to high-velocity impact. *Compos Struct*, 92, pp.2090-2096.

Camanho, P.P. & Dávila, C.G., 2003. Numerical Simulation of Mixed-mode Progressive Delamination in Composite Materials. *Journal of composites materials*, 37(16), pp.1415–1436.

Chang, F.K. & Chang, K.Y., 1987. A Progressive Damage Model for Laminated Composites Containing Stress Concentrations. *J Compos Mater*, 21, pp.834–855.

Chen, Z. et al., 2018. Effect of curing cycles using wet prepreg processing on mechanical properties. *International Journal of Modern Physics B*, 32, pp.1840076.

Chen, Z., Yu, T, Park, S.J., Hong, J.H. & Kim, Y.H., 2019. Rapid in situ remediation of glass fiber wind turbine blades in low temperature environment. *Modern Physics Letters B*, 25 Apr.

Choi, J.S., Park, S.J., Chen, Z. & Kim, Y.H., 2019. Development of environment-friendly CF/BF hybrid composites according to the arrangement angle and volume fraction of basalt fiber. *Modern Physics Letters B*, 09 May.

Chukov, D.I., Stepashkin, A.A. & Maksimkin, A.V., 2015. Investigation of structure, mechanical and tribological properties of short carbon fiber reinforced UHMWPE-matrix composites. *Compos Part B*, 76, pp.79–88.

Chun H.W. & Duong C.N., 2015. Bonded Joints and Repairs to Composite Airframe Structures. Academic Press.

Chun, H.W. & Andrew, J., 2009. Optimum shapes of scarf repairs, *Composites Part A: Applied Science and Manufacturing*, 40(9), pp.1407-1418.

Compston, P., Schiemer, J. & Cvetanovska, A., 2008. Mechanical properties and styrene emission levels of a UV-cured glass-fibre/vinylester composite. *Compos Struct*, 86, pp.22–26.

Cormier, L., Joncas, S., Rogier & Nijssen, P.L., 2016. Effects of low temperature on the mechanical properties of glass fibre–epoxy composites: static tension, compression, R = 0.1 and R = -1 fatigue of ±45° laminates. *Wind Energ*, 19, pp.1023–1041.

Costa, A.P., Botelho, E.C. & Pardini, L.C., 2010. Influence of environmental conditioning on the shear behavior of poly(phenylene sulfide)/glass fiber composites. *J. Appl. Polym. Sci.*, 118, pp.180-187.

Da, S., L, F.M., Öchsner, A. & Adams, R.D., 2011. *Handbook of Adhesion Technology*. Springer-Verlag Berlin Heidelberg.

Di, P.A. & Compston, P., 2009. Resin hardness and interlaminar shear strength of a glass-fibre/vinylester composite cured with high intensity ultraviolet (UV) light. *J Mater Sci*, 44, pp.4188–4190.

Dios, M., Gonzalezer, P.L., Dios, D. & Maffezzoli, A., 2017. A mathematical modeling approach to optimize composite parts placement in autoclave. *International Transactions in Operational Resarch*, 24, pp.115–141.

Donaldson, S.L. & Miracle, D.B., 2001. *Metal handbook: composites*, vol. 21. Materials Park (OH): ASM international.

Dorian, J.P., Franssen, H.T. & Simbeck, D.R., 2006. Global challenges in energy. *Energy Policy*, 34(15), pp.1984–1991.

Dresselhaus, M.S. & Thomas, I.L., 2001. *Alternative energy technologies. Nature*, 414, 332–337.

Dudek, P., 2013. FDM 3D Printing Technology in Manufacturing Composite Elements. *Archives of Metallurgy and Materials*, 58(4), pp.1415-1418.

Ellakwa, A.E., Shortall, A.C. & Marquis, P.M., 2002. Influence of fiber type and wetting agent on the flexural properties of an indirect fiber reinforced composite. *J Prosthet Dent*, 88, pp.485–490.

Esteban, M.D., Diez, J.J., Lopez, J.S. & Negro, V., 2011. Why offshore wind energy. *Renewable Energy*, 36(2), pp.444–450.

Feng, P., Hu, L., Zhao, X.L., Cheng, L. & Xu, S., 2014. Study on thermal effects on fatigue behavior of cracked steel plates strengthened by CFRP sheets. *Thin-Walled Structures*, 82, pp.311-320.

Fu, B., Teng, J.G., Chen, J.F., Chen, G.M. & Guo, Y.C., 2017. Concrete cover separation in frp-plated rc beams: mitigation using frp u-jackets. *J Compos Constr*, 21, pp.04016077.

George, M., 2011. The challenge of wind turbine blade repair. *Renewable Energy Focus*, 12, pp.2-66.

Gholami, M., Sam, A.R.M., Yatim, J.M. & Tahir, M.M., 2013. A review on steel/cfrp strengthening systems focusing environmental performance. *Constr Build Mater*, 47, pp.301-10.

Goh, J.Y., Georgiadis, S., Orifici, A.C. & Wang, C.H., 2013. Effects of bondline flaws on the damage tolerance of composite scarf joints. *Compos Part A*, 55, pp.110–119.

Grunenfelder, L.K., Centea, T., Hubert, P. & Nutt, S.R., 2013. Effect of room-temperature out-time on tow impregnation in an out-of-autoclave prepreg. *Composites Part A*, 45, pp.119–126.

Hallquist, J.O., 2006. *LS-DYNA theory manual. Livermore Softw Technolodge Corp*, 2006.

Hammami, A. & Al-Ghuilani, N., 2004. Durability and environmental degradation of glass-vinylester composites. *Polym Composite*, 25, pp.609-616.

Hartwig, G. & Knaak, S., 1984. Fibre-epoxy composites at low temperatures. *CRYOGENICS*, 24(11), pp.639-647.

Hashin, Z. & Rotem, A., 1973. A Fatigue Failure Criterion for Fiber Reinforced Materials. *J Compos Mater*, 7, pp.448–464.

Hashin, Z., 1980. A Reinterpretation of the Palmgren-Miner Rule for Fatigue Life Prediction. *J Appl Mech*, 47, pp.324-328.

Hasiaoui, B., Ibrahim, A. & L’Hostis, G., 2018. Free radical photopolymerization process for fiber-reinforced polymer: Effect on the mechanical properties. *Polym Adv Technol*, 2018, pp.1-8.

Hasiaoui, B., Ibrahim, A. & L’Hostis, G., 2018. Free radical photopolymerization process for fiber-reinforced polymer: Effect on the mechanical properties. *Polym Adv Technol*, 2018, pp.1-8.

Haymen, B., Wedel-Heinen, J. & Brondsted, P., 2008. Materials Challenges in Present and Future Wind Energy. *MRS Bulletin*, 33, pp.343–353.

Herbert, G.M., Iniyan, S., Sreevalsan, E. & Rajapandian, S., 2007. A review of wind energy technologies. *Renewable Sustainable Energy Reviews*, 11(6), pp.1117-1145.

Heshmati, M., Haghani, R. & Al-Emrani, M., 2015. Environmental durability of adhesively bonded frp/steel joints in civil engineering applications: state of the art. *Compos Part B*: Eng, 81, pp.259-75.

Hideki, S., Yoshiyuki, N., Masatoshi, K. & Ken, T.S., 2003. Corrosion Behavior of Epoxy Resin Cured with Different Amount of Hardener in Corrosive Solutions. *Materials Science Research International*, 9, pp.230-234.

Hiroyuki, K. & Srivastava, V.K., 2011. The effect of an acidic stress environment on the stress-intensity factor for GRP laminates. *Composites Science and Technology*, 61, pp.1109-1114.

Hsiao, K. & Heider, D., 2012. *Vacuum assisted resin transfer molding (VARTM) in polymer matrix composites.* Woodhead Publishing Limited.

Huang, J.J., Yuan, T., Ye, X.Y., Man, L.M., Zhou, C., Hu, Y., Zhang, C.Q. & Yang, Z.H., 2018. Study on the UV curing behavior of tung oil: Mechanism, curing activity and film-forming property. *Industrial Crops & Products*, 112, pp.61-69.

Isaac, M., Daniel. & Ori, lshai., 2006. *Engineering mechanics of composite materials.* Oxford University Press, Inc.

Islam, M.R., Mekhilef, S. & Saidur, R., 2013. Progress and recent trends of wind energy technology. *Renewable Sustainable Energy Reviews*, 21, pp.456-468.

Jefferson, A.J., Arumugam, V. & Dhakal, H.N., 2018. Overview of different damage and common repair methods in composite laminates. *Repair Polym Compos*, pp.45–95.

Jerry, A.P., Li, G.Q., Pang, S.S. & Michael, A., Stubblefield, 2004. Light intensity effect on UV cured FRP coupled composite pipe joints. *Composite Structures*, 64, pp.539-546.

Kaldellis, J.K. & Zafirakis, D., 2011. The wind energy revolution: A short review of a long history. *Renewable Energy*, 36, pp.1887-1901.

Kara, M., Uyaner, M. & Avci, A., 2015. Repairing impact damaged fiber reinforced composite pipes by external wrapping with composite patches. *Compos Struct*, 123, pp.1–8.

Katnam, K.B., Comer, A.J. & Roy, D., 2015. Composite Repair in Wind Turbine Blades : An Overview. *The Journal of Adhesion*. 91, pp.113–139.

Ke, X.X., Liang, H.B., Xiong, Lei., Huang, S.M. & Zhu, M., 2016. Synthesis, curing process and thermal reversible mechanism of UV curable polyurethane based on Diels-Alder structure. *Progress in Organic Coatings*, 100, pp.63–69.

Khalili, S.M.R., Soroush, M., Davar, A. & Rahmani, O., 2011. Finite element modeling of low-velocity impact on laminated composite plates and cylindrical shells. *Compos Struct*, 93, pp.1363–1375.

Khan, L.A., Kausar, A. & Day, R.J., 2017. Aerospace composite cured by quickstep and autoclave processing techniques : Evaluation and comparison of reaction progress. *Aerosp Sci Technol*, 65, pp.100–105.

Kim, J.K. & Mai, Y., 1991. High strength, high fracture toughness fibre composites with interface control—A review. *Compos Sci Technol*, 41, pp.333–378.

Kong, S.Y., Yang, X. & Lee, Z.Y., 2018. Mechanical performance and numerical simulation of GFRP-concrete composite panel with circular hollow connectors and epoxy adhesion. *Constr Build Mater*, 184, pp.643–654.

Kratz, J., Hsiao, K., Fernlund, G. & Hubert, P., 2012. Thermal models for MTM45-1 and Cycom 5320 out-of-autoclave prepreg resins. *J Compos Mater*, 47, pp.341-352.

Kruth, J.P., Wang, X., Laoui, T. & Froyen, L., 2003. Lasers and materials in selective laser sintering. *Assembly Automation*, 23(4), pp.357-371.

Laffan, M.J., Pinho, S.T. & Robinson, P., 2012. Measurement of the fracture toughness associated with the longitudinal fibre compressive failure mode of laminated composites. *Compos Part A Appl Sci Manuf*, 43, pp.1930–1938.

Lee, C.W., Gibson, T., Tienda, K.A. & Storage, T.M., 2010. Reaction rate and viscosity model development for Cytec’s Cycom® 5320 family of resins, *Proc 42nd int SAMPE tech conf, Society for the Advancement of Material and Process Engineering*, Salt Lake City, UT.

Lee, H.G., Kang, M.G. & Park, J., 2015. Fatigue failure of a composite wind turbine blade at its root end. *Composite Structures*, 133, pp.878–885.

Li, G.Q., Neema, P., Adam, C., Jerry, P. & Pang, S.S., 2003. Fast repair of laminated beams using UV curing composites, *Composite Structures*, 60, pp.73-81.

Liu, B., Xu, F. & Feng, W., 2016. Experiment and design methods of composite scarf repair for primary-load bearing structures. *Compos Part A Appl Sci Manuf*, 88, pp.27–38.

Liu, H., Falzon, B.G. & Tan, W., 2018. Experimental and numerical studies on the impact response of damage-tolerant hybrid unidirectional/woven carbon-fibre reinforced composite laminates. *Compos Part B*, 136, pp.101–118.

Liu, P., Meng, F. & Barlow, C.Y., 2019. Wind turbine blade end-of-life options: An eco-audit comparison. *J Clean Prod*, 212, pp.1268–1281.

Loos, M., 2015. *Carbon Nanotube Reinforced Composites.* William Andrew Publishing.

Lu, J.H. & Youngblood, J.P., 2015. Adhesive bonding of carbon fiber reinforced composite using UV-curing epoxy resin. *Compos Part B*, 82, pp.221–225.

Lu, T., Solis-Ramos, E., Yi, Y. & Kumosa, M., 2018. UV degradation model for polymers and polymer matrix composites. *Polymer Degradation and Stability*, 154, pp.203-210.

Mahat, K.B., Alarifi, I., Alharbi, A. & Asmatulu, R., 2016. Effects of UV Light on Mechanical Properties of Carbon Fiber Reinforced PPS Thermoplastic Composites, Macromol. *Symp*, 365, pp.157-168.

Mallick, P.K., 2007. *Fiber-reinforced composites: Materials, Manufacturing, and design.* Taylor & Francis Group, LLC.

Marsh, G., 2011. Meeting the challenge of wind turbine blade repair. *Renew Energy Focus*, 12, pp.62–66.

Matsuzaki, R., Kobayashi, S., Todoroki, A. & Mizutani, Y. 2011. Full-field monitoring of resin flow using an area-sensor array in a VaRTM process. *Compos Part A*, 42, pp.550–559.

Matzenmiller, A., Lubliner, J. & Taylor, R.L., 1995. A constitutive model for anisotropic damage in fiber-composites. *Mech Mater*, 20, pp.125–152.

Mehrad, A., Maya, P. & Cengiz, A.M., 2018. Fabricating high-quality VARTM laminates by magnetic consolidation: experiments and process model, *Composites Part A: Applied Science and Manufacturing*, 114, pp.398-406.

Mohammadreza, E. & Ali, F., 2016. Tensile behavior of thermoplastic composites including temperature, moisture, and hygrothermal effects. *Polymer Testing*, 51, pp.151-164.

Mortimer, S., Smith, M.J. & Olk, E., 2010. Product development for out-of-autoclave (O.O.A.) manufacture of aerospace structure, Proc SAMPE 2010 conf, *Society for the Advancement of Material and Process Engineering*, Seattle, WA.

Murray, R.E., Jenne, S. & Snowberg, D., 2019. Techno-economic analysis of a megawatt-scale thermoplastic resin wind turbine blade. *Renew Energy*, 131, pp.111–119.

Nele, L., Caggiano, A. & Teti, R., 2016. Autoclave cycle optimization for high performance composite parts manufacturing. *Procedia CIRP*, 57, pp.241–246.

Ning, F., Cong, W. & Qiu, J., 2015. Additive manufacturing of carbon fiber reinforced thermoplastic composites using fused deposition modeling. *Composites Part B*, 80, pp.369-378.

Pantano, V., Compston, P. & Stachurski, Z.H., 2002. Effect of matrix toughness on the shear strength of brittle and rubber-modified glass-fiber/vinyl ester composites. *Journal of Materials Science Letters*, 21(10), pp.771-773.

Park, J., Tari, M.J. & Hahn, H.T., 2000. Characterization of the laminated object manufacturing (LOM) process. *Rapid Prototyping Journal*, 6(1), pp.36-49.

Park, S.J., Choi, J.S., Lee, J.W., Yu, T., Chen, Z., Kim, Y.H. & Bae, C.W., 2019. Influence of nanoparticle dispersibility on hygrothermal properties of HNT-GFRP/BFRP nanocomposites. *Modern Physics Letters B*, 25 Apr.

Peck, J.A., Li, G., Pang, S.S. & Michael, A., 2004. Stubblefield. Light intensity effect on UV cured FRP coupled composite pipe joints. *Composite Structures*, 64, pp.539-546.

Peck, J.A., Li, G., Pang, S.S. & Stubblefield, M.A., 2004. Light intensity effect on UV cured FRP coupled composite pipe joints. *Compos Struct*, 64, pp.539-546.

Pilar, D.L.R.G., Escamilla, A.C. & Nieves, G.G.M., 2013. Bending reinforcement of timber beams with composite carbon fiber and basalt fiber materials. *Compos Part B*, 55, pp.528-536.

Pu, L., Claire, Y. & Barlow., 2017. Wind turbine blade waste in 2050. *Waste Management*, 62, pp.229-240.

Qiu, Q. & Kumosa, M., 1997. Corrosion of E-glass fibers in acidic environments. *Composites Science and Technology*, 57, pp.497-507.

Quarton, D.C., 1998. The evolution of wind turbine design analyses - a twenty year progress review. *Wind Energy*, 1, pp.5-24.

Raghu Prasad, B.K. & Pavan Kumar, D.V.T.G., 2008. Analysis of composite ENF specimen using higher order beam theories. *Thin-Walled Structures*, 46, pp.676-688.

Reid, S.R. & Zhou, G., 2000. *Impact behavior of Fibre-reinforced Composite Materials and Structures*. Taylor & Francis.

Repecka, L. & Boyd, J., 2002. Vacuum-bag-only-curable prepregs that produce void-free parts, Proc SAMPE 2002 conf, *Society for the Advancement of Material and Process Engineering*, Long Beach, CA.

Ridgard, C., 2000. Advances in low temperature curing prepregs for aerospace structures. Proc SAMPE 2000 conf, *Society for the Advancement of Material and Process Engineering*, Long Beach, CA.

Ridgard, C., 2009. Out of autoclave composite technology for aerospace, defense and space structures. Proc SAMPE 2009 conf, *Society for the Advancement of Material and Process Engineering*, Baltimore, MD.

Ridgard, C., 2010. Next generation out of autoclave systems, Proc SAMPE 2010 conf, *Society for the Advancement of Material and Process Engineering*, Seattle, WA.

Sanaa, E.M., Karim, O., Mohammed, M.I., Bousselham, K. & Abderrahmane H., 2018. Aerodynamics and structural analysis of wind turbine blade. *Procedia Manufacturing*, 22, pp.747–756.

Sangermano, M., D'Anna, A., Marro, C., Klikovits, N. & Liska, R., 2018. UV-activated frontal polymerization of glass fibre reinforced epoxy composites. *Composites Part B*, 143, pp.168-171.

Sanjay, K. & Mazumdar., 2002. *Composites Manufacturing: Materials, Product, and Process Engineering*. Taylor & Francis Group, LLC

Senthil, P., Vinodh, S. & Jayanth N., 2017. A review on composite materials and process parameters optimisation for the fused deposition modelling process. *Virtual and Physical Prototyping*, 12(1), pp.47-59.

Serge, A., 1998. *Impact on Composite Structures*. Cambridge University Press

Shi, Y., Swait, T. & Soutis, C., 2012. Modelling damage evolution in composite laminates subjected to low velocity impact. *Compos Struct*, 94, pp.2902–2913.

Shigeru, Y., 2013. Lightning protection of wind turbine blades. *Electric Power Systems Research*, 94, pp.3–9.

Smojver, I. & Ivančević, D., 2011. Bird strike damage analysis in aircraft structures using Abaqus/Explicit and coupled Eulerian Lagrangian approach. *Compos Sci Technol*, 71, pp.489–498.

Surendra, K.M., Neeti, S. & Ray, B.C., 2007. *Acidic Degradation of FRP Composites. National Conference on Developments In Composites 2007.*

Tan, W. & Falzon, B.G., 2016. Modelling the nonlinear behavior and fracture process of AS4/PEKK thermoplastic composite under shear loading. *Compos Sci Technol*, 126, pp.60–77.

Thomas, L. & Ramachandra, M., 2018. Advanced materials for wind turbine blade- A Review. *Mater Today Proc*, 5, pp.2635–2640.

Thomas, L. & Ramachandra, M., 2018. Advanced materials for wind turbine blade- A Review. *Materials Today: Proceedings*, 5, pp.2635–2640.

Tsai, S.W. & Wu, E.M., 1971. A General Theory of Strength for Anisotropic Materials. *J Compos Mater*, 5, pp.58–80.

Tsai, S.W., 1965. NASA CR-224, *Strength Characteristics of Composite Materials.* Newport Beach, CA, USA.

Tsai, Y.I., Bosze, E.J., Barjasteh, E. & Nutt, S.R., 2009. Influence of hygrothermal environment on thermal and mechanical properties of carbon fiber/fiberglass hybrid composites. *Compos Sci Technol,* 69, pp.432-7.

Upadhya, A.R., Dayananda, G.N. & Kamalakannan, G.M., 2011. Autoclaves for Aerospace Applications : Issues and Challenges. *Hindawi Publishing Corporation International Journal of Aerospace Engineering,* 2011, pp.1-11.

Veers, P.S. & Ashwill, T.D., 2003. Special Review Issue on Advances in Wind Energy. *Wind Energy*, 6(3), pp.245–259.

Vilanova, I., Torres, L., Baena, M. & Llorens, M., 2016. Numerical simulation of bond-slip interface and tension stiffening in GFRP RC tensile elements. *Compos Struct*, 153, pp.504–513.

Vinson, J.R. & Sierakowski, R.L., 2006. *The Behavior of Structures Composed of Composite Materials.* Springer Netherlands.

Wang, C.H., Goh, J.Y. & Ahamed, J., 2015. Damage Tolerance Analysis of Adhesively Bonded Repairs to Composites Structures. *18th International Conference on Composite Materials Damage Tolerance Analysis of Adhesively Bonded.*

Wang, C.H., Gunnion, A.J. & Wang, C.H., 2018. Optimum shapes for minimising bond stress in scarf repairs. *Australian Journal of Mechanical Engineering*, 6(2), pp.153-158.

Wang, N., Zhao, J.H. & Zhu, N.L., 2014. Mechanics Properties on Glass Fiber Reinforced Polymer-Confined Concrete Short Columns. *Asian J Chem*, 26, pp.5387–5392.

Wang, Y. & Zhou, C., 2017. Bond characteristics of cfrp/steel interface end-anchored with g-shaped clamps. *Polym Polym Compos*, 25, pp.661-7.

Wang, Y., Zheng, Y. & Li, J., 2018. Experimental study on tensile behavior of steel plates with center hole strengthened by CFRP plates under marine environment. I*nt J Adhes Adhes*, 84, pp.18–26.

West, A.P., Sambu, S.P. & Rosen, D.W., 2001. A process planning method for improving build performance in stereolithography. *Computer-Aided Design*, 33, pp.65-79.

William, D. & Callister., 2007. *Materials Science and Engineering.* John Wiley & Sons, Inc.

Wood, K., 2011 (April). *Composites Technology.* Composites World, Web Publisher.

Wu, X. & Anthony, M.W., 2017. Fracture toughness of woven textile composites. *Engineering Fracture Mechanics,* 169, pp.184-188.

Xin, Q., Oleksandr, G.K., Diego, P. & Ica, M.Z., 2018. Effect of polycarbonate film surface morphology and oxygen plasma treatment on mode I and II fracture toughness of interleaved composite laminates. *Composites: Part A*, 105, pp.138-149.

Yakovlev, A., Trunova, E., Grevey, D., Pilloz, M. & Smurov, I., 2005. Laser-assisted direct manufacturing of functionally graded 3D objects. *Surface and Coatings Technology, Surface & Coatings Technology*, 190(1), pp.15-24.

Yalcinkaya, M.A., Sozer, E.M. & Altan, M.C., 2017. Fabrication of high quality composite laminates by pressurized and heated-VARTM. *Compos Part A*, 102,pp.336–346.

Yan, F. & Lin, Z., 2016. Bond behavior of GFRP bar-concrete interface: Damage evolution assessment and FE simulation implementations. *Compos Struct*, 155, pp.63–76.

Ye, Y., Chen, H., Wu, J. & Chan, C.M., 2011. Interlaminar properties of carbon fiber composites with halloysite nanotube-toughened epoxy matrix. *Composites Science and Technology*, 71, pp.717-723.

Yu, T., Chen, Z., Park, S.J. & Kim, Y.H., 2019. Rapid in situ remediation of glass fiber wind turbine blades in low temperature environment. *Modern Physics Letters B*, 11 Apr.

Zhai, Z., Feng, L., Li, G., Liu, Z. & Chang, X., 2016. The anti-ultraviolet light (UV) aging property of aluminium particles/epoxy composite. *Progress in Organic Coatings*, 101, pp.305-308.

Zhang, Z., Liu, Y. & Huang, Y., 2002. The effect of carbon-fiber surface properties on the electron-beam curing of epoxy-resin composites. *Compos Sci Technol*, 62, pp.331–337.

Zhong, W., Li, F. & Zhang, Z., 2001. Short fiber reinforced composites for fused deposition modeling. *Materials Science and Engineering*, A301, pp.125-130.

Zidani, M.B., Belakhdar, K., Tounsi. A. & Adda Bedia, E.A., 2015. Finite element analysis of initially damaged beams repaired with FRP plates. *Composite Structures*, 134, pp.429-439.